Exchange bias and spin-orbit torque induced switching with antiferromagnetic MnN – a novel material for spintronics

Doctoral Thesis in Physics by

Mareike Dunz

Dissertation submitted to
Department of Physics
Bielefeld University

March 2021

Supervisor & 1st Examiner
Prof. Dr. Markus Meinert

2nd Examiner
Prof. Dr. Thomas Huser

Printed on permanent paper °° ISO 9706
Gedruckt auf alterungsbeständigem Papier °° ISO 9706

Declaration of Authorship

I hereby confirm that I have written this thesis independently and without use of others than the acknowledged references. Figures and text were partly taken from my own publications, which originated directly from this work. Furthermore, I declare that I have not previously submitted this thesis to any examination office.

(Mareike Dunz)

Publications

Publications included in this thesis

- *Role of the Ta buffer layer in Ta/MnN/CoFeB stacks for maximizing exchange bias*
  M. Dunz and M. Meinert
  J. Appl. Phys. **128**, 153902 (2020)

- *Spin-orbit torque induced electrical switching of antiferromagnetic MnN*
  M. Dunz, T. Matalla-Wagner, and M. Meinert
  Phys. Rev. Research **2**, 013347 (2020)

- *Enhanced exchange bias in MnN/CoFe bilayers after high-temperature annealing*
  M. Dunz, J.-M. Schmalhorst, and M. Meinert
  AIP Adv. **8**, 056304 (2018)

Publications not included in this thesis

- *Unidirectional and uniaxial anisotropies in the MnN/CoFeB exchange bias system*
  A. Rai, M. Dunz, A. Sapkota, P. Zilske, J. B. Mohammadi, M. Meinert, C. Mewes, and T. Mewes
  J. Magn. Magn. Mater. **485**, 374 (2019)

- *Effects of field annealing on MnN/CoFeB exchange bias systems*
  P. Quarterman, I. Hallsteinsen, M. Dunz, M. Meinert, E. Arenholz, J. A. Borchers, and A. J. Grutter
  Phys. Rev. Mater. **3**, 064413 (2019)

- *Improved thermal stability in doped MnN/CoFe exchange bias systems*
  M. Dunz, B. Büker, and M. Meinert
  J. Appl. Phys. **124**, 203902 (2018)

Conference Contributions

- *Spin-torque induced electrical switching of antiferromagnetic MnN*
  M. Dunz, T. Matalla-Wagner, and M. Meinert
  64th Annual Conference on Magnetism & Magnetic Materials,
  Las Vegas, Talk, BB-05

- *Spin-orbit torque induced electrical switching of antiferromagnetic MnN*
  M. Dunz, T. Matalla-Wagner, and M. Meinert
  SPICE Workshop on Antiferromagnetic Spintronics: from topology to neuromorphic computing, Mainz, Poster

- *Comparing thickness dependence and transport properties of the organic semiconductors $F_{16}CuPc$ and $F_{16}CoPc$*
  M. Dunz, K. Rott, J.-M. Schmalhorst, and G. Reiss
  DPG Frühjahrstagung Regensburg 2019, Poster, HL 12.40

- *Broadband FMR measurements on MnN/CoFeB exchange bias systems*
  M. Dunz, A. Rai, J. B. Mohammadi, A. Sapkota, C. Mewes, T. Mewes, P. Zilske, and M. Meinert
  2018 IEEE International Conference on Microwave Magnetics,
  Exeter, Talk

- *Large increase of exchange bias in MnN/CoFe bilayers after high-temperature annealing*
  M. Dunz, J.-M. Schmalhorst, and M. Meinert
  DPG Frühjahrstagung Berlin 2018, Talk, MA 26.4

- *In situ transport measurements in organic field effect transistors with $F_{16}CuPc$*
  M. Dunz, K. Rott, J.-M. Schmalhorst, and G. Reiss
  DPG Frühjahrstagung Berlin 2018, Poster, HL 13.53

- *Large increase of exchange bias in MnN/CoFe bilayers after high-temperature annealing*
  M. Dunz, J.-M. Schmalhorst, and M. Meinert
  62nd Annual Conference on Magnetism & Magnetic Materials, Pittsburgh, Talk, FE-07

- *Improved thermal stability of doped MnN/CoFe exchange bias systems*
  M. Dunz, B. Büker, and M. Meinert
  DPG Frühjahrstagung Dresden 2017, Talk, MA 26.2

Contents

Chapter 1

Introduction

Over the last decades, the continuously increasing demand for data storage and fast information processing in large parts of our everyday lives has lead to extensive research for new materials and devices in the area of micro- and nanoelectronics. To follow Moore's law, predicting that the number of transistors in integrated circuits doubles almost every two years [1], alternatives to conventional electronics need to be explored. Here, the emerging field of so-called spintronics, short for spinelectronics, has proven to provide very promising and sustainable technologies [2, 3, 4].

Whereas conventional electronics rely on the charge transported by an electron, in spintronics the electron's spin is introduced as an additional degree of freedom. This makes it possible to observe spin-dependent transport phenomena and pure spin currents, allowing for the transfer of information without the need for electrical currents [2]. For spintronics to become as successful as it is today, the discovery of different magnetoresistive effects like the tunnel-magnetoresistance (TMR) in 1975 [5] and the giant-magnetoresistance (GMR) in 1988 [6] was crucial. In a thin film trilayer stack, where two ferromagnetic electrodes are separated either by a normal metal (GMR) or an insulator (TMR), the resistance that is measured when sending a current through the junction is dependent on the orientation of the ferromagnets' magnetization towards each other [7]. For a parallel magnetization alignment of the electrodes, a lower resistance is measured than for an antiparallel orientation. This is attributed to the fact that only electrons carrying a spin that is parallel to the

magnetization of the corresponding electrode can pass through it. Electrons having an antiparallel spin with regard to the magnetization are backscattered, making the electrodes act as spin filters. Accordingly, in the state of parallel magnetized electrodes, one spin channel can easily pass the junction. In the antiparallel configuration, electrons are either scattered at the first or the second electrode as their spin is definitely antiparallel to one of them [7]. Based on nano-scale TMR junctions, magnetoresistive random-access memory (MRAM) has been developed, which can nowadays already be found in a couple of commercial memory chips and storage devices [8, 9].

Like for GMR and TMR spin valves, spintronic elements are usually based on ferromagnetic thin films. Ferromagnets can polarize and detect spin currents and may be manipulated via spin torques. Thus, they are able to magnetically store, read, or write information. Even though this information is robust against electric field pertubations, it might be disturbed and erased by high magnetic fields [10]. Furthermore, downscaling devices with ferromagnetic components, magnetic stray fields become a severe problem [11]. Hence, a class of materials that is quite similar to ferromagnets, yet providing some fundamentally different properties, has recently gained strongly increasing interest in terms of spintronic application: antiferromagnets [12, 13, 14].

Just like ferromagnets, antiferromagnets exhibit a uniform ordering of magnetic moments, called Néel order, without the need for external magnetic fields. However, instead of the parallel alignment as found in ferromagnets, magnetic moments in antiferromagnets align in an antiparallel manner [15, 16]. Usually, there are two magnetic sublattices with opposite atomic magnetic moments $\vec{m}_1 = -\vec{m}_2$, whose orientation is described by the Néel vector $\vec{L} = \vec{m}_1 - \vec{m}_2$. Thus, antiferromagnets do not have a net magnetization [16]. On the one hand, this yields a very high stability against magnetic pertubations. On the other hand, the insensitivity towards magnetic fields makes it extremely hard to access or change the Néel order [13]. Lacking any mechanism for the manipulation of their magnetic moments, antiferromagnets were therefore considered “interesting but useless”, as stated by Louis Néel in his Nobel lecture [17], for nearly half a century.

About 50 years after their discovery [17], the first application of antiferromagnets was found in GMR and TMR valves [18]. Here, they can be used to pin one of the ferromagnetic electrodes, making it less sensitive to external magnetic fields, via an interfacial exchange coupling mechanism called exchange bias effect [19]. This allows for the generation of distinct stable resistance states at zero external magnetic field [2]. Consequently, antiferromagnets quite rapidly became important in spintronic devices and are widely used as passive components in exchange bias systems up to today [2, 16].

Anyway, it was not until recently that antiferromagnets experienced their real breakthrough in the field of spintronics [12]. In 2016, it was found that the Néel order can be manipulated via electrical current pulses in some antiferromagnets with special magnetic and crystallographic symmetries via an intrinsic spin-orbit torque [10]. Shortly afterwards, it was shown that it is also possible to switch magnetic moments in any type of antiferromagnet by means of spin current induced torques [20]. Since then, there have been several studies reporting the successful manipulation of the Néel order in antiferromagnets [10, 20, 21, 22] as well as the observation of transport effects that had been only known to occur in ferromagnets previously [23, 24]. These results strongly suggest that magnetic information can actively be implanted to or extracted from antiferromagnets, paving the way for the newly emerging field of antiferromagnetic spintronics [12, 13, 14].

Having significant advantages over their ferromagnetic counterparts, antiferromagnets could replace the ferromagetic components in spintronic devices at some point in the (near) future. Due to their stability against external electric and magnetic fields, the information stored in antiferromagnets would be very well protected against pertubations. Furthermore, lacking a net magnetization, antiferromagnets do not produce stray fields. They provide ultrafast spindynamics with frequencies in the Terahertz regime, allowing for their manipulation on a pico second time scale [13]. Combined, these properties would make for a high-density memory with ultrafast operation speed [12]. On top of that, compared to the very limited variety of available ferromagnetic elements, there is a very broad range of antiferromagnetic materials that exhibit a stable Néel order at room temperature.

Lastly, it has been reported that antiferromagnetic insulators have very high spin diffusion lengths, yielding low power operation and possibly superfluid spin transport [25].

Even though there is a broad variety of antiferromagnetic materials, only few of them meet the criteria for possible integration into spintronic devices on a large-scale basis. For instance, in exchange bias systems the two most popularly used antiferromagnetic materials are MnIr and MnPt [26, 27], both featuring very rare elements that are expensive and difficult to extract [28, 29]. Hence, in the past years extensive research on alternative antiferromagnets replacing these materials has been performed [30]. In the case of antiferromagnetic switching, successful manipulation of the Néel order has been observed in epitaxially grown crystals of CuMnAs, MnAu or NiO up to now [10, 20, 21]. However, for a widespread application, polycrystalline materials that are easy to prepare, rare-earth free and thermally stable are necessary. Recently, an antiferromagnetic phase of the compound MnN was found to be a very promising candidate [31, 32].

In this work, antiferromagnetic MnN is investigated both as a passive component in exchange bias systems as well as in an active role in spin current induced electrical switching experiments. It has already been shown that film stacks consisting of polycrystalline Ta/ MnN/ CoFe trilayers yield an exchange bias effect that is comparable to or even higher than in MnIr and MnPt [31]. However, the thermal stability of exchange bias systems based on MnN is limited by nitrogen diffusion at high temperatures, respectively long annealing times [31, 33]. To enable routes towards a possible application, a better understanding about the diffusion processes and their consequences is crucial. Thus, in the first part of this work, the influence of the MnN thickness and the Ta buffer layer on the thermal stability and maximum exchange bias is investigated. In the second part of this thesis, spin-orbit torque induced switching of MnN is studied. This provides the possibility to investigate antiferromagnetic switching in a polycrystalline metal. To the best of the author's knowledge, this is the first time that spin-orbit torque induced antiferromagnetic switching is observed and studied in such a material.

Manganese Nitride

Manganese nitride is a compound that can be found in several different phases, depending on the ratio of manganese and nitrogen [34]. The four stable phases of Mn−N are summarized in Table 1.1, including their corresponding crystal structures. The $\theta-$MnN phase has a composition of Mn_6N_{5+x}, where x ranges from 0 to 1, depending on the exact nitrogen concentration. It is the most nitrogen-rich phase and is stable up to temperatures around 480° C. At higher temperatures, nitrogen diffuses out of the lattice and the $\eta-Mn_3N_2$ phase forms. Both the $\theta-$ and the $\eta-$phase of manganese nitride have antiferromagnetic ground states, with the $\eta-$phase showing higher anisotropy [35]. Going to temperatures higher than 575° C, the ζ-phase, yielding a composition of Mn_5N_2 or Mn_2N, arises. Here, the nitrogen content can vary between 36 % and 30 %. $\epsilon-Mn_4N$ is the least nitrogen-rich phase and the only one exhibiting a ferrimagnetic ordering with a Curie temperature of $T_C = 480°$ C [34].

While the θ- and the $\eta-$phase crystallize in an fct lattice, the $\zeta-$phase yields a hcp and the $\epsilon-$phase a perovskite structure. The data concerning the thermal stability of each Mn-N phase presented in Table 1.1 was determined by Suzuki et al. [36] via annealing reactively sputtered Mn−N films for two hours. It should be noted that even small variations of the nitrogen concentration, which may result from different preparation methods or parameters, can strongly influence the thermal stability and the lattice parameters. For instance, Gokcen et al. [34] found in their experiments that $\theta-$MnN can be stable up to 580° C, however with continuously decreasing nitrogen concentration for increasing temperatures.

Table 1.1: Composition, crystal structure and thermal stability of the four Mn−N phases [36, 37].

phase	composition	crystal structure	stable up to
ε	Mn_4N	perovskite structure	910° C
ζ	Mn_5N_2/Mn_2N	hexagonal-closed packed (hcp)	710° C
η	Mn_3N_2	face-centered tetragonal (fct)	575° C
θ	Mn_6N_5/MnN	face-centered tetragonal (fct)	480° C

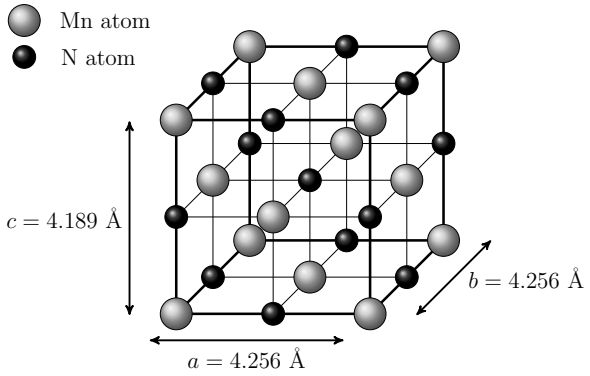

Figure 1.1: Schematics of the crystal structure of $\theta-$MnN [36].

In this work, the antiferromagnetic $\theta-Mn_6N_{5+x}$ phase is studied in the context of exchange bias systems as well as current induced switching experiments. For simplicity, the $\theta-$phase will be referred to as MnN in the following, even though it may not be completely saturated with nitrogen. In Fig. 1.1, the face-centered tetragonal crystal structure of $\theta-$MnN at room temperature is illustrated. The lattice parameters are a = b = 4.256 Å and c = 4.189 Å. MnN has a density of $\rho = 6.03\,\mathrm{g/cm^3}$ [36].

Often, there are some nitrogen atoms missing in the MnN lattice, leading to a composition of Mn_6N_{5+x} with $x < 1$. This is illustrated exemplarily in the two dimensional view on the MnN lattice in Fig. 1.2. Vacancies may be distributed randomly within the nitrogen sublattice [38]. The nitrogen concentration in the lattice has a strong influence on MnN's lattice parameters: with decreasing nitrogen content the lattice constants also decrease [36]. The magnetic structure of MnN is collinear of AFM-I type: The spins of the manganese atoms are aligned parallel within the c-plane and alternate along the c-direction.

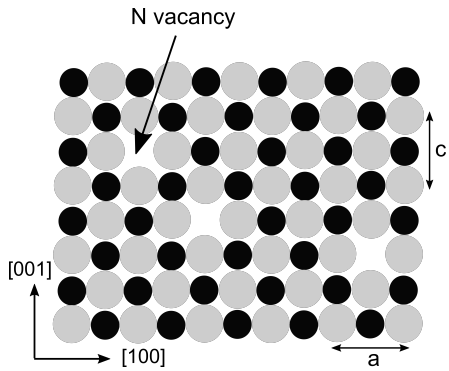

Figure 1.2: Illustration of vacancies in the nitrogen sublattice of MnN's crystal structure [38].

However, the orientation of the spins towards the c-plane is still controversial and might depend critically on the exact lattice constants: Suzuki et al. [36] found that the spins lie exactly in the c-plane when investigating fully saturated MnN [39]. In contrast, Leineweber et al. [35], working with nitrogen-poor MnN that consequently has smaller lattice constants, came to another conclusion. They found that at low temperatures, the spins are tilted about 22° away from the c-plane and converge towards it at increasing temperatures [35]. Again, the different results might be explained by the strong sensitivity towards the exact nitrogen content in the MnN lattice. Anyhow, both studies found a magnetic moment of 3.3 μ_B per Mn atom [39], which was also confirmed by density functional theory calculations [40]. The Néel temperature of MnN lies around $T_N \approx 380^\circ\,C$ [41]. Above T_N, the crystal structure transforms from a tetragonal to a cubic lattice, caused by magnetostriction [36].

Structure of this work

Following this introduction to the development of antiferromagnetic spintronics and the compound MnN studied in this work, Chapter 2 gives an overview about the most important experimental methods used for the sample preparation and characterization. Chapter 3 and Chapter 4 represent the two main parts of this work, including all experimental results. Chapter 3 deals with the integration of MnN into exchange bias systems. First, an introduction to the theory of the exchange bias effect is given, followed by a summary about previous results related to the use of MnN in exchange bias systems. Then, the results of two different studies performed on MnN exchange bias systems in the course of this work are presented. Chapter 4 considers spin current induced switching of MnN, starting with an introduction to the spin Hall effect, spin torques and the switching of antiferromagnets. After presenting the device preparation and the setup for electrical transport measurements, the results are discussed. To conclude, all main findings of this work are summarized in Chapter 5. Moreover, it is discussed which further challenges need to be overcome for the integration of antiferromagnetic MnN into spintronic devices.

Chapter 2

Experimental methods

In this Chapter, the experimental methods used for sample preparation and characterization in the course of this work are presented. Firstly, sputter deposition is introduced as the preparation technique, including a summary of the main properties of the used sputter chamber. Furthermore, the micropatterning process via lithography is presented. Following this, an overview about the methods used for sample characterization is given. X-ray diffraction is presented as a tool for structural analysis whereas MOKE is introduced for the magnetic characterization of the samples.

2.1 Sample preparation

2.1.1 Sputter deposition

For the preparation of thin films either physical (PVD) or chemical (CVD) vapor deposition can be used [42]. While CVD techniques rely on precurser molecules that are mixed with the source material to coat a sample, PVD simply works by vaporizing the source material [42]. Sputtering, which was used for sample preparation in this work, is a PVD method. The sputter process takes place in an ultra-high vacuum chamber as illustrated in Fig. 2.1. For the deposition process a sputter gas, usually Ar, is inserted into the chamber and a high DC voltage is applied between the cathode, consisting of the source material (target), and the anode, which is connected to the substrate. Due to the high negative voltage at the cathode, electrons are

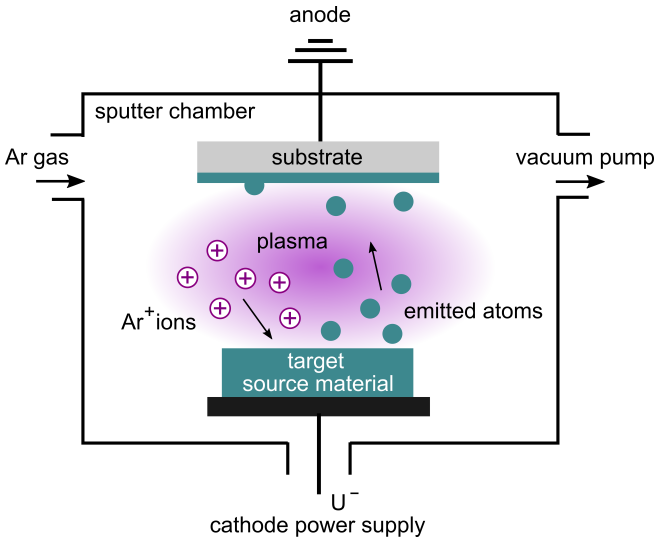

Figure 2.1: Schematic illustration of the sputter process inside a sputter chamber. Positively charged Ar ions are accelerated towards a target consisting of the source material. Hitting the target, they transfer momentum and knock out atoms. The emitted atoms then deposit on a substrate that is placed above the target.

emitted from the target and accelerated towards the anode, hitting and ionizing Ar atoms. This results in a glow discharge, igniting a plasma and starting the sputter process: Positively charged Ar ions are accelerated towards the cathode, hit the target and transfer their momentum to the target atoms. In case the momentum is large enough, the target atoms can overcome their binding energy and are knocked out. The emitted atoms then deposit on the substrate that is located above the target. The relation of ejected atoms to incoming ions is called the sputter yield, depending on the argon ion energy, the ions' incidence angle on the target and on the binding energy of the target atoms [43].

To ensure that the deposited film is as clear of impurities as possible it is crucial that the base pressure of the sputter chamber lies in the ultra-high vacuum regime. During the sputter process, the working pressure should not exceed values of 10^{-3} mbar to secure long enough mean free paths for the Ar ions and ejected atoms, preventing them from colliding with other

particles. However, those pressures are too low to allow for a stable plasma when working with a simple DC diode sputtering setup [43].

An advancement of the setup presented in Fig. 2.1 is so-called magnetron sputtering [44]. As an addition, magnets are installed beneath the target, generating a magnetic field of several hundred oersteds. When applying a voltage to ignite the plasma, electrons that are emitted from the target are forced to travel on circular paths due to the Lorentz force. Thus, they need to travel a greater distance on their way to the anode, increasing the probability of collisions with Ar atoms. This yields a higher ionization efficiency, which results in a decrease of the plasma's impedance, and makes it possible to work with lower voltages during the sputter process. Next to that, lower working pressures can be used due to the increased plasma concentration [45].

With a DC diode setup only conducting elements can be sputtered. In case sputtering of insulating materials is desired, special sputter sources coupled to an RF generator can be used [44]. Like for DC sputtering, Ar sputter gas is inserted into the chamber. When applying high frequencies around 13.56 MHz between the target and the anode, electrons move faster than the corresponding Ar ions due to their lighter mass. To compensate this charge imbalance, the target electrode biases negatively, forming a sheath potential on its surface. Consequently, Ar ions are accelerated towards the target, just as in the DC set up. Usually, a higher sputter gas concentration is needed to ignite a plasma in an RF than in a DC setup. RF sources can also be used to sputter conducting elements but corresponding sputter rates are always lower than in the DC setup [46]. To sputter compounds, either co-sputtering of different elements or sputtering from a target consisting of the composite material is possible. Moreover, by inserting an additional gas like nitrogen or oxygen into the chamber during the sputter process, compounds can form when gas molecules react with ejected atoms. This is called reactive sputtering.

All samples presented in this work were prepared with a sputter system designed by Bestec. The sputter chamber is equipped with four sputter sources; three DC sources and one RF source. The base pressure inside the

sputter chamber typically lies below 5×10^{-9} mbar. The working pressure varies around $2 \times 10^{-3} - 2.3 \times 10^{-3}$ mbar, depending on the source material. The substrate is fixed on a rotatable sample holder located centrically above the targets. During sputtering, the substrate rotation is set to 10 rounds per minute, allowing for a homogeneous distribution of the deposited atoms. To control the deposited layers' thicknesses, a quartz sensor is used to measure the deposition rate of each sputter target prior to deposition runs. The corresponding film thickness is defined by the deposition time, assuming a linear proportionality. Nitrogen or oxygen can be injected into the chamber for reactive sputtering.

2.1.2 Lithography

After preparation, it is often necessary to bring the sputtered films into certain geometrical shapes, like Hall bars, for electrical measurements. Lithography is the technique used for generating such a pattern on a substrate. It was developed within the rising field of semiconductor industry around 1960 [47]. Samples are coated with a polymeric resist that transfers an imprinted pattern onto the underlying films. Different types of lithography are distinguished based on the method of pattern imprinting.

Optical or photolithography is the oldest and still most commonly used technique [48, 49]. The corresponding process is illustrated in Fig. 2.2. First, the sample is coated with a resist. To spread the resist uniformly on the surface, the sample is rotated for $30 - 60$ s at a speed of $3000 - 7000$ rounds per minute. This fast rotation process is called spin coating. The rotation speed and duration define the resulting thickness and need to be adjusted depending on the type of resist that is used.

To clear the remaining casting solvents and bake-out the resist, the sample is put onto a heating plate for several minutes after the coating. Then, the fully prepared resist is exposed to UV light that is shone through a mask placed in close proximity above the sample. Each type of resist requires a specific exposure dose that is controlled by the exposure time and irradiance. In the exposed regions that are not protected by the mask, a radiation pattern is

generated. Here, the UV light induces chemical changes to the resist, changing its solubility [42]. Depending on the type of resist that is used, those parts will be either less dissolvable (negative resist) or more dissolvable (positive resist).

After the pattern has been imprinted, the resist needs to be developed. Therefor, the sample is brought in contact with a resist-specific developer by immersion. During this step, the exposed regions of negative resist (left-hand side of Fig. 2.2) remain on the sample whereas they dissolve when positive resist (right-hand side of Fig. 2.2) is used, respectively. Next, the resulting pattern has to be transferred to the underlying film. This can be realized via etching with Ar ion bombardment. In a vacuum chamber, the sample is exposed to a plasma where Ar ions are accelerated towards its surface and knock out atoms, similarly to sputtering. In regions protected by the resist, the films remain on the substrate. The process is monitored with a mass spectrometer that provides real-time information about the etching depth. In a final step, the sample is cleaned and the remaining resist is removed with acetone and

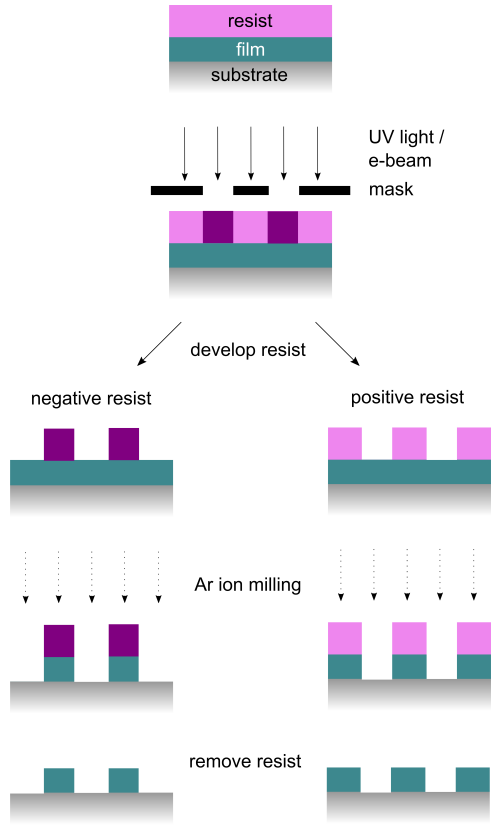

Figure 2.2: Schematic illustration of a lithography process, using either negative or positive resist. The sample is coated with the resist and then exposed to UV light or an electron beam. Depending on the type of the resist, the exposed areas remain or dissolve after development. Via Ar ion milling the exposed film is etched off. Lastly, the resist is removed.

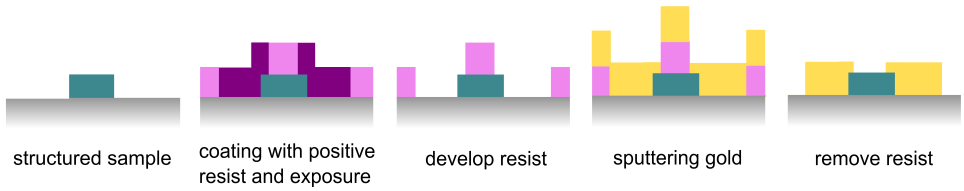

Figure 2.3: Illustration of a lithography process for the deposition of Au contact pads. The structured sample is coated with positive resist and then exposed with UV light or an e-beam. After development, Au is sputtered onto the sample. When the resist is removed, the Au remains in the areas that were previously defined by the resist.

ethanol. The whole lithography process can then be repeated if contact pads or more complicated patterns are required. The presented type of photolithography based on proximity printing is restricted to a resolution of $2-4\,\mu$m [48]. However, some setups and techniques require even smaller or more precise structures that have to be imprinted by other lithography methods.

To achieve higher resolution, e-beam lithography can be used [48, 50]. Here, a focused electron beam is used to imprint the desired pattern to the resist. This is done by placing the coated sample into a scanning electron microscope (SEM) and directly exposing the resist by the electron beam in the desired regions. This way, no mask is needed. Even arbitrary geometries and complicated structures can thus be printed very precisely. E-beam lithography provides a resolution around 10 nm and can reach even smaller values in optimized setups [50]. All further production steps described in the previous paragraph remain unchanged. As the resulting structures are very small, contact pads need to be added in a second lithography process when following electrical measurements are desired. Therefor, positive resist is used to define larger areas contacting the previously generated structures as illustrated in Fig. 2.3. After development, a well-conducting element such as Au, together with a supporting layer of Ta ensuring adhesion, is sputtered onto the sample. When the resist is removed at the end of the process, the conducting material only remains in the defined areas.

2.2 Sample characterization

2.2.1 X-ray diffraction

X-ray diffraction is a widespread and well-known technique to determine the crystallographic properties of a material [51, 52]. For x-rays to interfere constructively after scattering off a crystal lattice, Bragg's law needs to be fulfilled:

$$\lambda = 2 \cdot d_{hkl} \cdot \sin(\theta). \tag{2.1}$$

Here, λ denotes the wavelength of the x-rays, θ the incidence angle and d_{hkl} the spacing between the lattice planes. In cubic systems, d_{hkl} is related to the lattice constant a via

$$d_{hkl} = \frac{a}{\sqrt{h^2 + k^2 + l^2}}, \tag{2.2}$$

where h, k, and l are the Miller indices. Thus, when a reflection occurs under a specific angle θ, the corresponding lattice constant of the material can be calculated, assuming the wavelength λ is known. Even though Bragg's law reveals the angles under which reflection peaks appear, it does not provide information about the corresponding intensity. Therefor, the so-called structure factor has to be taken into account. It relates to the electron density and the phase factor of a diffraction and is given by

$$F_{hkl} = \sum_j f_j \cdot \exp(2\pi i(hx_j + ky_j + lz_j)), \tag{2.3}$$

where f_j is the atomic form factor that is specific for each element and contains anomalous scattering contributions [53]. x, y, and z denote the interior coordinates of the crystal's unit cell. The square of F_{hkl} is proportional to the intensity of the reflection from the lattice plane (hkl):

$$|F_{hkl}|^2 \ \propto \ I_{hkl}. \tag{2.4}$$

As a result of the lattice's symmetry, the structure factor equals zero for certain combinations of x, y and z. This gives rise to a second condition for reflections to be observable in x-ray diffraction measurements. For each

Bravais-lattice, extinctions rules can be determined. The crystal structure of $\theta-$MnN, which is investigated in the course of this thesis, is a tetragonally distorted variant of the NaCl lattice. Thus, it is built up by two face-centered cubic (fcc) lattices that are shifted towards each other. For an fcc lattice, reflections from lattice planes (hkl) are only observable when all of h, k, and l are equal or all of them are odd numbers [51].

For this work, x-ray diffraction measurements were performed with a PHILIPS X'PERT PRO MPD instrument equipped with Cu-K_α radiation and Bragg-Brentano optics. Here, the easiest way extract information about the crystal structure of a sample is to perform a Gonio-scan. The setup and geometry are shown in Fig. 2.4: The angle θ between the x-ray source and the sample surface is varied to scan a defined angular range for reflections. To detect the diffraction pattern, a detector measures the reflected beam under the angle 2θ. While the incidence angle is varied, the detector moves about the same angle in the same time, such that the detection angle is always similar to the incidence angle while the sample does not move. Whereas the diffraction measurement of an ideal, half-infinite crystal would result in reflection peaks in the shape of delta-functions, detected peaks from real samples usually show a broadening that originates from the crystallites' size and strain as well as contributions from the instrument itself [54]:

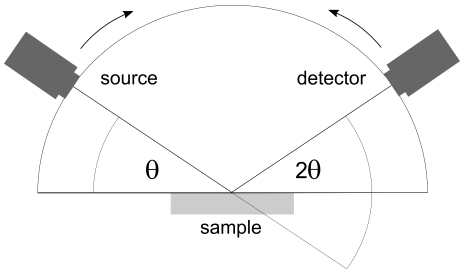

Figure 2.4: Schematic setup of the x-ray diffractometer for a $\theta - 2\theta$ Gonio-scan. The source and the detector move towards each other with the same speed, so that the detection angle is constantly 2θ.

$$B^2_{\text{integral}} = B^2_{\text{instrument}} + B^2_{\text{size and strain}}. \tag{2.5}$$

To further investigate the crystalline quality of a sample, so-called rocking curves can be detected [51]. This technique provides information about the orientation of the single crystallites. The source and the detector are set to an

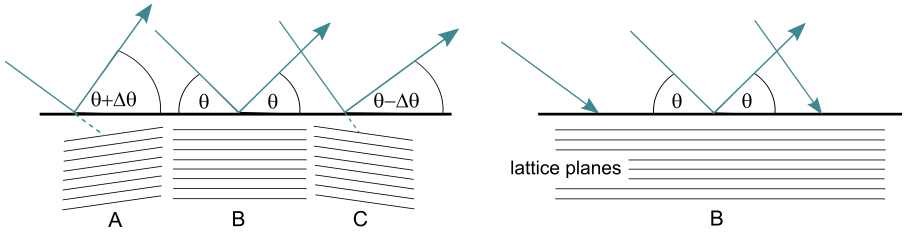

Figure 2.5: Schematic lattice planes illustrating the origin of a rocking curve. On the left-hand side, a film with differently orientated crystallites (A), (B) and (C) is shown. Crystallite (B) is aligned parallel to the film plane, thus it reflects incoming beams under an angle θ. As there are other crystallites like (A) and (C), not orientated perfectly parallel to the plane, the incoming beam is also reflected for angles slightly smaller and higher than θ and a broad rocking curve emerges. In case all crystallites are aligned parallel to the sample plane as presented on the right-hand side, the incoming beam is only reflected under the angle θ [51].

angle θ and 2θ, respectively, where a reflection has been observed. In contrast to a Gonio-scan, where the source and the detector move towards each other, their interjacent angle is held constant for the rocking curve measurement. The incidence angle ω is varied about a small range $\Delta\omega = \theta \pm \Delta\theta$. In case the sample consists of different crystallites that are not all orientated in the same manner, corresponding reflections at angles slightly smaller and larger than θ are detected, as illustrated on the left-hand side of Fig. 2.5. If the incidence angle is smaller than θ, crystallite (A) that is tilted towards the normal of the sample plane reflects the incoming x-rays. If it is greater, crystallite (C) fulfills the condition for constructive interference. Crystallite (B) is orientated parallel to the sample plane, thus reflecting the beam exactly at θ. Each of these three reflections results in the detection of a peak at $\theta \pm \Delta\theta$ with varying intensity. As there are not only three but many more non-perfectly orientated crystallites in a real sample, the distribution of the different reflections leads to one broad rocking curve.

On the right-hand side of Fig. 2.5, a crystal structure yielding a narrow rocking curve is shown. There is only one crystallite orientated completely parallel to the sample plane, resulting in a reflection at θ. As no other crystallites are present, the beam cannot be reflected at smaller or higher angles [51].

2.2.2 MOKE

The magneto-optic Kerr effect (MOKE) is a fairly simple and fast tool to obtain information about the basic magnetic properties of a sample. In 1877, John Kerr [55] discovered that linearly polarized light reflected by a ferromagnetic material experiences a rotation of the polarization plane. Since this rotation is proportional to the ferromagnet's magnetization, MOKE is nowadays commonly used to investigate magnetic thin films, for example to detect ferromagnetic hysteresis loops [16].

To describe the origin of the magneto-optic Kerr effect it can either be discussed on a micro- or macroscopic level. Microscopically, MOKE results from spin-orbit interactions of electrons' spins in a ferromagnetic material with the linearly polarized light that travels through it. This requires a full quantum mechanical description as can be found in [56] and will not be further discussed here. Macroscopically, MOKE can be considered in terms of the dielectric properties of a medium. Linearly polarized light can be separated into right and left circularly polarized parts. In ferromagnetic materials, these parts exhibit slightly different propagation velocities. Thus, when linearly polarized light interacts with a ferromagnetic specimen, i.e. when it is reflected by a ferromagnetic sample, a phase shift of the left and right circularly polarized parts occurs. Consequently, this leads to a rotation of the polarization plane in the reflected beam, that is called the Kerr rotation θ_K. Furthermore, as right and left circularly polarized parts also have different absorption coefficients in ferromagnetic materials, changes to the ellipticity

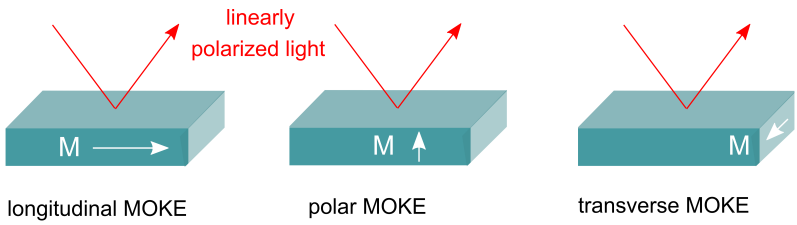

Figure 2.6: Illustration of the three different geometries that yield the longitudinal, polar, or transverse magneto-optic Kerr effect.

e_K are induced on top of the Kerr rotation. In summary, these variations gives rise to a complex Kerr rotation

$$\Theta_K = \sqrt{\theta_K^2 + e_K^2}. \tag{2.6}$$

Θ_K is connected to the dielectric tensor $\varepsilon_{\alpha\beta}$ [57], whose off-diagonal components contribute to the complex Kerr rotation in dependence on the orientation of the incident beam towards the sample's magnetization. In Fig. 2.6, the three possible orientations and resulting Kerr effects are presented. In the case of incident light perpendicular to an in-plane magnetization (longitudinal MOKE), Θ_K is proportional to ε_{xz}. In the absence of a magnetic field, i.e. in non-(ferro)magnetic materials, the off-diagonal components become zero and the Kerr rotation vanishes [57, 16].

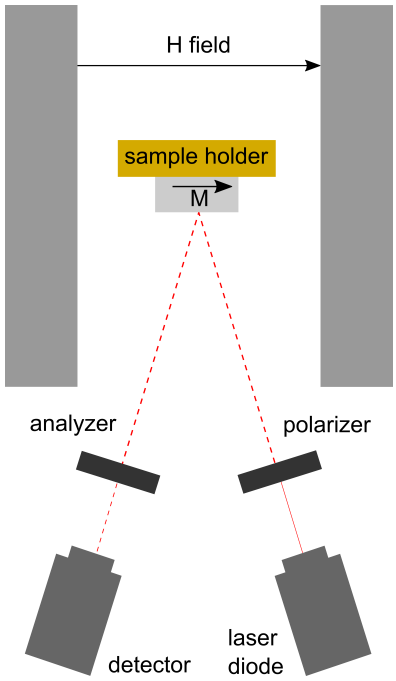

Figure 2.7: Illustration of the MOKE setup as used for measurements in this work. A laser beam is polarized and reflected by a ferromagnetic sample that is placed into a magnetic field. The reflected beam is lead through an analyzer and then detected by a photodiode.

Fig. 2.7 illustrates the MOKE setup that was used for the detection of hysteresis loops in the course of this work. Longitudinal as well as polar MOKE can be measured. The sample is placed onto a sample holder between two electric coils that generate an external magnetic field up to 2 T. For a typical MOKE measurement, a laser with a wavelength of 650 nm is focused on the sample and calibrated such that it reflects into the detector. A polarizer installed behind the laser diode ensures that only linearly polarized light reaches the sample. The reflected beam is lead through an analyzer before its intensity is detected by a photo diode. To measure the Kerr rotation, the analyzer is set to a fixed angle Θ_0, enabling the measurement of intensity variations associated with the rotation of the polarization plane via

$$\Delta I(\Theta_\mathrm{K}) = I_0 \cdot \cos^2(\Theta_0 \pm \Theta_\mathrm{K}) \tag{2.7}$$

according to Malus' law [58]. This way, the detected intensity variations can easily be converted to the corresponding Kerr rotation. Additionally, for the sake of better comparability, the normalized Kerr rotation is calculated for each loop by the measurement software. At this point, it should be emphasized that the Kerr rotation is only proportional to the sample's magnetization and does not yield any information about absolute values like the saturation or remanent magnetization. However, for this work, MOKE was mainly used for the detection of exchange bias fields. Corresponding values are obtained by measuring the shift of a hysteresis curve towards negative fields. Hence, absolute magnetization values are not necessary.

Chapter 3

MnN in exchange bias systems

In this Chapter, all results concerning the use of MnN in exchange bias systems are presented. As an introduction, an overview about the different models used to describe the exchange bias effect is given. This is followed by a summary of the preliminary work that has been performed on exchange bias systems with MnN. Thereafter, the results of two different independent studies of MnN based exchange bias stacks are presented, separated into two different Sections. Both Sections first introduce the corresponding sample preparation parameters before the results are discussed.

The first study deals with investigating high-temperature annealing of Ta/ MnN/ CoFe exchange bias stacks with particularly thick MnN films [59]. Detailed annealing series of exchange bias systems with varying MnN thickness are presented, including depth profile monitoring of the nitrogen diffusion via Auger electron depth profiling and polarized neutron reflectometry. In the second study, the focus is laid on the seed layer used in Ta/ MnN/ CoFeB exchange bias systems [60]. Results of a detailed Ta thickness dependence and the effects of introducing a TaN diffusion barrier are discussed.

3.1 Introduction

3.1.1 The exchange bias effect

In 1956, Meiklejohn and Bean [61] first discovered the phenomenology of the so-called exchange bias effect. Studying ferromagnetic (FM) Cobalt particles with an antiferromagnetic (AFM) oxide shell, they found that an anisotropy is induced in the ferromagnet via an interface coupling to the antiferromagnet. The effect vanishes when the system is heated above the respective Néel temperature of the antiferromagnet. The anisotropy that is induced in the ferromagnet leads to a shift of its hysteresis curve, which is nowadays often exploited in thin film devices, like GMR or TMR systems, to pin a ferromagnetic layer. As only one preferred direction is generated instead of the usual two-fold symmetry of an easy axis, this exchange coupling is often referred to as unidirectional anisotropy.

The origin as well as the characteristics of the exchange bias effect can be discussed within different models, which are presented in the following [16]. However, up to now, several properties of exchange bias are still under debate and a full quantitative model that explains its formation and all its features on the microscopic scale does not yet exist.

Ideal Meiklejohn-Bean model

For the activation of exchange bias, a FM/ AFM bilayer system is heated above the antiferromagnet's Néel temperature T_N as presented in Fig. 3.1 a). The ferromagnet's Curie temperature T_C has to be higher than the corresponding Néel temperature of the antiferromagnet, ensuring that its magnetic moments are still aligned and respond to an externally applied magnetic field H_{ext} at the chosen annealing temperature. Hence, the antiferromagnet's spins lose their magnetic orientation while the ferromagnetic order is maintained. After bringing the FM/ AFM system into this state, the temperature is decreased again to values smaller than T_N. During this so-called field cooling process, the spins in the antiferromagnet align parallel to the ferromagnetic ones at the FM/ AFM interface due to the presence of H_{ext}. Accordingly, the antiferromagnet's spins are aligned alternately parallel or antiparallel with

respect to the ferromagnet when the antiferromagnetic order is regained below T_N. As a consequence of this interface coupling, the ferromagentic order is now more stable against external magnetic pertubations: Higher magnetic fields are necessary to rotate the ferromagnetic spins near the interface from their initial, preferred, orientation [16].

This pinning makes the total magnetization less sensitive to external magnetic fields and results in a shift of the ferromagnet's hysteresis curve as illustrated in an exemplary hysteresis loop in Fig. 3.1 b). An exchange bias system is

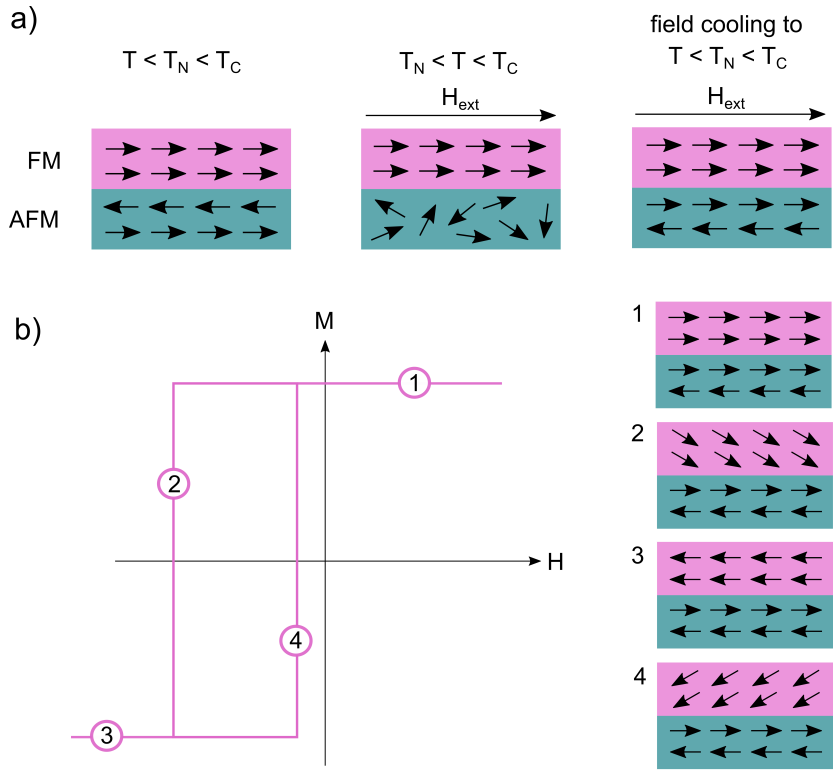

Figure 3.1: Simplified illustration of the magnetic order during the a) Activation of exchange bias and b) Magnetization reversal in an exchange bias system. After field cooling (FC), the ferromagnetic spins are coupled to the antiferromagnet, resulting in a shift of the hysteresis curve. Steps 1) to 4) in part b) illustrate the magnetic orientation for four different magnetic field values [16].

brought into an external magnetic field parallel to the pinning direction (1). When changing the magnetic field direction, the ferromagnet's magnetization does not follow directly. Only when going to higher field values, the ferromagnetic moments begin to follow (2) and finally align parallel to the external field (3). In contrast, reducing the field again, the moments begin to rotate back to their preferred direction before the external field direction is even switched (4). The unidirectional anisotropy induced by the exchange bias coupling yields a torque acting on the ferromagnetic spins in all orientations that are different from the initial preferred one. The stronger the interface coupling, the further the hysteresis is shifted from the zero-crossing. The value about which the center of the hysteresis is shifted is called the exchange bias field H_{eb}.

In most systems, the direction to which the hysteresis is shifted, i.e. the sign of exchange bias, is opposite to the field cooling direction (negative exchange bias). Only for a few systems using antiferromagnets with very low anisotropy exceptions exhibiting positive exchange bias have been observed [16, 62, 63].

This model provides the easiest and most demonstrative way of describing exchange bias. However, several assumptions are made about the FM/ AFM bilayer system that do not hold for real exchange bias systems: The ferromagnetic as well as the antiferromagnetic layer are considered to have a perfectly smooth interface, both are supposed to be in a single domain state, the spins of the ferromagnet are only allowed to rotate as a whole, not independently, and the antiferromagnet's spins are assumed to be rigid. Within these limitations, the exchange bias field is given by

$$H_{\mathrm{eb}}^{\mathrm{ideal}} = \frac{J_{\mathrm{eb}}}{\mu_0 M_{\mathrm{FM}} t_{\mathrm{FM}}}, \tag{3.1}$$

where the parameter J_{eb} measures the interfacial exchange energy per unit area, thus defining the magnitude of the interface coupling. μ_0 depicts the vacuum permeability, M_{FM} the magnetization of the ferromagnetic layer and t_{FM} its thickness [16]. Regarding the numerous initial assumptions about the FM/ AFM system it is not surprising that the calculated values $H_{\mathrm{eb}}^{\mathrm{ideal}}$ do not agree well with experimentally determined exchange bias fields. Often,

the calculated values are way too high. Moreover, the ideal Meikeljohn-Bean model does not account for the experimentally observed increase of the ferromagnet's coercive field H_c in exchange biased layers and it cannot provide information concerning the dependence of exchange bias on the antiferromagnet's thickness [16, 19].

Realistic Meiklejohn-Bean model

The realistic Meiklejohn-Bean model advances from the ideal model in terms of allowing rotatable magnetic moments in the antiferromagnet [16]. However, the antiferromagnet's spins are not supposed to rotate separately, but only as a whole during magnetization reversal. Adding this new degree of freedom allows to impose certain requirements on the antiferromagnet which need to be fulfilled to generate exchange bias. The parameter R is introduced, accounting for all properties of the antiferromagnet. It denotes the ratio of the antiferromagnet's anisotropy K_{AFM} and thickness t_{AFM} to J_{eb} via

$$R = \frac{K_{\mathrm{AFM}} t_{\mathrm{AFM}}}{J_{\mathrm{eb}}} \tag{3.2}$$

and needs to be equal to or larger than unity for exchange bias to be observable. When this condition is fulfilled, the antiferromagnetic moments rotate reversibly during magnetization reversal of the ferromagnet. The higher R, the closer the observed exchange bias approaches the corresponding ideal value $H_{\mathrm{eb}}^{\mathrm{ideal}}$. Furthermore, the shape of the ferromagnet's hysteresis at magnetization reversal sharpens with increasing R. In the range of $R \geq 1$, the coercive field is found to be zero within the frames of this model. However, when going down to values of $R < 1$, no exchange bias but a non-zero and increased coercive field is observed. Here, the antiferromagnetic moments follow the ferromagnet but their rotation is no longer reversible [16].

Finally, within the realistic Meiklejohn-Bean model, the exchange bias field can be calculated via

$$H_{\mathrm{eb}} = H_{\mathrm{eb}}^{\mathrm{ideal}} \cdot \sqrt{1 - \frac{1}{4R^2}}. \tag{3.3}$$

Thus, $H_{\mathrm{eb}}^{\mathrm{ideal}}$ is consequently lowered when R approaches unity. Unfortunately, the corresponding values are still too high to agree with experimental results [16].

Nevertheless, assuming fixed values for J_{eb} and K_{AF}, a critical layer thickness of the antiferromagnet can be defined via Eq. (3.2):

$$t_{\mathrm{AFM}}^{\mathrm{crit}} = \frac{J_{\mathrm{eb}}}{K_{\mathrm{AFM}}}. \tag{3.4}$$

For smaller thicknesses, no exchange bias but only an enlargement of the coercivity is observed. For $t_{\mathrm{AFM}} \geq t_{\mathrm{AFM}}^{\mathrm{crit}}$, exchange bias sets in and grows with increasing thickness until a saturation is reached finally [16]. Furthermore, Eq. (3.4) shows that an increase of the antiferromagnet's anisotropy yields a reduction of $t_{\mathrm{AFM}}^{\mathrm{crit}}$, which can be crucial when integration of exchange bias systems into thin film applications is desired.

Domain wall model

In order to diminish the discrepancy between measured and calculated field values, Mauri et al. [64] introduced a new model for exchange bias in 1987, proposing that a domain wall forms at the FM/ AFM interface during magnetization reversal. The experimentally observed loss of coupling energy would thus be related to the formation of the domain wall, accounting for the small values of H_{eb}. Again, some assumptions about the exchange bias system are made: Both the antiferromagnet and the ferromagnet are supposed to be in a single domain state and the antiferromagnetic layer is assumed to have a uniaxial anisotropy. The domain wall is considered to form near the FM/ AFM interface, either in the ferromagnetic or the antiferromagnetic layer, depending on where it is energetically more favorable. Supposing that the exchange energy is spread over one domain wall with a thickness of about $\pi\sqrt{A_{\mathrm{AFM}}K_{\mathrm{AFM}}}$, the exchange bias field is then given by:

$$H_{\mathrm{eb}} = \begin{cases} 2\sqrt{\dfrac{\sqrt{A_{\mathrm{AFM}}K_{\mathrm{AFM}}}}{M_{\mathrm{S}}t_{\mathrm{FM}}}} & \text{for strong interface coupling and} \\ \dfrac{J_{\mathrm{ex}}}{M_{\mathrm{S}}t_{\mathrm{FM}}} & \text{for weak interface coupling.} \end{cases} \tag{3.5}$$

Here, the exchange stiffness A_{AFM} is introduced as a new material specific parameter of the antiferromagnet [65].

As an expansion of the Mauri model, Kim and Stamps [66, 67] proposed the concept of partial domain walls in the antiferromagnet instead of a planar one at the FM/ AFM interface. Even though this does not change the analytic expression for H_{eb}, the model assigns the experimentally observed increased coercivity in exchange biased ferromagnetic layers to domain wall pinning at magnetic defects and impurities, yielding an additional energy barrier. This pinning might also be the reason for asymmetries in measured hysteresis.

Temperature dependence

In the context of temperature dependence of exchange bias it is crucial to distinguish between the annealing temperature T_{A}, at which the exchange bias is set, and the measurement temperature T_{M}. Several different parameters with diverse temperature dependencies like the ferromagnet's and antiferromagnet's anisotropies and the interfacial coupling energy have to be considered, making it complicated to develop a universal model. Most calculations predict that the exchange bias field decreases monotonically with increasing temperature T_{M}. The coercive field does also decrease with increasing temperature, however this is only valid in the lower temperature range. Then, it exhibits a peak at higher temperatures before it declines again [68]. When approaching T_{N}, the exchange bias as well as the coercive field decline to zero.

However, experimental observations in exchange bias systems often reveal a temperature dependence that does not fully agree with the above-mentioned characteristics. Usually, the exchange bias starts to decline at temperatures that are much lower than the antiferromagnet's Néel temperature. Accordingly, to define the temperature above which exchange bias is no longer detected, the so-called blocking temperature T_{B} is introduced [69]. In return, this means that for the activation of exchange bias it is not necessary to perform field cooling from temperatures higher than T_{N} in most FM/ AFM systems. Usually, it is sufficient to anneal the system at temperatures that are higher than its corresponding blocking temperature [69].

Polycrystalline exchange bias systems

Exchange bias can be observed in many different types of samples and materials. Up to now, the highest values have been reported for polycrystalline FM/ AFM bilayer systems [69]. Polycrystalline films have quite rough interfaces that yield both magnetic and structural disorder. Furthermore, it has to be taken into account that both the antiferromagnetic and the ferromagnetic layer consist of different grains which are assumed to be in a single domain state in thin magnetic films. In order to include these characteristics correctly, several models for exchange bias in polycrystalline films have been developed [69].

The first theory for polycrystalline systems was proposed by Stiles and McMichael in 1999 [70]. Assuming that the temperature dependence of exchange bias arises from thermal instabilities of the single antiferromagnetic grains, they could model systems where the ferromagnet's Curie temperature is significantly smaller than the antiferromagnet's Néel temperature. Here, the antiferromagnetic grains remain in a stable magnetic state during magnetization reversal of the ferromagnet if the measurement temperature is low enough. However, thermal excitations of the grains can occur at higher temperatures. Therefor, the energy barrier

$$E_{\mathrm{B}} = V_{\mathrm{g}} K_{\mathrm{AFM}} \tag{3.6}$$

has to be overcome, depending both on the grain volume V_{g} and the grain's anisotropy K_{AFM} [71]. The probability of switching a grain at a given temperature is then given by the Néel-Arrhenius law

$$\tau = f_0^{-1} \exp\left(\frac{E_{\mathrm{B}}}{k_{\mathrm{B}} T}\right), \tag{3.7}$$

where k_{B} is the Boltzmann's constant and τ denotes the relaxation time, which is usually identified with the annealing time for exchange bias systems. The antiferromagnetic resonance frequency f_0 is usually taken to be $10^{12}\,\mathrm{s}^{-1}$ [69]. Accordingly, each grain has its own blocking temperature, depending on its size and anisotropy. This yields a broad blocking temperature distribution that can be determined via reversed field cooling experiments as presented

in [69]. The median blocking temperature $< T_B >$ is related to the anisotropy of the antiferromagnetic film via

$$K_{AFM}(< T_B >) = \frac{\ln(\tau f_0)}{V_m} k_B < T_B >, \tag{3.8}$$

where

$$V_m = \frac{\pi t_{AFM} D_m^2}{4} \tag{3.9}$$

defines the median grain volume according to the median grain diameter D_m [69]. Anyway, it can be stated that the median blocking temperature increases with increasing anisotropy and grain size, which again depends on the thickness of the antiferromagnet, yielding a higher anisotropy in thinner films.

3.1.2 Previous results

Over the last years, antiferromagnetic MnN has been intensively studied concerning its use in exchange bias systems. Meinert et al. [31] found that MnN can induce hysteresis shifts of up to $H_{eb} = 1800\,\text{Oe}$ at room temperature in reactively sputtered polycrystalline MnN/ CoFe exchange bias systems. Optimized bilayers with $t_{MnN} = 32\,\text{nm}$ and $t_{CoFe} = 1.6\,\text{nm}$ yield an effective interfacial exchange coupling energy of $0.41\,\text{mJ/m}^2$. In Fig. 3.2, the corresponding dependence of the exchange bias field on the MnN and CoFe thickness is displayed. The highest exchange bias is obtained for thicknesses of $t_{MnN} \approx 30$ nm, which is a rather high value with regard to other antiferromagnets commonly used for exchange bias. For comparison, MnIr generates maximum H_{eb} with a thickness around 7 nm [72]. Below $t_{MnN} \approx 12$ nm, no exchange bias is observable. Accordingly, this marks the critial layer thickness.

With increasing thickness of the ferromagnet the exchange bias field decreases, as commonly observed in exchange bias systems. CoFe thicknesses around $t_{CoFe} = 1.6\,\text{nm}$ provide high exchange bias as well as sufficiently good reproducibility and stability at the same time. Furthermore, it has been shown that MnN can generate perpendicular exchange bias using even thinner ferromagnetic layers and corresponding field annealing [32]. Exchange bias values of more than 3500 Oe have been observed in those systems.

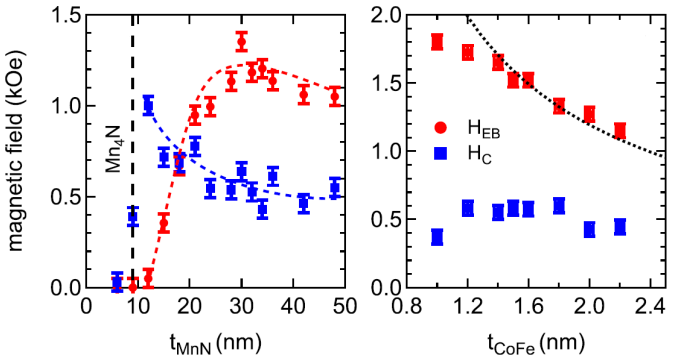

Figure 3.2: Exchange bias H_{eb} and coercive field H_{c} in dependence on the MnN (left) and CoFe (right) thickness for samples annealed at $T_{\mathrm{A}} = 325°\mathrm{C}$ for 15 min [31], measured at room temperature.

As discussed in Chapter 1, the nitrogen concentration in the MnN lattice plays a crucial role in terms of thermal stability. This has also been observed by Meinert et al. investigating exchange bias systems based on MnN films with different nitrogen contents [31], as presented in Fig. 3.3. These annealing series show the exchange bias field after successive annealing and field cooling of samples with varying nitrogen content in a vacuum furnace. Clearly, the generated exchange bias starts to decrease after annealing at lower temperatures for samples with nitrogen-poor MnN. However, the exchange bias system with nitrogen-rich MnN is stable up to annealing temperatures around $T_{\mathrm{A}} = 425°\,\mathrm{C}$.

During the annealing processes nitrogen diffuses out of the MnN film. Therefore, a sufficiently large nitrogen reservoir is crucial for good thermal stability. The percentages given in each window of Fig. 3.3 represent the nitrogen to argon ratio during the sputter process, i.e. 40 % relates to 40 % N_2 and 60 % Ar. Using 55 % nitrogen for the preparation of MnN yields exchange bias systems that show a significant increase of exchange bias after annealing at temperatures higher than $T_{\mathrm{A}} = 400°\,\mathrm{C}$. This behavior is not observable in the other investigated samples and thus supposedly connected to the nitrogen content in the MnN lattice. Moreover, it strikes that all samples, independent of the nitrogen content, exhibit a local minimum of exchange bias around $T_{\mathrm{A}} = 200°\,\mathrm{C}$. This behavior is quite unique and cannot be explained within

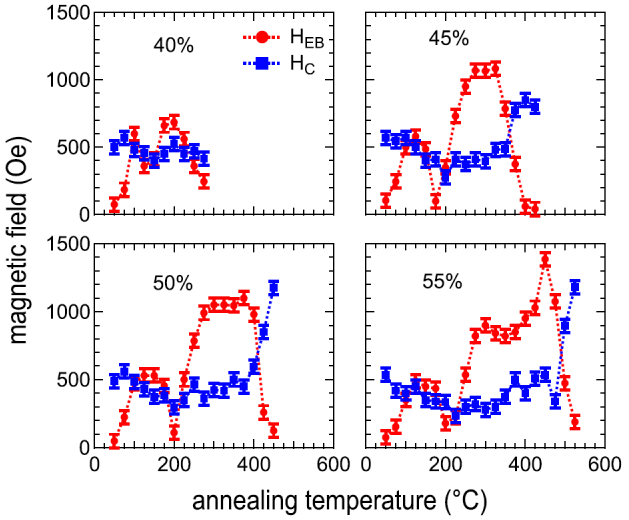

Figure 3.3: Exchange bias H_{eb} and coercive field H_{c} in dependence on the nitrogen content in the lattice after successive annealing for 15 min, measured at room temperature. The percentage depicts the gas ratio of N_2 to Ar during sputtering [31].

the usual models of exchange bias up to now. The blocking temperature of an optimized MnN/ CoFe system lies around $T_{\mathrm{B}} = 160^{\circ}\,\mathrm{C}$ for $t_{\mathrm{MnN}} = 30$ nm, which was determined via a reversed field cooling study [31, 69].

Via transmission electron microscope (TEM) imaging, Sinclair et al. [73] found that the median grain diameter in a 30 nm thick reactively sputtered polycrystalline MnN film is $D_{\mathrm{m}} = 4.8\,\mathrm{nm}$. Compared to values for the commonly used antiferromagnet MnIr ($D_{\mathrm{m,\ MnIr}} \approx 10\,\mathrm{nm}$), this is a rather small diameter for such a thick film [74]. In terms of enhancing the thermal stability it could be beneficial to increase the grain diameter of MnN. However, the study also revealed that MnN has a similar anisotropy constant to MnIr, lying in the range of $0.6 - 2.9 \times 10^7\,\mathrm{erg/cm^3}$. Yet, thermal stability of the grains at room temperature is only guaranteed when film thicknesses of more than 20 nm MnN are used [73].

In an effort to improve the thermal stability, doping MnN with elements that strengthen the nitrogen bonds, thereby reducing the loss of nitrogen through

diffusion during annealing, has been investigated [33]. Suitable dopant candidates with negative defect energies were calculated via density functional theory. It was found that doping with these elements indeed leads to an enhanced thermal stability in terms of stable exchange bias after annealing at high temperatures. The best results were obtained by doping MnN with a very small amount of Y ($< 2\,\%$), yielding high exchange bias of more than 1000 Oe for annealing temperatures up to $T_\mathrm{A} = 485^\circ$ C. This relates to an increased thermal stability of nearly 100° C. Unfortunately, this improved stability is accompanied by lower total exchange bias values due to worsened crystallinity, resulting in smaller ratios of $H_\mathrm{eb}/H_\mathrm{c}$ throughout all investigated dopants.

3.2 Large increase of exchange bias in MnN/CoFe systems after high-temperature annealing

In the course of the previous investigations, summarized above, almost exclusively exchange bias systems with a thickness of 30 nm MnN have been studied. This value was chosen based on the thickness dependence of exchange bias, and annealing series investigating the thermal stability have been performed accordingly. For possible integration into spintronic devices, it would certainly be beneficial to reduce the MnN thickness to minimize the size of the whole exchange bias stack. However, thinner MnN films naturally have smaller grains, decreasing the anisotropy and thermal stability. Furthermore, assuming that a more or less constant amount of nitrogen diffuses out of the MnN film during annealing, the resulting nitrogen deficiency would be more severe the thinner the MnN gets.

Following these considerations, it might be interesting to look at exchange bias stacks with even thicker MnN films to improve the thermal stability. Even though those stacks would not necessarily be suited for device integration, they could provide important insight concerning some of the system's properties. Hence, for this study, exchange bias samples with MnN thicknesses exceeding the usual 30 nm were prepared and investigated in terms of high-temperature annealing to test whether the exchange bias is stable up to higher annealing temperatures.

3.2.1 Sample preparation

Since exchange bias systems based on MnN have already been investigated in the course of previous projects, the optimized preparation parameters could be adopted for this work [31]. All samples, following the setup depicted in Fig. 3.4, were prepared via DC magnetron sputtering at room temperature in a BESTEC sputter system (cf. Chapter 2.1.1). The base pressure of the sputtering system was around 5×10^{-9} mbar prior to the deposition runs. The MnN films were reactively sputtered from an elemental Mn target with a gas ratio of 50 % Ar to 50 % N_2 at a working pressure of $p_w = 2.3 \times 10^{-3}$ mbar, holding the total gas flow constant at 11.5 sccm. The working pressure was

set to slightly higher values than usual for this sputter system, ensuring a stable plasma in the nitrogen atmosphere. The typical deposition rate of MnN was 0.1 nm/s at a source power of 50 W. The ferromagnetic film was sputtered from a $Co_{70}Fe_{30}$ target at a source power of 25 W, using a gas flow of 10 sccm Ar and a working pressure of $p_w = 2 \times 10^{-3}$ mbar. The Ta buffer layer, yielding an improved growth of the polycrystalline MnN, was deposited with the same parameters, however at an increased source power of 50 W. In order to protect the sample from oxidation and other damaging processes in air a thin capping layer of Ta_2O_5 was deposited on the completed stack. Therefor, a small amount of oxygen was lead into the sputter chamber, giving rise to a reactive sputter process in a gas atmosphere of 80 % Ar to 20 % O_2 with a constant gas flow of 10 sccm at $p_w = 2 \times 10^{-3}$ mbar. The corresponding sputter rates were determined with a quartz sensor installed inside the sputter chamber previous to the deposition runs to calculate desired sputter times and resulting film thicknesses.

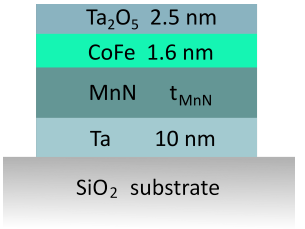

Figure 3.4: Schematic setup for all samples investigated in the high-temperature annealing study.

After preparation, the samples were post-annealed in a vacuum furnace with pressure below 5×10^{-6} mbar and cooled down in a magnetic field of $H_{fc} = 6.5$ kOe parallel to the film plane to activate exchange bias. Subsequent post-annealing for 15 min at increasing annealing temperatures was performed to obtain temperature dependent results for the below presented annealing series. The furnace is equipped with a copper heating block that provides annealing temperatures of up to $T_A = 550°$ C. The annealing process is not only necessary for the generation of exchange bias but can also influence the crystallinity of a sample, especially at high temperatures.

3.2.2 Results

Magnetic characterization

Magnetic characterization of the samples was performed using the longitudinal magneto-optical Kerr effect (MOKE) at room temperature. Detecting MOKE measurements after activation of exchange bias yields shifted hysteresis loops that provide information about the exchange bias as well as the coercivity of the corresponding sample. Fig. 3.5 shows an exemplary hysteresis loop detected for a sample with $t_{\mathrm{MnN}} = 48\,\mathrm{nm}$ after high-temperature annealing at $T_{\mathrm{A}} = 500\,^{\circ}\mathrm{C}$. Very high exchange bias of $H_{\mathrm{eb}} = 2600\,\mathrm{Oe}$, indicated in Fig. 3.5, accompanied by a reasonably small coercive field of $H_{\mathrm{c}} = 630\,\mathrm{Oe}$ can be observed. This gives rise to a ratio of $H_{\mathrm{eb}}/H_{\mathrm{c}} \approx 4$. For possible integration into spintronic devices like GMR valves it is crucial for the ratio $H_{\mathrm{eb}}/H_{\mathrm{c}}$ to be larger than unity, which is easily fulfilled for the presented sample. Furthermore, the CoFe layer is almost saturated at zero field. Using the saturation magnetization of $M_{\mathrm{CoFe}} \approx 1700\ \mathrm{emu/cm^3}$ for the CoFe film [75], the corresponding maximum effective interfacial exchange energy

$$J_{\mathrm{eff}} = t_{\mathrm{CoFe}} \cdot M_{\mathrm{CoFe}} \cdot \mu_0 H_{\mathrm{eb}} \approx 0.76\,\mathrm{erg/cm^2} \tag{3.10}$$

can be estimated.

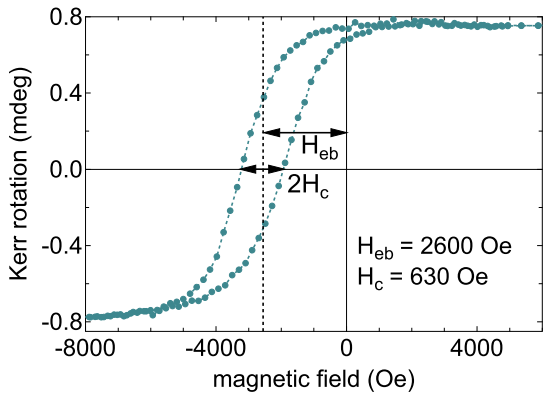

Figure 3.5: Hysteresis loop detected parallel to the field cooling direction for a sample with $t_{\mathrm{CoFe}} = 1.6\,\mathrm{nm}$ and $t_{\mathrm{MnN}} = 48\,\mathrm{nm}$ after annealing at $T_{\mathrm{A}} = 500\,^{\circ}\mathrm{C}$, measured at room temperature. The exchange bias field is marked with a dashed line.

In order to get information about the influence of the MnN thickness on the thermal stability and temperature dependence of exchange bias, a detailed annealing series was performed for samples with $t_{\mathrm{MnN}} = 32, 36, 42$ and 48 nm. Therefor, the samples were successively annealed up to $T_{\mathrm{A}} = 550°$ C for 15 min and MOKE measurements were taken in between the single annealing steps, at room temperature, to determine the corresponding exchange bias and coercive fields. An estimated error of ±50 Oe is added to the extracted field values to account for possible uncertainties arising from the setup. As the temperature dependence of exchange bias systems with $t_{\mathrm{MnN}} = 32$ nm has been investigated before (cf. Fig. 3.3), this sample functions as a reference to verify the quality of the prepared sample set.

In Fig. 3.6 a), the resulting dependence of exchange bias on the annealing temperature is depicted for the different MnN thicknesses. Starting at annealing temperatures around $T_{\mathrm{A}} = 300°$ C, all samples show quite similar exchange bias values of $H_{\mathrm{eb}} \approx 1400$ Oe. While the two samples with the thinner MnN layers exhibit a plateau with rather constant values for increasing annealing temperatures, the exchange bias slightly decreases and reaches a local minimum when thicker layers of MnN are used. However, when reaching high annealing temperatures of $T_{\mathrm{A}} \geq 400°$ C, which is higher than the Néel temperature of MnN, it gets obvious that the MnN thickness

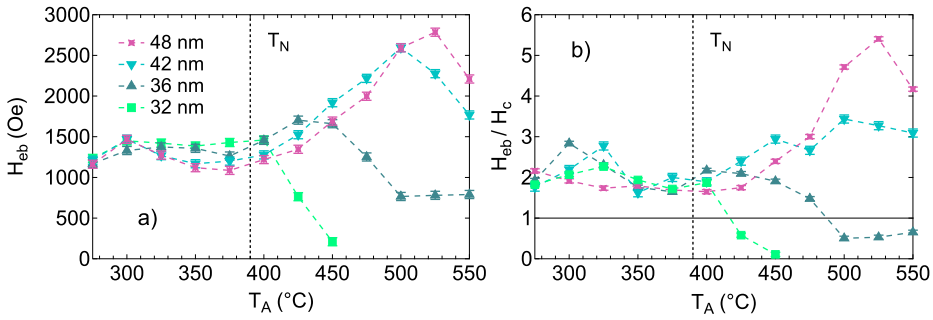

Figure 3.6: Dependence of a) Exchange bias field and b) Ratio $H_{\mathrm{eb}}/H_{\mathrm{c}}$ on the annealing temperature T_{A} determined for samples with different MnN thicknesses. The crossing of the Néel temperature of MnN is indicated with dashed lines. An estimated error of ±50 Oe was added to the extracted field values.

has a strong influence on the system's thermal stability. With a thickness of $t_{\mathrm{MnN}} = 32\,\mathrm{nm}$, the exchange bias is stable up to $T_{\mathrm{A}} = 400\,^{\circ}\mathrm{C}$ before it decreases, perfectly agreeing with our previous studies [31]. For samples with thicker films of 36 and 42 nm MnN, the thermal stability is increased up to $T_{\mathrm{A}} = 450^{\circ}$ and 500° C, respectively. When using 48 nm MnN, exchange bias values of $H_{\mathrm{eb}} > 2000\,\mathrm{Oe}$ are still observable after annealing at the highest possible temperature of $T_{\mathrm{A}} = 550^{\circ}$ C. Thus, it can be concluded that thicker MnN layers yield increased thermal stability.

The giant increase of exchange bias after high-temperature annealing is especially observable for the samples with $t_{\mathrm{MnN}} = 42$ and 48 nm. Both yield exchange bias values of more than 2500 Oe with the maximum of 2785 Oe reached after annealing at $T_{\mathrm{A}} = 525\,^{\circ}\mathrm{C}$ for the sample with 48 nm MnN. In our previous work [31], we found that the thermal stability of MnN crucially depends on the nitrogen content in the MnN lattice (cf. Fig. 3.3). Samples that were prepared with a higher amount of nitrogen (55 %) during the reactive sputter process showed an increase of exchange bias after annealing at $T_{\mathrm{A}} = 400^{\circ}$ C, similarly to the behavior observed for the very thick MnN films in this study. However, with a higher nitrogen content in the lattice, this was even visible for samples with MnN thicknesses of about 30 nm that are not thermally stable at such high temperatures when prepared with the usual amount of nitrogen (50 %) during reactive sputtering. On the contrary, as thicker MnN films have a larger nitrogen reservoir by default, the huge increase of exchange bias after annealing at high temperatures is observable here for the usual preparation parameters. These findings lead to the conclusion that the effect of large exchange bias after high-temperature annealing is related to the amount of nitrogen in the MnN film.

Additionally, in this study the highest ratio of $H_{\mathrm{eb}}/H_{\mathrm{c}} = 5.4$ is found for the same parameters as the highest exchange bias, namely for the sample with 48 nm MnN after annealing at $T_{\mathrm{A}} = 525\,^{\circ}\mathrm{C}$. The corresponding temperature dependence is displayed in Fig. 3.6 b) in detail. It can be seen that the critical value of one, which is marked by a solid line, is exceeded by all samples throughout most of the investigated temperature window. Only for the samples with 32 and 36 nm MnN smaller values are observed at annealing

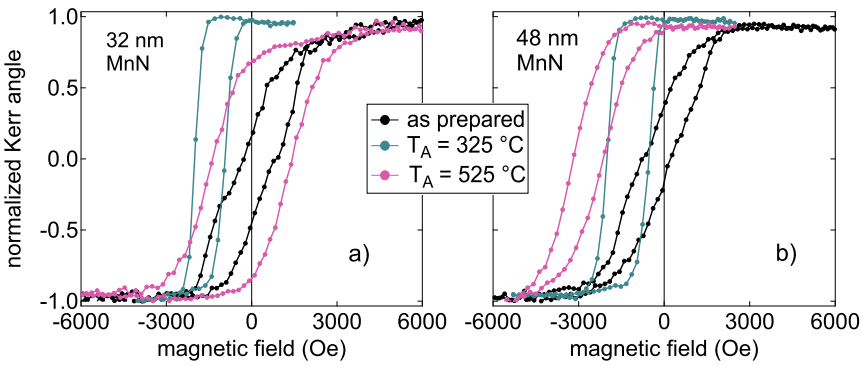

Figure 3.7: Hysteresis loops of exchange bias systems with a) $t_{\mathrm{MnN}} = 32$ and b) 48 nm detected via MOKE measurements at room temperature. Loops before and after annealing at $T_{\mathrm{A}} = 325\,^{\circ}\mathrm{C}$ and $T_{\mathrm{A}} = 525\,^{\circ}\mathrm{C}$, respectively, are shown. The data was normalized for the sake of better comparability.

temperatures higher than where the corresponding exchange bias maximum was found.

Fig. 3.7 shows some exemplary hysteresis loops for the samples with the thinnest (32 nm) and the thickest (48 nm) MnN layer. For both thicknesses, MOKE results before annealing and after annealing at $T_{\mathrm{A}} = 325^{\circ}\,\mathrm{C}$ and $T_{\mathrm{A}} = 525^{\circ}\,\mathrm{C}$, respectively, are displayed. In the as prepared state, the detected hysteresis loop is centered around zero and looks quite similar for both samples. However, for the thinner sample a higher coercivity, indicating the presence of exchange coupling even before field cooling, can be observed. After annealing at $T_{\mathrm{A}} = 325^{\circ}\,\mathrm{C}$, a clear hysteresis shift is visible for both thicknesses. The exchange bias is slightly higher and the coercivity smaller for 32 nm MnN. No exchange bias can be observed for the thinner sample after high-temperature annealing at $T_{\mathrm{A}} = 325^{\circ}\,\mathrm{C}$. Additionally, the coercivity has strongly increased. For the thicker sample though, the hysteresis is shifted to highly negative field values and shows even smaller coercivity compared to the previous loops.

An additional parameter that yields further information about the thermal stability of any given exchange bias system is its blocking temperature, i.e. the corresponding blocking temperature distribution in polycrystalline

films with varying grain size [69]. In order to investigate the influence of high-temperature annealing on the blocking temperature distribution of the MnN/ CoFe system, reversed field cooling experiments [76] were performed on samples with $t_{\mathrm{MnN}} = 42, 48\,\mathrm{nm}$. The samples were initially field-cooled from $T_{\mathrm{set}} = 525°\,\mathrm{C}$ and $T_{\mathrm{set}} = 550°\,\mathrm{C}$ for thicknesses of 42 nm MnN and 48 nm MnN, respectively, and their hysteresis loops were measured to detect $H_{\mathrm{eb}}(\mathrm{RT})$. After that, the stacks were successively field-cooled in a reversed field from $T_{\mathrm{rev}} = 50, 75, 100, ..., 525\,(, 550)°\,\mathrm{C}$. In Fig. 3.8 a), the dependence of exchange bias on the reversal temperature is shown. The zero crossing of this curve marks the median blocking temperature $< T_{\mathrm{B}} >$ of the antiferromagnetic grains that are still blocked at room temperature. For both MnN thicknesses

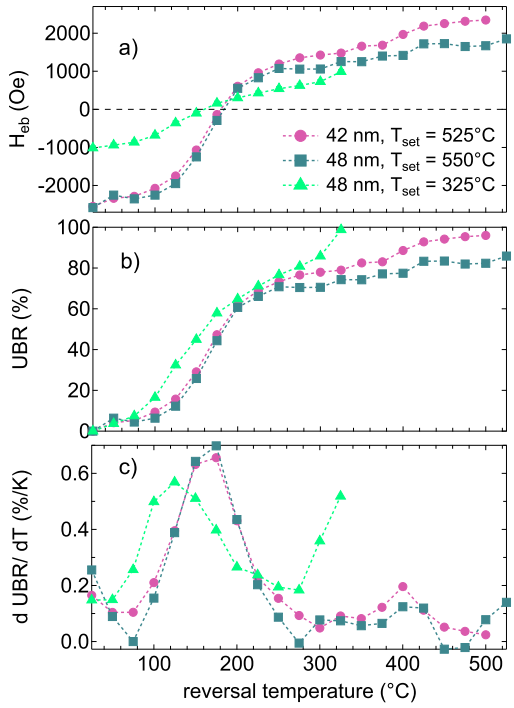

Figure 3.8: Results of the reversed field cooling experiments performed on exchange bias systems with $t_{\mathrm{MnN}} = 42$ and 48 nm and $t_{\mathrm{CoFe}} = 1.6\,\mathrm{nm}$: a) Exchange bias, b) Unblocked ratio UBR and c) Derivative of the unblocked ratio in dependence on the temperature of reversed field cooling. The data set for $t_{\mathrm{MnN}} = 48\,\mathrm{nm}$ with $T_{\mathrm{set}} = 325°\,\mathrm{C}$ is included for the sake of comparability from a previous study [31]. The error bars are smaller than the markers.

it lies around 180° C. The unblocked ratio (UBR), i.e. the area fraction of unblocked grains, is obtained via

$$\mathrm{UBR}(T_{\mathrm{rev}}) = 100\% \cdot \frac{H_{\mathrm{eb}}(\mathrm{RT}) - H_{\mathrm{eb}}(T_{\mathrm{rev}})}{2H_{\mathrm{eb}}(\mathrm{RT})}, \tag{3.11}$$

representing the cumulative distribution function of the blocking temperature, presented in Fig. 3.8 b). By taking the derivative of this function, the blocking temperature distribution can be obtained. It is shown in Fig. 3.8 c) and has a maximum around 170° C.

In the course of our previous investigations [31], field cooling experiments on similar samples with $t_{\mathrm{MnN}} = 48\,\mathrm{nm}$ were performed. However, then, they were initially field-cooled from a lower temperature $T_{\mathrm{set}} = 325°\,\mathrm{C}$. The resulting values are included in Figure 3 for comparability, yielding a median $< T_{\mathrm{B}} >$ of 160° C with a maximum of the corresponding blocking temperature distribution around 125 °C. Comparing this to our new results, the high-temperature annealing has a positive influence on the thermal stability of the MnN/ CoFe system and seems to increase either the grain volume or the magnetocrystalline anisotropy energy.

Structural characterization

In order to identify what causes the giant increase of exchange bias after high-temperature annealing, possible changes in the crystal structure were investigated via x-ray diffraction measurements that were performed in between the single annealing steps for the sample with 42 nm MnN. In Fig. 3.9, the corresponding diffraction patterns directly after preparation and after annealing at $T_{\mathrm{A}} = 325°\,\mathrm{C}$ and $T_{\mathrm{A}} = 525°\,\mathrm{C}$ are shown. The measurements confirm a polycrystalline, columnar growth of MnN in (001) direction.

The lattice constant of MnN directly after preparation is $c = 4.264\,\text{Å}$, which is slightly larger than the bulk values reported in literature [36]. After annealing, the (002) peak of MnN narrows and increases in intensity, indicating growth of the crystal grains and a relaxation of strain. Both can have a beneficial

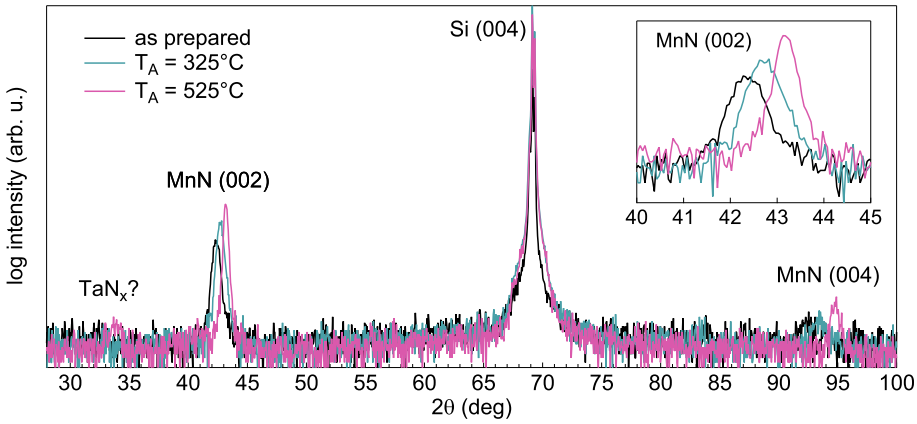

Figure 3.9: X-ray diffraction spectrum of an exchange bias stack with 42 nm MnN before and after annealing at $T_A = 325\,°C$ and $T_A = 525\,°C$, respectively. The inset shows a zoom-in around the angular range of the (002) peak of MnN.

influence on the exchange bias. Larger crystal grains are also in line with the observed enhancement of the blocking temperature [69].

Furthermore, after annealing, the (002) and (004) peaks of MnN are shifted towards higher angles, indicating smaller lattice constants. This is related to nitrogen diffusion that occurs during annealing. With decreasing nitrogen content in the MnN film, the lattice constant decreases. Fig. 3.10 displays the detailed evolution of the lattice constant c in dependence on the annealing temperature, determined from

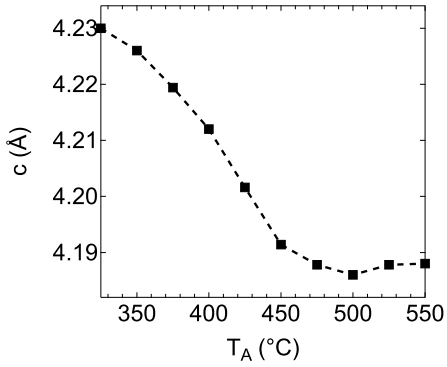

Figure 3.10: Dependence of the lattice constant c of MnN on the annealing temperature for a sample with $t_{MnN} = 42\,nm$. Values were determined via the MnN (002) peak.

the MnN (002) peak's position in the corresponding x-ray diffraction scans. Starting at $c = 4.23\,\text{Å}$ after annealing at $T_\text{A} = 325°\,\text{C}$, it decreases monotonously with increasing annealing temperature up to $T_\text{A} = 475°\,\text{C}$ where it saturates around $c = 4.188\,\text{Å}$, close to the value that was determined by Suzuki et al. [36]. After annealing at $T_\text{A} = 525°\,\text{C}$, an additional peak around 34° arises that is not related to any phase of Mn−N. Possibly, it is attributed to the formation of TaN_x in the Ta buffer layer caused by the nitrogen diffusion.

Auger electron spectroscopy

To verify the temperature dependent nitrogen diffusion that is suggested by the x-ray diffraction results, Auger electron spectroscopy (AES) depth profiling [77] was performed on a corresponding Ta/ MnN/ CoFe stack with $t_\text{MnN} = 48\,\text{nm}$. Therefor, a scanning Auger microscope PHI660 was used. The samples were continuously rotated during sputtering with a 500 eV Ar^+ ion beam to achieve optimum depth resolution. The measured Auger intensities are defined as peak to peak heights of the differential spectrum of the

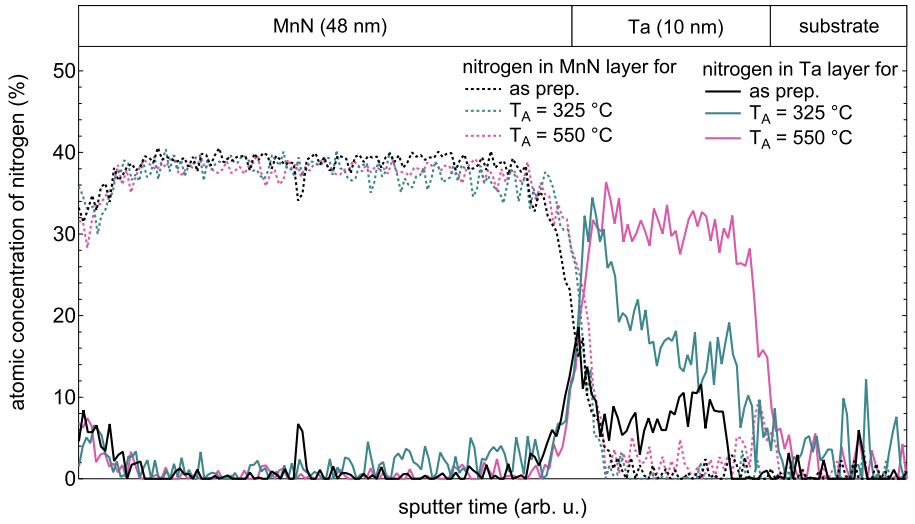

Figure 3.11: Depth profile displaying the nitrogen concentration in a stack with $t_\text{MnN} = 48\,\text{nm}$ detected with Auger electron spectroscopy directly after preparation and after annealing at $T_\text{A} = 325$ and 550° C.

different components. Target factor analysis [78] was used for separating the different chemical states of nitrogen in TaN_x and MnN_x.

Measurements were taken in the as prepared state and after annealing at $T_A = 325$ and 550° C, respectively. Fig. 3.11 shows the resulting depth profile of the nitrogen concentration detected in the Mn and the Ta buffer layer for those three temperature settings. Obviously, the nitrogen concentration in the Ta layer increases with each annealing process. Notably, even in the as prepared state a significant amount of nitrogen can be found in the Ta layer. After annealing at $T_A = 550°$ C, an almost homogeneous concentration of nitrogen is detected in the whole Ta film. It strikes that the nitrogen concentration inside the Mn layer does not decrease with increasing nitrogen concentration in the Ta layer. A strong preferential sputtering of nitrogen is known for other transition-metal nitrides [79], which can change the apparent composition of the nitride film. Our results suggest that this effect is also present for Mn−N and that the same sputter equilibrium ratio of Mn and N is reached for the sample in the as prepared state as well as after annealing. This can mask the expected reduction of the nitrogen concentration in the Mn−N if the nitrogen concentration in the Ta increases. Nonetheless, the depth profiles verify strong nitrogen diffusion caused by the high-temperature annealing.

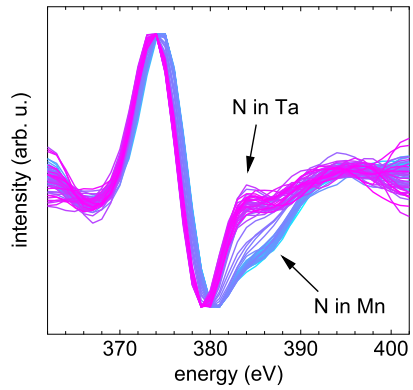

Figure 3.12: Normalized KLL-Auger transition of nitrogen in the differential spectrum for different depths after annealing at $T_A = 550°$ C. The color transition from blue to pink corresponds to increasing depth.

In Fig. 3.12, the evolution of the Auger peak of nitrogen for different depths is displayed after annealing the sample at $T_A = 550°$ C. The color change

from blue to pink relates to increasing sputter time/ depth, i.e. the transition from Mn to Ta. A chemical shift of the nitrogen Auger peak is clearly visible. These findings coincide with the appearance of the additional peak in the XRD scan that might be related to TaN_x after annealing at high temperatures as well as the decrease of the lattice constant c with increasing annealing temperature. However, this strong diffusion of nitrogen does not seem to worsen but significantly increase the exchange bias.

Polarized neutron reflectometry

In a collaboration with P. Quarterman et al. [80], the nitrogen diffusion inside exchange bias stacks with MnN was further investigated via polarized neutron reflectometry (PNR). Therefor, samples with a similar setup as used for the high-temperature annealing studies were prepared. Only the ferromagnetic film was changed from CoFe to a thicker layer of CoFeB (7 nm), which, however, should not affect the nitrogen diffusion from MnN into Ta that was observed in the Auger depth profiling measurements distinctly. Increasing the ferromagnet's thickness for PNR measurements is beneficial as it allows for magnetic effects to be more prominently observable. The measurements were performed using the Polarized Beam Reflectometer instrument at the National Institute of Standards and Technology Center for Neutron Research. Further information about PNR or details concerning the measurement geometry can be found in [80] and [81], respectively.

PNR is especially sensitive to nitrogen movement from MnN into Ta as the scattering length density (SLD) of Mn is strongly negative whereas the SLD for nitrogen is strongly positive. In contrast to AES, it is also possible to detect changes to the nitrogen concentration in the MnN and not only the Ta layer. Two samples with different thicknesses of MnN (30 nm and 48 nm) were investigated in the as prepared state and after annealing at $T_A = 325°$ C and $T_A = 525°$ C.

Fig. 3.13 displays the corresponding PNR results in terms of a nuclear and a magnetic SLD depth profile for a sample with 30 nm MnN (a) and 48 nm MnN (b). The nuclear depth profile can be interpreted as a measure of

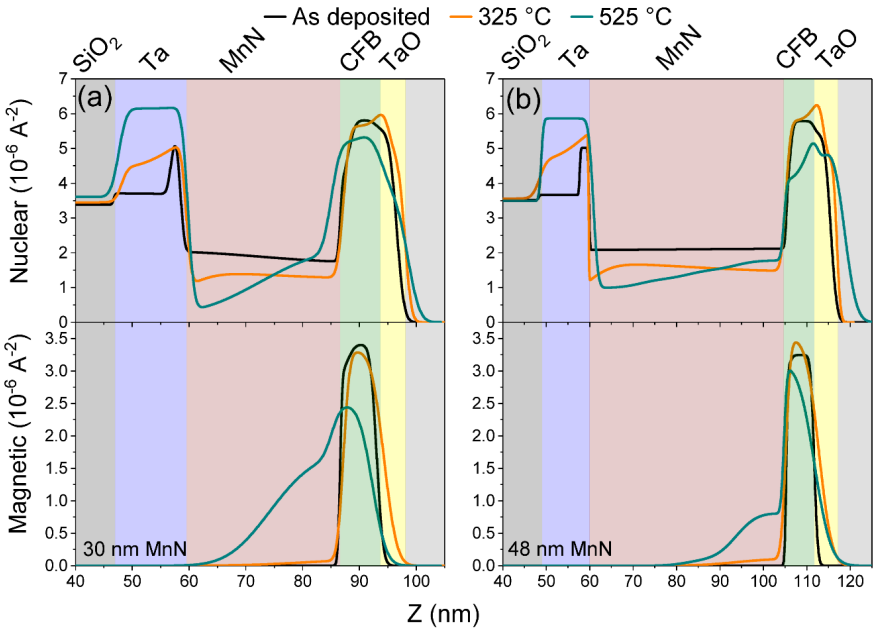

Figure 3.13: Nuclear (top) and magnetic (bottom) scattering length density profiles for exchange bias samples with 7 nm CoFeB and (a) 30 nm and (b) 48 nm of MnN before and after annealing at $T_A = 325$ and 525° C, respectively. The layers are denoted by their corresponding nominal thicknesses and the distance Z is referenced such that the Si/ SiO_2 interface is positioned at 0 nm [80].

nitrogen content in the corresponding layer [80]. Hence, it is easily visible that the PNR results match well with the AES profiles that were previously detected for a sample with 48 nm MnN. A significant amount of nitrogen can be found at the Ta side of the Ta/ MnN interface in the as prepared state for both MnN thicknesses. After the first annealing step, the nitrogen content in the Ta layer strongly increases, resulting in the formation of a nitrogen-poor zone in the MnN close to the Ta interface. Annealing at $T_A = 525°$ C yields the complete and homogeneous saturation of the Ta buffer layer with nitrogen, inducing a significant nitrogen deficiency in the MnN layer.

Comparing the results of the two samples, it gets clear that the decrease of nitrogen concentration in proximity to the Ta buffer layer is way more pronounced when using a 30 nm MnN film. These findings combined with

the results of the annealing series, where samples with thicker MnN showed more stable exchange bias after high-temperature annealing, confirm that the nitrogen content in the MnN layer is the crucial factor in terms of thermal stability. To saturate the buffer layer of Ta with nitrogen during annealing, thinner MnN films become nitrogen deficient quicker (at lower temperatures) than thick films with a larger nitrogen reservoir. Furthermore, it is observable that a significant amount of nitrogen can be detected in the ferromagnetic CoFeB layer, even before annealing. It is thus possible that antiferromagnetic Fe or Co nitrides form during the annealing processes, affecting the exchange bias. As more nitrogen vacancies are generated in the 30 nm film during annealing, interdiffusion at the MnN/ CoFeB interface is more prominent in this sample. The magnetic depth profiles underline this observation. After annealing at $T_A = 525°$ C, magnetic material sweeps far into the MnN layer as Fe and Co atoms mix with the Mn atoms. This is again much stronger visible for the sample with 30 nm than for the thicker one.

3.3 Role of the buffer layer in Ta/MnN/CoFeB stacks for maximizing exchange bias

As discussed in the previous section, it has been shown via PNR [80] and AES depth profiling [59] studies of Ta/ MnN/ CoFeB stacks that nitrogen diffusion during annealing plays a significant role in determining the magnitude of exchange bias and the system's thermal stability. Whereas the influence of the MnN thickness was investigated according to these terms in the previous study, the focus is now laid on the role of the Ta buffer layer.

Both the PNR and AES measurements revealed that nitrogen diffuses from the MnN into the Ta layer during the annealing process. After annealing at high temperatures of $T_A > 500^\circ$ C, the Ta layer is fully saturated with nitrogen. It was proposed that, in terms of better thermal stability, using a thinner Ta buffer layer could be beneficial [80]. The thinner the Ta, the smaller the nitrogen drain and accordingly less nitrogen needs to diffuse from the MnN to the Ta layer for the latter to be saturated. Thus, to learn more about the consequences of nitrogen diffusion, the influence of the Ta thickness on the exchange bias and the thermal stability of Ta/ MnN/ CoFeB systems is investigated in the course of this study. Furthermore, the effects of introducing an additional TaN_x layer, acting as a diffusion barrier, between MnN and Ta is tested.

3.3.1 Sample preparation

For this buffer layer study, two different sets of samples were prepared. In the first set, the Ta buffer layer thickness was varied between $1 - 15$ nm resulting in the setup illustrated in Fig. 3.14 a). For the second set of samples, an additional TaN_x layer was introduced while the Ta thickness was kept constant at 3 or 10 nm, yielding the setup depicted in Fig. 3.14 b) and Fig. 3.14 c), respectively. The thickness of TaN_x was varied from $0.5 - 3$ nm. Both sample sets were prepared via (reactive) DC magnetron sputtering following the exact same procedure as presented in Chapter 3.2.1. However, in this study, $Co_{40}Fe_{40}B_{20}$ substitutes CoFe as the ferromagnetic layer. It was prepared with the exact same sputter parameters. The intermediate TaN_x layer was

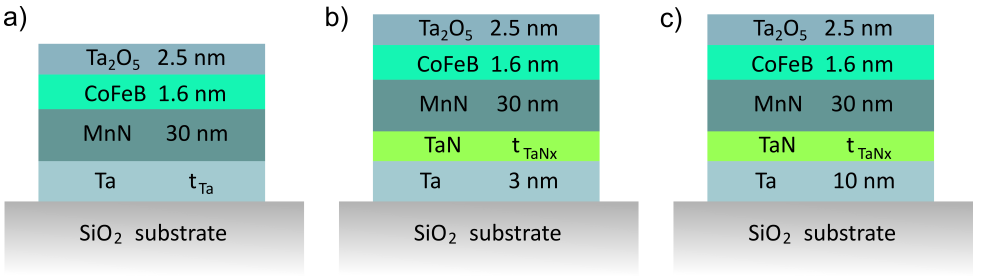

Figure 3.14: Schematic setup of the samples used for the Ta buffer layer investigation in the standard configuration a) or with an additional TaN_x interlayer, b) and c).

prepared via reactive sputtering from an elemental Ta target. A gas ratio of 78 % Ar to 22 % N_2 was used, yielding the best crystallographic results throughout a partial pressure series from 14 % to 22 % nitrogen. To activate exchange bias, the samples were annealed in a vacuum furnace and cooled down in a magnetic field as described in Chapter 3.2.1.

3.3.2 Results of the Ta thickness variation

To investigate how the Ta buffer layer thickness influences the thermal stability of Ta/ MnN/ CoFeB exchange bias systems, annealing series with temperatures ranging from $T_A = 100°$ C to $T_A = 550°$ C were performed. The samples were successively annealed at increasing temperature and MOKE measurements were taken in between the single steps. Fig. 3.15 a) displays the dependence of exchange bias on the annealing temperature for samples with Ta thicknesses varying between 1 nm and 15 nm. Since CoFeB was chosen as a ferromagnetic layer instead of CoFe, the total exchange bias values are somewhat smaller and the optimized sample with the commonly used 10 nm Ta slightly deviates from the results observed in our previous studies [31, 33, 59].

Notably, independent of the Ta thickness, all samples follow a similar behavior at low annealing temperatures. Starting from exchange bias values of $H_{eb} = 500$ Oe, a minimum is reached around $T_A = 250°$ C. This temperature range is identified as the first of three regimes, indicated by background coloring in Fig. 3.15. At higher annealing temperatures, the exchange bias

rises and reaches a plateau. In this second regime, the Ta thickness obviously has a strong influence: the thicker the Ta layer, the higher the exchange bias. Thicker Ta layers yield stronger diffusion from MnN into the Ta during annealing. However, up until temperatures around $T_A = 450°\,C$, this process does not lower the exchange bias, as can be seen from the results for the sample with 15 nm Ta. Only when reaching the third regime with high annealing temperatures of $T_A > 450°\,C$, nitrogen diffusion becomes a crucial factor. The sample with the thickest Ta buffer layer loses its exchange bias whereas the other samples do not show decreasing values yet.

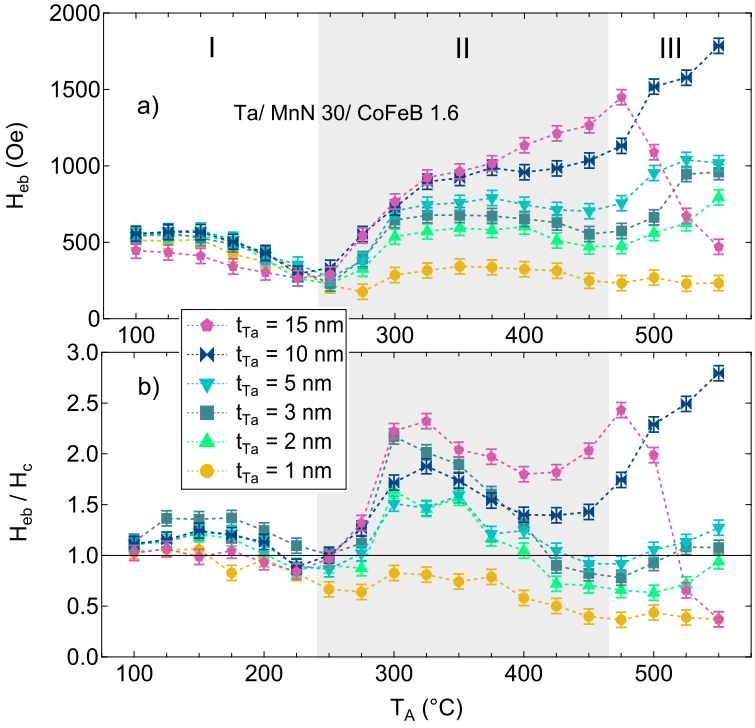

Figure 3.15: a) Exchange bias H_{eb} and b) Ratio H_{eb}/H_c as a function of the annealing temperature T_A for Ta/ MnN/ CoFeB exchange bias systems with varying Ta thickness. Measurements were taken after each annealing step at room temperature. I, II and III mark three distinct annealing temperature regimes. An estimated error of ±50 Oe was added to the extracted magnetic field values.

In general, all samples, except for the thinnest one, show a very similar dependence on the annealing temperature: After reaching the plateau in regime II, a local minimum can be observed before the exchange bias rises again in regime III. This minimum and the corresponding rise are located at higher annealing temperatures for samples with thinner Ta layers. The minimum of exchange bias marking the transition from temperature range I to II has also been observed in all our previous studies on MnN exchange bias systems [31, 33, 59]. The dip is not accompanied by any structural transitions and is not observed in a second sequence of annealing once the exchange bias has been reset with a zero-field annealing [31]. This behavior is quite unique and up to now we can only speculate about its origin. Possibly, a magnetic ordering transition like a spin reorientation from easy axis to easy plane [35, 36] is happening at annealing temperatures around $T_\mathrm{A} = 250^\circ$ C.

Fig. 3.15 b) shows the ratio of the exchange bias and the corresponding coercive field $H_\mathrm{eb}/H_\mathrm{c}$ as a function of the annealing temperature. Again, $H_\mathrm{eb}/H_\mathrm{c} > 1$ needs to be fulfilled for any exchange bias system to be integratable into spintronic devices. Here, this is reached for all samples with Ta thicknesses higher than 1 nm. However, for $T_\mathrm{A} > 400^\circ$ C the ratio of the 2 nm Ta sample decreases to values smaller than one, followed by samples with 3 and 5 nm Ta layers, before a weak increase is observable again after annealing at the highest temperatures.

Next, the influence of the Ta thickness on the crystallographic properties of MnN was investigated via x-ray diffraction. Fig. 3.16 shows diffraction patterns of the Ta/ MnN/ CoFeB system with a 10 nm Ta buffer layer directly after preparation, after annealing at $T_\mathrm{A} = 325^\circ$ C (regime II), and after annealing at the highest possible temperature of $T_\mathrm{A} = 550^\circ$ C (regime III). The measurements are consistent with our previous findings of a polycrystalline, columnar growth of MnN in (001) direction [31, 73]. The lattice constant of MnN directly after preparation is $c = 4.282$ Å, which is slightly larger than the bulk values reported in literature [36]. The inset shows the corresponding rocking curve of MnN's (002) peak, which yields a FWHM of 5.92° for the as prepared sample. This suggests a rather uniform growth of the crystallites in the c-direction. After annealing, the MnN peaks are slightly shifted to higher

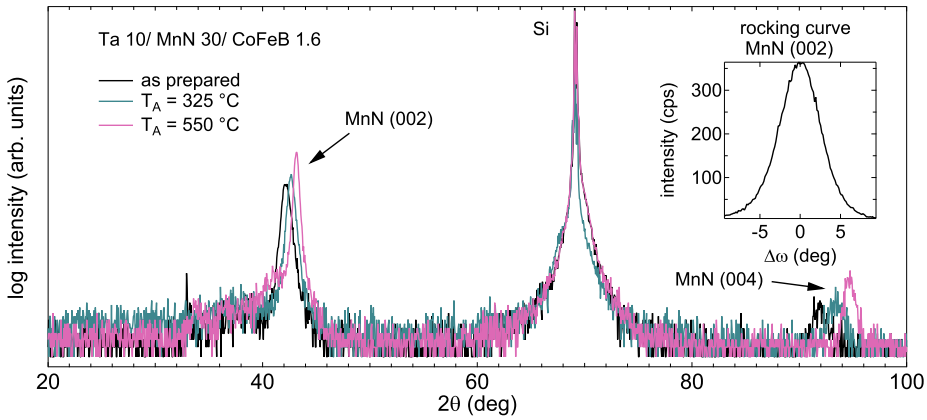

Figure 3.16: X-ray diffraction pattern of a Ta/ MnN/ CoFeB sample with a 10 nm Ta buffer layer as prepared and after annealing at $T_A = 325°$ C, and $T_A = 550°$ C. The inset shows the rocking curve of MnN's (002) peak after preparation.

angles, indicating a smaller lattice parameter of $c = 4.189$ Å after annealing at $T_A = 550°$ C. This can be attributed to the generation of nitrogen vacancies as interdiffusion occurs during the annealing process, leading to a decrease of MnN's lattice constants [31].

In Fig. 3.17 a) and b), diffraction scans around the angular range of MnN's (002) peak are shown for all Ta thicknesses. Directly after preparation (Fig. 3.17 a)), MnN yields good crystallinity in all samples, except for the one with 1 nm Ta. The reduced crystallinity is directly connected to the low exchange bias values observed for this sample. Decreased crystallinity yields smaller grains, thus the anisotropy energy per grain is also decreased. This shifts the blocking temperature distribution such that lower exchange bias is observed at a given measurement temperature [19, 69].

After annealing at $T_A = 550°$ C (Fig. 3.17 b)), significant changes to the crystal structure are visible. The MnN's (002) peak narrows, indicating vertical crystallite growth or relaxation of microstrain. In our previous study [31], we concluded that the crystallites are columnar and their height corresponds to the film thickness; thus, the narrowing here can be assigned to a relaxation

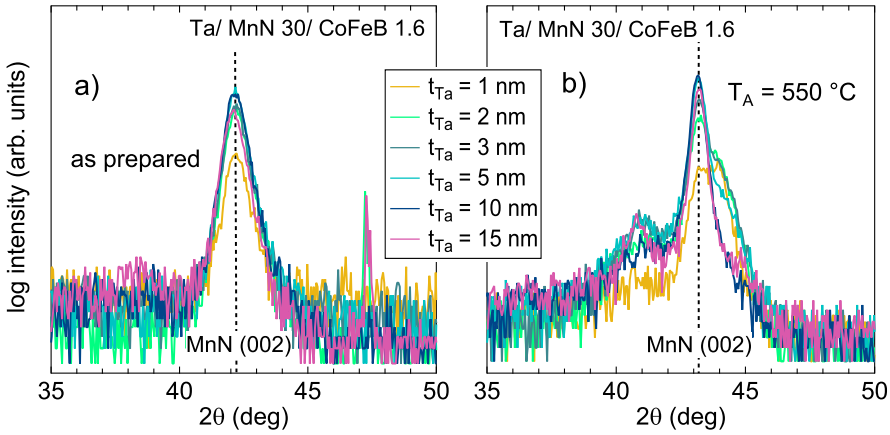

Figure 3.17: Diffraction scans around the angular range of the (002) peak of MnN for Ta/ MnN/ CoFeB samples with different Ta thicknesses detected a) Directly after preparation and b) After annealing at $T_\mathrm{A} = 550°$ C.

of microstrain. However, in all samples with $t_\mathrm{Ta} < 10$ nm an additional peak arises in the right shoulder of the MnN (002) peak. The fact that this peak is not observable for all samples suggests that it is connected to a structural transition that only occurs if the Ta layer is thin enough, i.e. enough nitrogen is left in the MnN layer. An additional peak emerges around 41° in all samples. Possibly, those peaks result from an emerging phase transition of the MnN to a less nitrogen-rich composition. Alternatively, they could be related to the formation of a crystalline TaN_x interlayer between Ta and MnN, similarly to the additional peak observed for thick MnN after high-temperature annealing in the previous study (cf. Fig 3.9). The origin of those unidentified peaks will be discussed in more detail further below.

Concluding the results of the Ta thickness variation, a clear dependence of the thermal stability of Ta/ MnN/ CoFeB systems on the buffer layer thickness was found. With increasing Ta thickness, higher exchange bias is generated after a transition temperature around $T_\mathrm{A} = 250°$ C is crossed, which is compatible with the reduced crystallinity that is observed for samples with thinner Ta. However, at the same time, the thermal stability decreases when thicker layers of Ta are used, as could be seen for the 15 nm Ta sample. This confirms the

hypothesis that more nitrogen is drawn from the MnN when using thicker Ta layers. All in all, the standard value of 10 nm Ta that was usually used in our previous studies indeed seems to be the optimum value when high exchange bias is needed. Yet, if minimizing the stack's thickness is desired, for example for integration of Ta/ MnN/ CoFeB systems into spintronic devices, samples with 5 nm Ta also yield conveniently high exchange bias accompanied by good thermal stability.

3.3.3 Results of introducing a TaN diffusion barrier

To further understand the role of the buffer layer in the diffusion processes occurring in the Ta/ MnN/ CoFeB exchange bias system, a second set of samples with an additional TaN_x interlayer was investigated. Fig. 3.18 a) displays the dependence of exchange bias on the annealing temperature for samples with $t_{Ta} = 3$ nm and varying TaN_x thickness. Again, the results can be separated into three different temperature regimes, indicated in Fig. 3.18. For low annealing temperatures, all samples show exchange bias values around $H_{eb} = 500$ Oe before reaching a minimum around $T_A = 250°$ C. This is similar to the behavior observed for the Ta thickness series discussed above and yet another hint that a magnetic ordering transition is happening between temperature regimes I and II.

At higher annealing temperatures, the influence of the TaN_x interlayer gets more significant. Whereas the samples with 0.5 nm and 1 nm TaN_x show increasing exchange bias values and reach a plateau, a thicker interlayer of TaN_x causes the absence of a local maximum in regime II. The results observed for even higher annealing temperatures need to be interpreted very carefully. Diffusion processes and structural transitions are happening simultaneously, making it hard to disentangle their effect on the exchange bias.

All samples show increasing exchange bias for $T_A > 450°$ C. However, the two samples with thinner TaN_x exhibit a distinct maximum, whereas the samples with thicker TaN_x only show a small increase. As can be seen in Fig. 3.18 b), the requirement for the ratio H_{eb}/H_c to be larger than unity is

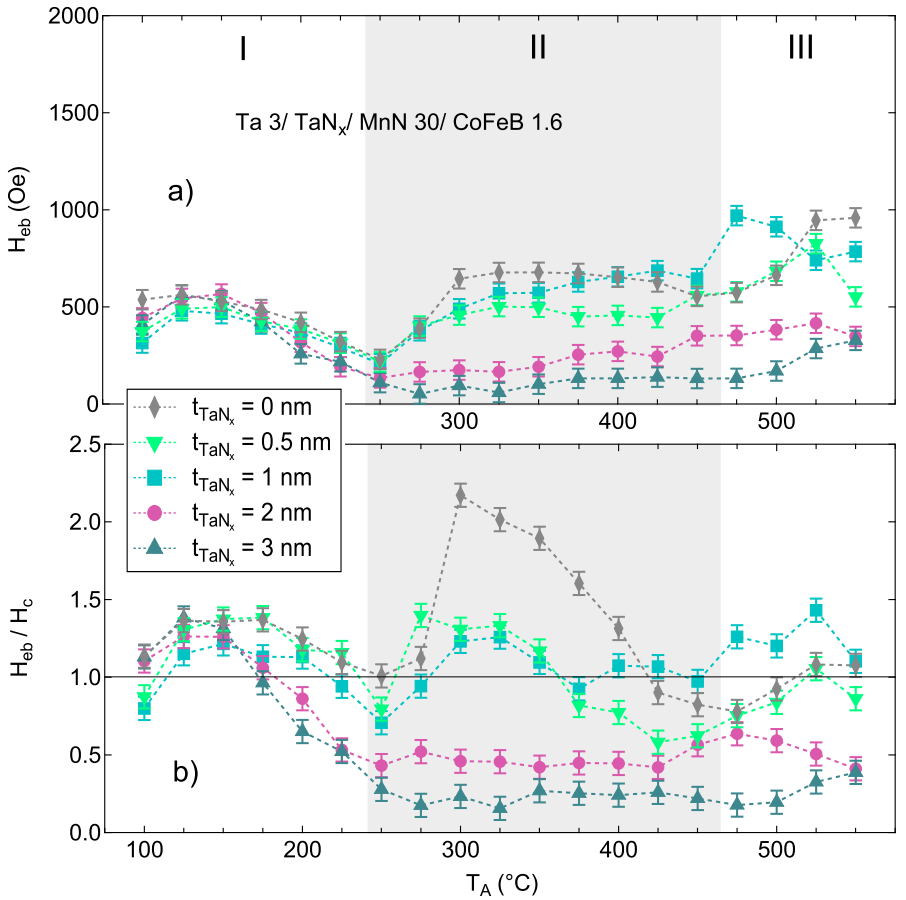

Figure 3.18: a) Exchange bias H_{eb} and b) Ratio $H_{\mathrm{eb}}/H_{\mathrm{c}}$ as a function of the annealing temperature T_{A} for Ta/ MnN/ CoFeB exchange bias samples with a 3 nm buffer layer of Ta and an additional $\mathrm{TaN_x}$ interlayer of varying thickness. Measurements were taken after each annealing step at room temperature. I, II and III mark the three annealing temperature regimes. An estimated error of ± 50 Oe was added to the extracted field values.

not fulfilled for any sample with a $\mathrm{TaN_x}$ interlayer throughout a broad range of the investigated temperature window.

The results of the annealing series for the samples with $t_{\mathrm{Ta}} = 10$ nm and varying $\mathrm{TaN_x}$ thickness are presented in Fig. 3.19. The development of exchange bias (Fig. 3.19 a)) resembles the one observed for $t_{\mathrm{Ta}} = 3$ nm. Exchange

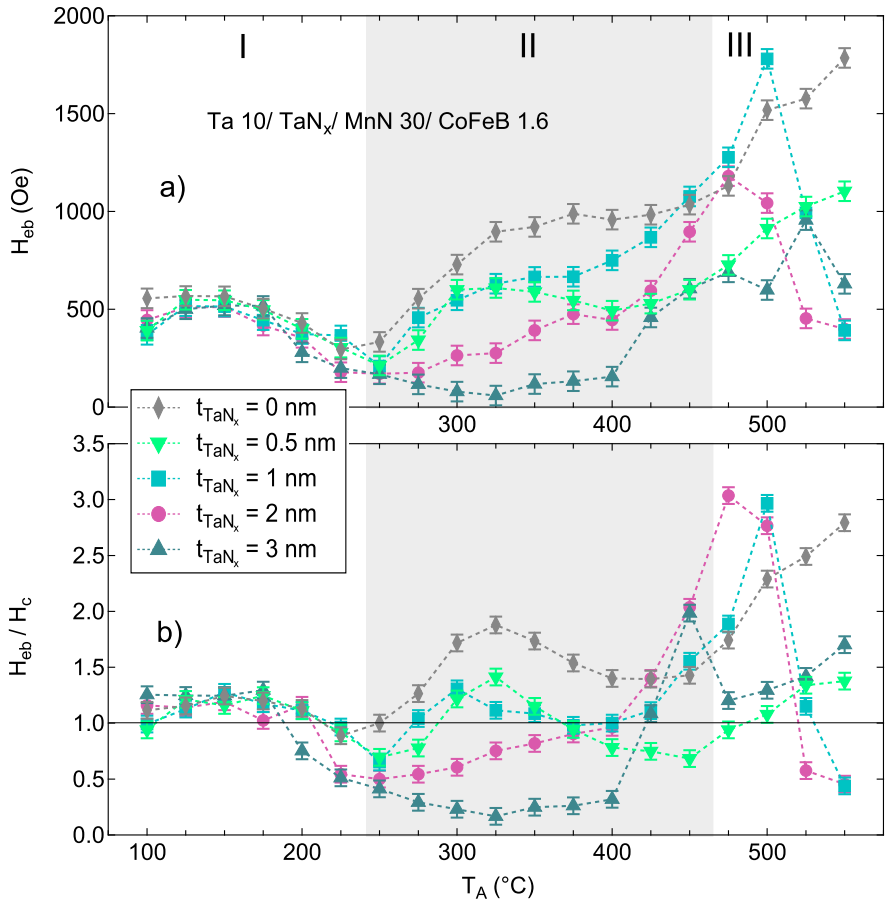

Figure 3.19: a) Exchange bias and b) Ratio $H_{\mathrm{eb}}/H_{\mathrm{c}}$ as a function of the annealing temperature T_{A} for Ta/ MnN/ CoFeB exchange bias samples with a 10 nm buffer layer of Ta and an additional TaN_x interlayer of varying thickness. Measurements were taken after each annealing step at room temperature. I, II and III mark the three annealing temperature regimes. An estimated error of ± 50 Oe was added to the extracted field values.

bias values lie around $H_{\mathrm{eb}} = 500$ Oe for all samples in the first temperature regime. This is followed by strongly varying behavior for the different TaN_x thicknesses in regime II. The two samples with the thickest TaN_x interlayers exhibit low exchange bias without a local maximum in the second regime while the samples with thinner TaN_x reach the typical plateau. At higher annealing temperatures, all samples show increasing exchange bias. The

behavior in the third temperature regime seems to be even more complicated here than it was for $t_{Ta} = 3\,nm$. Due to the thicker Ta buffer layer, i.e. larger nitrogen drain, diffusion becomes especially important. The samples with 1, 2 and 3 nm TaN_x exhibit a maximum around $T_A > 500°\,C$ and then lose their exchange bias, whereas the one with only 0.5 nm TaN_x shows steadily increasing values. This observation stands in contrast to our hypothesis that thicker TaN_x layers yield better thermal stability. Possibly, there are phase transistions happening in the MnN layer that support stable exchange bias in the sample with 0.5 nm TaN_x.

Overall, the exchange bias values are slightly higher in the case of $t_{Ta} = 10\,nm$ than for $t_{Ta} = 3\,nm$. This can be attributed to the better crystallinity of MnN when thicker Ta layers are used, which goes in line with the results of the Ta thickness series discussed above. Nevertheless, mostly low ratios H_{eb}/H_c are observed (Fig. 3.19 b)). Values of one are only exceeded in some parts of the temperature range, depending on the TaN_x thickness. However, these results show that a specific TaN_x thickness can be used to tune the thermal stability

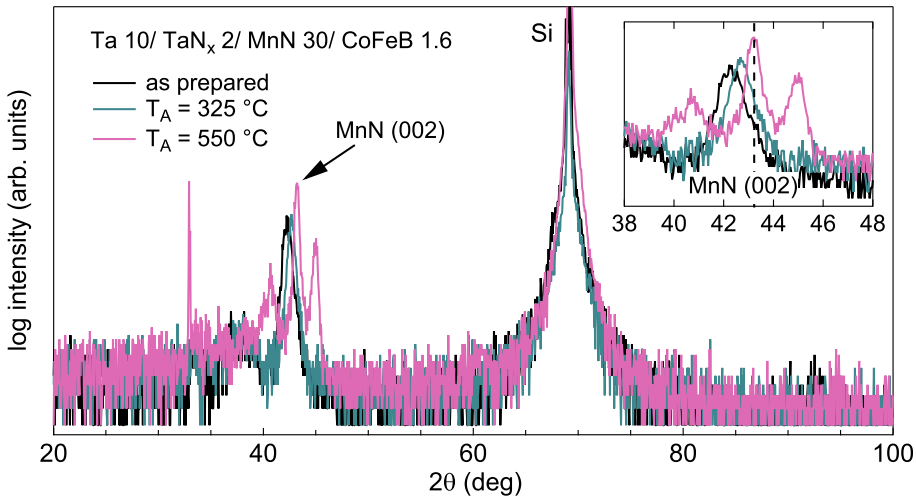

Figure 3.20: X-ray diffraction pattern of a Ta/ MnN/ CoFeB sample with 10 nm Ta and a 2 nm TaN_x interlayer as prepared and after annealing at $T_A = 325°\,C$ and $T_A = 550°\,C$, respectively. The inset shows a zoom-in around the angular range of the (002) peak of MnN.

at a given temperature. For example, using 2 nm TaN_x, especially high ratios are observed for $T_A = 450 - 500°$ C.

To gain a deeper understanding about the influence of diffusion and crystallization processes, especially at high annealing temperatures, x-ray diffraction scans were performed for all samples with $t_{Ta} = 10$ nm and varying TaN_x thickness. In Fig. 3.20, the diffraction patterns measured for the sample with $t_{Ta} = 10$ nm and $t_{TaN_x} = 2$ nm directly after preparation and after annealing at $T_A = 325°$ C (regime II) and $T_A = 550°$ C (regime III) are displayed. The lattice constant of MnN before annealing is $c = 4.276$ Å, which agrees well with the value determined for the sample without an additional layer of TaN_x (cf. Fig. 3.17).

Again, MnN's lattice constant decreases with increasing annealing temperature, yielding $c = 4.185$ Å after annealing at $T_A = 550°$ C, which also matches the result obtained for the sample without TaN_x. This means an interlayer of TaN_x does not change the crystallographic properties of MnN in terms of lattice parameters. Yet, the rocking curves of MnN's (002) peak, presented in Fig. 3.21, reveal the main crystallographic transformation that TaN_x induces. In Fig. 3.21 a), the rocking curve for the sample with 2 nm TaN, corresponding to Fig. 3.20, directly after preparation is shown. With 11.47°, the FWHM of MnN's (002) peak is more than twice as broad as in a similar sample without

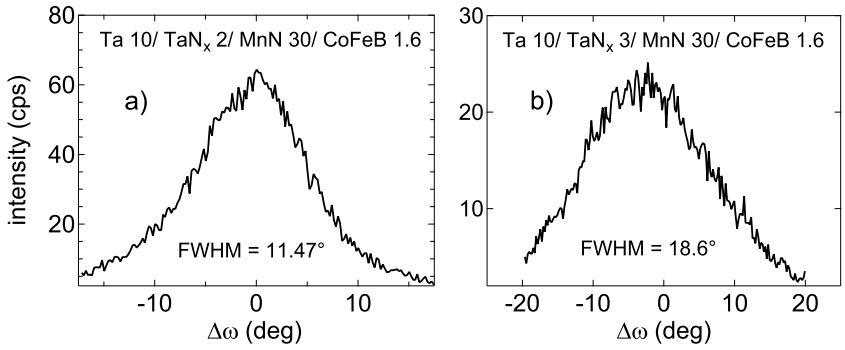

Figure 3.21: Rocking curves of the MnN (002) peak for Ta/ MnN/ CoFeB samples with 10 nm Ta and a) 2 nm TaN_x or b) 3 nm TaN_x. The curves were measured directly after preparation of the samples.

TaN_x (cf. Fig. 3.16). Using an interlayer of 3 nm TaN_x, it even increases to 18.6° as can be seen in Fig. 3.21 b). The thicker the TaN_x layer is, the more of MnN's crystallites are tilted away from the film normal. MnN grows less uniformly orientated and with a probably smaller lateral grain diameter, resulting in reduced exchange bias values.

Remarkably, judging solely from the x-ray diffraction results, TaN_x does not seem to prevent nitrogen diffusion significantly, as the lattice constant of MnN decreases similarly strong after annealing, with or without the layer of 2 nm TaN_x. However, other changes to the structure are observable after annealing at $T_A = 550°$ C. Two additional peaks arise near the MnN (002) peak (cf. inset Fig. 3.20).

In Fig. 3.22 a), x-ray diffraction scans around the angular range of the MnN (002) peak for all TaN_x thicknesses directly after preparation are displayed. It is obvious that with increasing TaN_x thickness the crystallinity of MnN decreases. This is in line with the results of the rocking curves and the observation of very low exchange bias for the samples with $t_{TaN_x} = 2$ nm and 3 nm. After annealing at $T_A = 550°$ C, the MnN peak narrows and additional

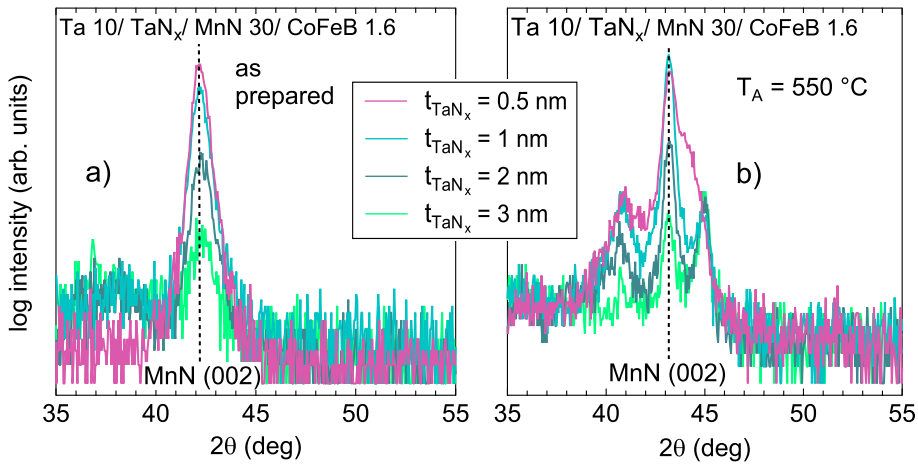

Figure 3.22: Diffraction scans around the angular range of MnN's (002) peak for Ta/ MnN/ CoFeB samples with 10 nm Ta and different TaN_x thicknesses detected a) Directly after preparation and b) After annealing at $T_A = 550°$ C.

peaks arise for all TaN_x thicknesses (Fig. 3.22 b)). Notably, the MnN (002) peak's intensity decreases with increasing TaN_x thickness, whereas the peak at 45° is nearly independent of the TaN_x thickness. Only for the sample with 0.5 nm TaN_x it is located at smaller angles and therefore lies in the shoulder of the MnN peak. This curve looks remarkably similar to the diffraction results obtained for the Ta thickness series in Fig. 3.17b). However, there, the peak in the MnN (002) peak's shoulder was only observed for $t_{Ta} < 10$ nm. Even a thin interlayer of 0.5 nm TaN_x thus significantly changes the crystallographic properties.

To clarify whether the additional peaks that are observed after high-temperature annealing originate from the $Ta(N_x)$, the MnN or the ferromagnetic layer, further x-ray diffraction measurements were performed after subsequently etching off single layers with Ar ion bombardment. The results are displayed in Fig. 3.23 for the sample with $t_{Ta} = 10$ nm and $t_{TaN_x} = 2$ nm. First, the capping layer, the CoFeB layer and about 5 nm MnN were etched off. All three peaks are still detectable. Thus, we can conclude that they do not result from the formation of a nitride in the ferromagnetic layer. However, the $\theta-$MnN (002) peak (b) loses a significant amount of intensity whereas peak (a)'s intensity only decreases weakly and peak (c) is nearly not influenced at all. These observations suggest that peaks (a) and (c) relate to crystallites that are located closer to the MnN/ TaN_x interface than to the CoFeB/ MnN interface.

Next, the complete MnN layer was etched off, so that Ta and TaN_x are the only layers left on the sample. This leads to the total disappearance of all peaks. Consequently, peak (a) and (c) must be originating from other, nitrogen-poor, Mn−N phases that form during annealing. Peak (a) could be identified as the (111) peak of ferrimagnetic $\varepsilon - Mn_4N$ [82] or the (002) peak of $\zeta - Mn_2N$ [83]. These nitrogen-poor phases might form very close to the TaN_x interface as much of the nitrogen has been lost due to diffusion here. Peak (c) could correspond to the (200) or (006) peak of antiferromagnetic $\eta - Mn_3N_2$ [84]. Assuming the peak is in fact the (200) peak, the c-axis of the $\eta - Mn_3N_2$ would lie in the plane. This would result in a compensated interface between $\eta - Mn_3N_2$ and CoFeB as well as magnetic moments aligning

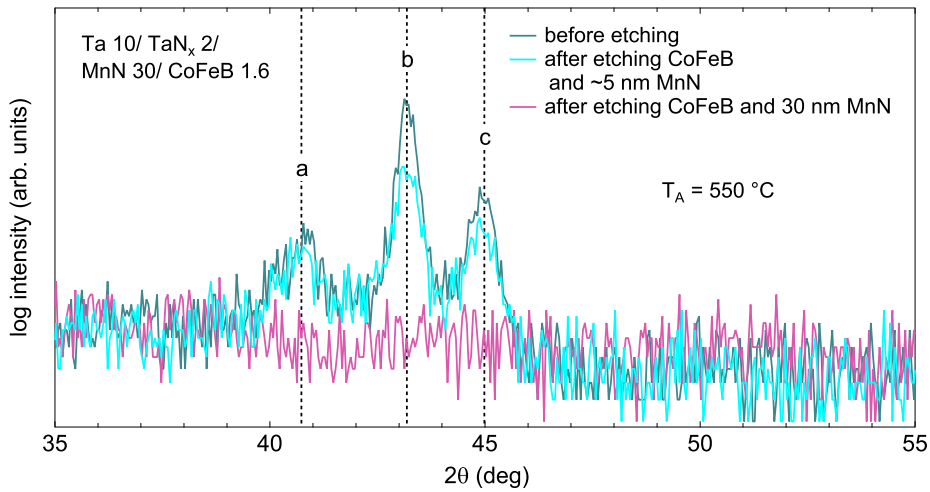

Figure 3.23: X-ray diffraction scan of a Ta/ MnN/ CoFeB sample with 10 nm Ta and 2 nm TaN_x after annealing at $T_A = 550°$ C for the full stack and after etching single layers off with Ar ion bombardment, respectively.

perpendicularly to the film plane, leading to a reduction of exchange bias [35]. This result would be consistent with the observed reduction of exchange bias at high annealing temperatures.

Summarizing the effects of introducing a TaN_x layer, it gets clear that there is no optimum TaN_x thickness that guarantees high exchange bias and increased thermal stability at the same time. Thick TaN_x layers reduce the crystalline quality of MnN and thus also the exchange bias. In fact, the TaN_x might not only act as barrier for nitrogen diffusion but also induce phase transitions during annealing that are not fully understood at this point. In any case, the detrimental effects of the TaN_x interlayer on the crystallography of the MnN films seem to outweigh possible positive effects of inhibiting nitrogen diffusion. However, the crystallographic quality does not seem to be the only driver of high exchange bias in this complex trilayer system. Additionally, these results show that during sample preparation it can be especially important to minimize the exposure time of the bare Ta layer to the nitrogen plasma before the deposition of MnN, preventing the unintended formation of a TaN_x layer.

Chapter 4

Spin-orbit torque induced electrical switching of MnN

This chapter deals with spin current induced electrical switching of the Néel order in MnN [85]. In the introduction, fundamental effects and mechanisms contributing to the electrical switching of antiferromagnets, namely the spin Hall effect and the concept of spin torques, are presented. Furthermore, both the mechanism of the intrinsic Néel order spin-orbit torque as well as spin current induced switching, including corresponding prior experimental results, are introduced.

Following, an overview about the sample preparation and device geometry as well as the setup used for the electrical transport measurements is given. Thereafter, the results investigating electrical switching in MnN are discussed. After introducing the measurement scheme and fitting procedure, temperature and current density dependent findings as well as reproducibility tests and a grain size distribution analysis are presented. Additionally, calculations and results concerning Joule heating in the samples are analyzed. Lastly, the possible read-out mechanisms enabling the detection of the reorientation of the Néel order are briefly introduced and studied.

4.1 Introduction

4.1.1 The spin Hall effect

The spin Hall effect (SHE) converts a charge current into a transverse spin current via spin-orbit coupling (SOC) in any conducting material [86, 87, 88]. Similarly to the anomalous Hall effect (AHE) in ferromagnets that was discovered in 1881 by Edwin Hall [24], conduction electrons acquire opposite transverse velocities depending on their spin orientation due to spin-dependent scattering. However, as there is no spin polarization in non-magnetic materials, these spin-dependent transverse velocities do not result in a transverse voltage but a spin accumulation at the edges of the sample, as illustrated in Fig. 4.1 a).

For the SHE as well as the AHE, there are three different mechanisms that can cause an electron to obtain a (spin-dependent) transverse velocity: spin skew scattering, side jump scattering or intrinsic effects [87]. In case the transverse velocity is acquired in between scattering events, this is due to intrinsic effects that originate solely from the influence of SOC on the electronic band structure of the crystal and can be described in terms of berry curvature as presented in [89]. In contrast to that, spin skew scattering and side jump scattering, referred to as extrinsic mechanisms, act on the electron during the scattering event. Here, spin skew scattering results in spin-dependent momentum directions after the scattering event as SOC gives rise to an effective magnetic field gradient within the scattering plane. In case of side jump scattering, electrons experience a spin-dependent acceleration and deceleration during scattering due to an effective magnetic field gradient along

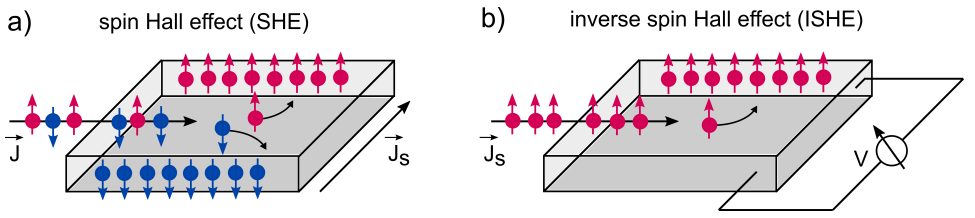

Figure 4.1: Schematic illustration of a) The spin Hall effect converting a charge current $\vec{J}$ into a transverse spin current $\vec{J}_s$ and b) The inverse spin Hall effect converting a spin current into a transverse charge current.

the incoming and outgoing momentum direction originating from SOC. This leads to a spin-dependent sideway displacement upon repeated scattering [86].

Even though the SHE had been theoretically predicted and described since 1971 [90], it took several decades until its first optical and electrical observation in an experiment [91, 92]. It was found that in very clean samples, the dominant mechanism contributing to the SHE is the spin skew scattering because it scales linearly with the momentum relaxation time τ. Side jump scattering and intrinsic effects do not depend on the relaxation time and become more important in samples with a high impurity concentration [86]. Independent of the dominant mechanism, the spin Hall angle θ_{SH} defines the efficiency of the conversion from charge to spin current via

$$\theta_{\mathrm{SH}} = \frac{j_{\mathrm{s}}}{j}, \tag{4.1}$$

where j denotes the charge current density and j_{s} the spin current density. Since the SHE arises from SOC interactions, which get stronger with increasing atomic number, the spin Hall angle is especially high in heavy elements [86]. Thus, in our experiments, a Pt layer is used for the generation of an efficient spin current that later acts on the magnetic moments in the MnN layer.

The spin-dependent scattering mechanisms introduced above cannot only give rise to the SHE but are also the source of a similar effect in a reserved geometry called the inverse spin Hall effect (ISHE). When a spin current $\vec{J}_{\mathrm{s}}$ is injected into a heavy metal layer, a transverse charge current is generated. This is illustrated in Fig. 4.1 b). Spin-dependent scattering deflects most of the spin-up electrons to one side of the sample. As there are no spin-down electrons present that could be scattered in the opposite direction, the spin accumulation that arises is accompanied by a charge accumulation that can be measured as a voltage V between the sample's edges. As such voltage is quite simple to measure, the ISHE provides a very fast and convenient way of detecting a spin current.

4.1.2 Spin torques

Spin torques transfer angular momentum to a ferro- or antiferromagnetic layer, acting on the atomic magnetic moments and thus manipulating the magnetization $\vec{M}$ or the Néel vector $\vec{L}$, respectively [93]. In general, there are two different types of spin torques that can be distinguished depending on their source. While spin-transfer torques (STTs) are associated with a spin-polarized current originating in an adjacent ferromagnetic layer, spin-orbit torques (SOTs) arise from a spin current that is generated in a non-magnetic adjacent layer, either by the spin Hall or the Rashba effect [94, 95]. In the following, both types of spin torques will be briefly introduced in the context of manipulating the magnetization of a ferromagnet. Afterwards, it will be explained in more detail how spin torques can influence the Néel order in an antiferromagnet.

In the configuration of two adjacent ferromagnetic layers, where one layer is free and the other one used to generate a spin-polarized current, the STT can simply be understood in terms of global angular momentum conservation. The carriers that are injected in the free layer transfer spin angular momentum that is converted to magnetization angular momentum. The corresponding torque $\vec{\tau}$ is driven by an effective magnetic field that is proportional to the non-equilibrium carrier spin polarization $\vec{S}$ in the free ferromagnetic layer and is given by

$$\vec{\tau} = \frac{\mathrm{d}\vec{M}}{\mathrm{d}t} = \vec{M} \times \vec{S}, \tag{4.2}$$

where $\vec{M}$ denotes the magnetization of the free layer. Depending on the carrier's spin lifetime with respect to the spin precession time in the free ferromagnet, different mechanisms play a role in terms of momentum transfer. In the case of short carrier lifetime, the non-equilibrium spin polarization $\vec{S}$ is approximately equal to the polarization of the injected spin current $\vec{p}$. Since this configuration is analogous to applying an external magnetic field to the free layer, the corresponding torque is called field-like. In contrast to that, for long carrier lifetimes, the injected spins precess around the magnetization of the free ferromagnet, thus $\vec{S} \approx \vec{M} \times \vec{p}$. As this type of precessional torque can contribute to or compete with the Gilbert damping, it is referred to

as (anti)damping-like. The field-like and damping-like torques can thus be expressed by

$$\vec{\tau}_{\text{field}} \approx \vec{M} \times \vec{p} \qquad \text{and} \qquad \vec{\tau}_{\text{damping}} \approx \vec{M} \times \left(\vec{M} \times \vec{p}\right), \tag{4.3}$$

respectively [93].

Similar torques can act on the magnetization of a ferromagnetic film when it is brought in contact with a normal (heavy) metal with a non-equilibrium density of spin-polarized conduction electrons. Here, the spin polarization arises due to SOC in the metallic layer and interacts with the magnetic moments in the ferromagnet through exchange coupling [95]. In the simple setup of a ferromagnetic layer adjacent to metallic layer, the non-equilibrium spin density can be induced by applying a charge current that is then converted to a spin current via the SHE [94]. The absorption of spin current then causes the transfer of spin torque to the magnetic moments in the ferromagnet given the applied current density is high enough. Additionally, in a normal metal/ ferromagnet/ oxide multilayer system, a non-equilibrium spin polarization can be induced by a structure inversion asymmetry along the surface normal, called Rashba effect [95]. SOTs originating from the Rashba effect are usually dominated by field-like torques, whereas spin currents generated by the SHE mostly result in (anti)damping-like torques [93].

Recently, it was found that spin torques cannot only manipulate magnetic moments in ferro-, but also in antiferromagnets [96]. Similarly, spin torques acting on antiferromagnets can either arise due to spin-polarized currents originating from adjacent ferromagnets (STT) or spin currents that are generated in adjacent heavy metal layers (SOT). Furthermore, the magnetic order in antiferromagnets can be manipulated via an intrinsic Néel order spin orbit torque (NSOT) [10]. These phenomena are described in detail in the following.

4.1.3 Switching of antiferromagnets

Even though antiferromagnets have been known and studied since the 1930s, up until recently there has been no efficient way to manipulate their magnetic order [17]. While this provides their unique ability of storing information that is protected against external electric or magnetic fields, the search for mechanisms to control the Néel order, enabling the use of antiferromagnets as active components in spintronic devices, has been going on for years [12]. However, in 2016, Wadley et al. [10] found that the Néel vector in antiferromagnetic CuMnAs can be switched via electrical current pulses.

The underlying relativistic effect resulting in the so-called intrinsic Néel order spin-orbit torque (NSOT) only occurs in layered antiferromagnets that have a special crystal symmetry: The two magnetic sublattices with magnetic moments $\vec{m}_1 = -\vec{m}_2$ need to be structural inversion partners. Accordingly, the material needs to exhibit a combined parity-time (PT) symmetry [97]. In antiferromagnetic crystals where this is fulfilled, an electrical current $\vec{J}$ flowing through the lattice induces locally non-equilibrium spin polarizations $\vec{p}_1 = -\vec{p}_2$ due to the inverse spin galvanic effect [14]. These staggered fields give rise to a field-like SOT acting on the magnetic moments of the two sublattices with opposite sign. As a result, the Néel vector $\vec{L} = \vec{m}_1 - \vec{m}_2$ rotates to align perpendicular to the applied current. As the direction of the current determines the sign of the induced staggered fields, each polarity favors one of the two possible orientations where $\vec{L} \perp \vec{J}$.

The reorientation of the magnetic moments can be detected via the anisotropic magnetoresistance (AMR) [98] in a planar Hall effect geometry. Even though this only provides spatially averaged information in multidomain films, it clearly shows that manipulation of the Néel order via current pulses is possible in antiferromagnetic CuMnAs films. Switching amplitudes around 10 mΩ were achieved [10]. Since then, NSOT switching in CuMnAs has been investigated in several other studies, addressing the importance of thermal activation in the switching process [97] and observing the switching via direct imaging [99]. Intrinsic NSOT switching had initially been predicted and has also been observed for antiferromagnetic Mn_2Au [21, 100, 101, 102]. This material has a

similar structural and magnetic symmetry to CuMnAs and might be an even more interesting candidate for future application, providing higher conductivity than CuMnAs and a high Néel temperature [103]. Nevertheless, since there is only a very limited number of metallic antiferromagnets that provide the required complex unit cell structure for intrinsic NSOT switching [104], the search for methods to control magnetic moments in a larger variety of antiferromagnetic materials has been going on.

Very recently, it was shown that the manipulation of the Néel order in antiferromagnets is not only possible by an intrinsic SOT but can also be achieved via an externally induced spin polarization that is generated in an adjacent heavy metal layer [20, 25, 105, 106]. Even though the underlying mechanisms of this spin current induced SOT switching in antiferromagnets are not yet fully understood, two different models have been developed to describe its characteristics [20, 25]. They are presented in the following.

Firstly, spin-orbit torques in antiferromagnets can be phenomenologically described by slightly modifying the model introduced for spin torques in ferromagnets [107]. As they do not have a net magnetization, for antiferromagnets it is more convenient to consider a spin current exerting a torque on a spin centered at a particular atomic site, restoring spin conversion locally. Thus, the sublattices i of an antiferromagnet can be considered separately, originating in a local torque

$$\vec{\tau_i} = \vec{M_i} \times \vec{S_i}, \tag{4.4}$$

determined by the local sublattice magnetization $\vec{M_i}$ and the corresponding non-equilibrium carrier spin polarization $\vec{S_i}$. Accordingly, field-like and (anti)damping-like torques can be defined. Fig. 4.2 schematically illustrates how these torques act on an antiferromagnetic layer with two sublattices [107]. In an adjacent heavy metal layer, a spin current is generated via the SHE, driving a spin polarization $\vec{p}$ towards the interface. This polarization is similar for both sublattices: $\vec{p_1} = \vec{p_2} = \vec{p}$. Since the field-like torque is driven by a non-staggered effective magnetic field proportional to $\vec{S} \approx \vec{p}$, it would have no effect on the antiferromagnet's Néel order. This is similar to the insensitivity

of antiferromagnets to external magnetic fields up to a critical value where a spin-flop transition occurs, typically lying in the range of several Teslas [107]. However, considering the (anti)damping-like torque, the two non-equilibrium spin polarizations $\vec{S}_1$ and $\vec{S}_2$ are given by

$$\vec{S}_1 \approx \vec{M}_1 \times \vec{p} \quad \text{and} \quad \vec{S}_2 \approx \vec{M}_2 \times \vec{p}. \tag{4.5}$$

Since the sublattice magnetizations $\vec{M}_1$ and $\vec{M}_2$ have opposite signs, the corresponding non-equilibrium field proportional to $\vec{S}_i$ is also staggered and thus as effective in an antiferromagnet as in a ferromagnet. Accordingly, (anti)damping-like torques

$$\vec{\tau}_i \approx \vec{M}_i \times \left(\vec{M}_i \times \vec{p}\right) \tag{4.6}$$

act on the sublattice magnetizations as illustrated in Fig. 4.2 and may rotate them towards each other. The resulting magnetic moment $\vec{m}$ that is induced by the canting of the sublattice magnetizations tries to align parallel to the spin polarization $\vec{p}$. When the sublattice magnetizations have been rotated

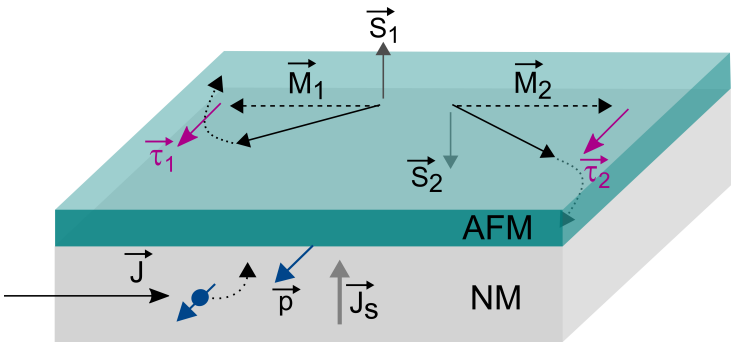

Figure 4.2: Schematic illustration of the generation of (anti)damping-like torques $\vec{\tau}_1$ and $\vec{\tau}_2$ acting on the two mangetic sublattices in an antiferromagnet (AFM). A spin current $\vec{J}_S$ forms in an adjacent non-magnetic heavy-metal layer (NM), i.e. via the SHE, driving a spin polarization $\vec{p}$ towards the interface. This spin polarization interacts with the two sublattice magnetizations of opposite sign, generating two non-equilibrium sublattice spin polarizations $\vec{S}_1$ and $\vec{S}_2$. The resulting torques move the sublattice magnetizations $\vec{M}_1$ and $\vec{M}_2$ away from their original position (dashed lines) towards each other (solid lines) [107].

far enough out of the plane, $\vec{m}$ vanishes. In this mechanism, the spin torques induce a perpendicular alignment of the Néel vector towards the initial spin polarization of the spin current [107]. Antiferromagnetic switching consistent with this model has been experimentally observed by Baldrati et al. [25].

In contrast to the above-mentioned mechanism, spin current induced SOT switching resulting in a parallel alignment of Néel vector and spin polarization has recently been observed in an experiment by Moriyama et al. [20]. The geometry and mechanism of this SOT induced switching are illustrated in Fig. 4.3 [20]. Applying a write current $\vec{J}_{\mathrm{W}}$ to the heavy metal/ antiferromagnet/ heavy metal trilayer stack, a spin current $\vec{J}_{\mathrm{S}}$ is generated in both heavy metal layers. The resulting spin polarizations at the interface at the top and bottom layer are of opposite sign. Those spin polarizations now interact with the magnetic moments in the antiferromagnet by exerting a torque $\vec{\tau}$. As there are similar torques working from the top and bottom layer, the moments can efficiently rotate without an increase of exchange energy. Obviously, the latter is only true in case the antiferromagnet has oppositely orientated spins at the top and bottom interface. Even though this might not hold for the complete film, there is a strong chance that it is true at least in some of the antiferromagnetic domains.

To investigate this SOT induced switching, Moriyama et al. [20] studied an epitaxially grown layer stack consisting of the antiferromagnetic insulater NiO sandwiched between two Pt films. The samples were structured into a Hall bar geometry and the rotation of the antiferromagnetic moments was detected as a change of transverse resistance via the spin Hall magnetoresistance (SMR) originating in the adjacent Pt layers. Maximum switching amplitudes of 112 mΩ were measured. While it was observed that in this geometry the Néel order turns to align perpendicular to the writing current $\vec{J}_{\mathrm{W}}$, other studies of SOT induced switching in NiO found that the moments rotate towards a parallel orientation with $\vec{J}_{\mathrm{W}}$ [105], consistent with the model developed by Baldrati and Gomonay et al. [25, 107].

At this point, it is not fully clear which model best describes the spin current induced switching in antiferromagnets, or wether different mechanism come

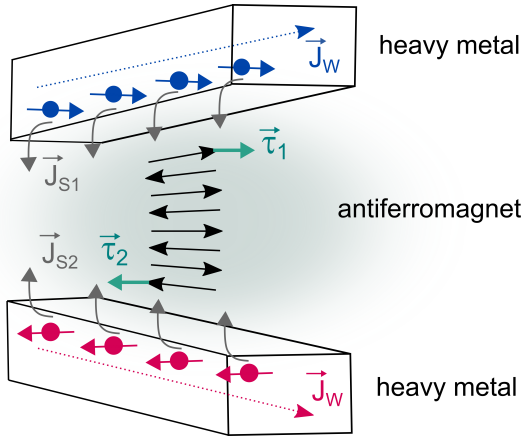

Figure 4.3: Schematic illustration, adapted and modified from [20], of spin current induced SOT switching. By applying a writing current $\vec{J}_W$, spin currents $\vec{J}_{S1}$ and $\vec{J}_{S2}$ are generated in the heavy metal layers via the SHE. Those spin currents then exert a torque $\vec{\tau}_1$ and $\vec{\tau}_2$ on the magnetic moments in the antiferromagnet, slightly rotating the Néel order [20].

into play at the same time. Possibly, the spin diffusion length of the antiferromagnet plays a role. In the case of a short spin diffusion length, the mechanism observed by Moriyama et al. may be dominant, as mostly interfacial magnetic moments of the antiferromagnet are rotated. This yields a parallel alignment of the Néel vector and the spin polarization. For antiferromagnets with longer spin diffusion lengths, on the other hand, the mechanism according to Baldrati et al. might play a more significant role, resulting in a perpendicular alignment of the Néel vector and the spin polarization. However, even though the underlying mechanisms have yet to be further investigated, SOT induced switching in antiferromangets has already been verified via direct imaging in several studies [25] and provides a very promising possibility for future application in spintronic devices.

Since, in contrast to intrinsic NSOT switching, the spin polarization invoking the torque on the Néel order originates from a secondary layer and not the antiferromagnet itself, SOT induced switching does not impose any restrictions on the antiferromagnet's structural or magnetic symmetry. In general, switching via this mechanism is possible in any material as long as the antiferromagnet's anisotropy is not too high and a sufficiently strong spin current is

generated in the adjacent layer. This opens a new route for the manipulation of the Néel order in a broad class of antiferromagnetic materials. It has already been demonstrated that SOT induced switching is also possible in α-Fe_2O_3 [22, 108], in pillars of PtMn [109], and that Mn_2Au [110] can be manipulated via the SHE in a way distinct from the intrinsic NSOT.

For the possible future application of this switching mechanism to design antiferromagnetic memory devices, it would be especially interesting to study metallic and polycrystalline antiferromagnets. Hence, in the following, we investigate SOT induced electrical switching in antiferromagnetic MnN, which has a low anisotropy, meets criteria for device integration, and is thus a very promising candidate.

4.2 Sample preparation and device geometry

To investigate switching of the Néel order in MnN, samples following the setup depicted in Fig. 4.4 were prepared via DC magnetron sputter deposition in a BESTEC sputter system at room temperature. The MnN layer was reactively sputtered from an elemental Mn target in a sputtering gas ratio of 50 % Ar to 50 % N_2, following the procedure reported in Chapter 3.2.1. Film stacks with varying MnN thicknesses of $t_{\mathrm{MnN}} = 6, 9, 12$ nm were prepared. The Ta and the Pt layer were prepared using a source power of 50 W, an Ar gas flow of 10 sccm and a working pressure of $p_{\mathrm{w}} = 2{\times}10^{-3}$ mbar. X-ray diffraction measurements confirmed the polycrystalline growth of MnN in (001) direction.

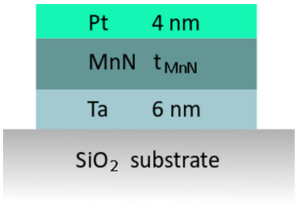

Figure 4.4: Schematic setup of the samples used for the switching experiments.

In polarized neutron reflectometry measurements on samples similar to those prepared for the switching experiments, the MnN films were found to be slightly rich in nitrogen and no magnetic scattering from the MnN films could be detected [80]. This excludes the possibility that electrical switching of ferrimagnetic Mn_4N precipitates contributes to the signals we investigate in the present study. Furthermore, no ferromagnetic signal was detected in MOKE measurements of the samples.

For the electrical switching experiments, the samples were patterned to star-shaped [10] structures as shown in Fig. 4.5 via electron beam lithography. In the first lithography process, the samples were coated with negative e-beam resist AR-N7520 and rotated for 30 s at a speed of 5000 rounds per minute in a spin-coater. Then, they were heated at 85° C for 2:30 min. The exposure was performed in a Keyence SEM, using an aperture of 60 μm, a voltage of 20 kV, an area dose of 300 μA/cm^2 and a step size of 0.02 μm at a working distance of 19.5 mm. To develop the resist, the samples were immersed into developer AR-300-47 for 7 min and cleaned by destilled water for 20 s. Using Ar ion bombardment, the samples were etched down to the silicon oxide

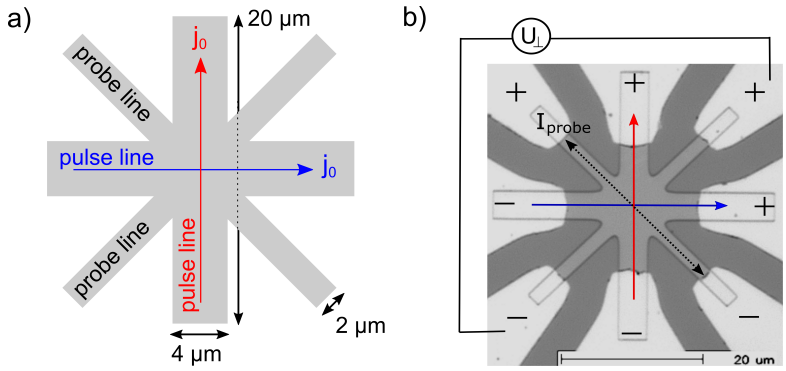

Figure 4.5: a) Schematic illustration of the star-shaped structures used in the electrical switching experiment. The pulse and probe lines are indicated accordingly. b) Optical micrograph of a star-shaped device after completion of the lithography process. The signs on the Au contact pads represent the connections to the positive/ negative differential outputs and inputs of the voltage sources and the lock-in amplifier. The red and blue arrows represent the physical current directions of polarity 1.

substrate. To conclude the first lithography process, the remaining resist was removed by immersion into NMP (N-Methyl-2-pyrrolidone) and ethanol in an ultra-sonic bath.

Following this, the contact pads were prepared. Therefor, the samples were coated with positive e-beam resist AR-P617.08 and rotated for 60 s at a speed of 5000 rounds per minute. Then, they were heated at 140° C for 10 min. For the exposure, an aperture of 60 μm, a voltage of 20 kV, an area dose of 170 μA/cm^2 and a step size of 0.03 μm at a working distance of 19.5 mm was used. For development, the samples were immersed into developer AR-600-55 for 2:30 min, followed by immersion into stopper AR-600-60 for $30 - 60$ s. Then, they were heated at 80° C for 2 min to clear off remaining solvents.

For the deposition of the contact pads, a custom-built sputter chamber was used. With a source power of 25 W, 4 nm Ta and 60 nm Au were deposited onto the patterned samples via DC sputtering. Again, to remove the remaining resist, the samples were immersed into NMP and ethanol in an ultra-sonic bath. Lastly, the samples were fixed on a chip carrier and the single structures were wired with Au bonds for transport measurements.

The star-shaped structures consist of two perpendicular pulse lines with a width of $w = 4\,\mu$m and two thinner probe lines (cf. Fig. 4.5 a)), all having the same length of $l = 20\,\mu$m. For the switching experiments, current pulses with a nominal current density of

$$j_0 = \frac{I_0}{wd} = \frac{U_0}{Rwd_{\mathrm{tot}}} \tag{4.7}$$

were applied to the pulse lines as indicated with the red an blue arrows. R denotes the pulse line resistance and d_{tot} the total metallic film thickness of the sample. However, as the current does not flow trough all metallic layers homogeneously due to their different resistivities, further measures were necessary to find the actual current density in the individual layers. Therefor, the resistivities of the MnN and Ta layer were both determined via four-point measurements [111] on suitable reference samples using the relation

$$\rho_{\mathrm{x}} = \frac{\Delta U}{I} \cdot k \cdot d_{\mathrm{x}}, \tag{4.8}$$

where ρ_{x} is the resistivity and d_{x} the film thickness of the corresponding layer. ΔU describes the potential difference that is induced when applying a current I through two electrodes. The factor k attributes for the measurement geometry. In case of an equidistant alignment of the four electrodes it takes a value of $\pi/\ln(2)$, given the measured sample is homogeneous and large enough to be considered as an infinite conducting sheet [112]. With this technique, the resistivities of the MnN and Ta layers were both determined to lie around $180\,\mu\Omega$cm.

Now, the Pt resistivity could be calculated using a parallel resistor model via

$$\rho_{\mathrm{Pt}} = d_{\mathrm{Pt}} \left(\frac{d_{\mathrm{tot}}}{\rho_{\mathrm{tot}}} - \frac{d_{\mathrm{Ta}} + d_{\mathrm{MnN}}}{\rho_{\mathrm{Ta,MnN}}} \right), \tag{4.9}$$

where ρ_{tot} was determined from the pulse line resistance

$$R = \rho_{\mathrm{tot}} l / w d_{\mathrm{tot}}. \tag{4.10}$$

As the resistivity of the Pt layer, which lies around 25 $\mu\Omega$cm, is significantly smaller than the one of Ta or MnN, most of the current flows through this layer, generating an efficient spin current that acts on the magnetic moments in the MnN. Thus, the applied current density is converted to the current density in the Pt layer

$$j_{\mathrm{Pt}} = \frac{U_0}{\rho_{\mathrm{Pt}} l} = j_0 \left(\frac{d_{\mathrm{tot}}}{d_{\mathrm{Pt}}} - \frac{\rho_{\mathrm{tot}} (d_{\mathrm{Ta}} + d_{\mathrm{MnN}})}{\rho_{\mathrm{Ta,MnN}}\ d_{\mathrm{Pt}}} \right) \tag{4.11}$$

after each switching measurement for better comparability. Eventually, this calculated current density is corrected for the inhomogeneous current flow in the center-region of the star structure by a factor of 0.6, which is derived in detail in the Appendix of [97]. Consequently, for all measurements presented in the following the current density j_{Pt} refers to the center-region current density in the Pt layer.

4.3 Setup for electrical transport measurements

For the electrical switching experiments, the structured samples were placed into a closed-cycle He cryostat that ensures stable measurement temperatures T_s in a range from 130 K to 300 K. Then, the star-shaped Hall crosses were connected to the measurement setup through a breakout box that was used for grounding the devices during structure or sample changes. A circuit diagram of the setup, including the complete measurement equipment, is illustrated in Fig. 4.6. The setup provides the possibility of purely differential measurements and is similar to the one described in [97].

Current pulses with a current density j_0 and a pulse width Δt are generated with an Agilent 33522A wave form generator and guided through the pulse lines of the star-shaped structure. A switchbox containing reed relais is used to direct the pulses to either the red or blue pulsing arm. If needed, an additional Tabor Electronics 9260 differential broadband amplifier can be added for pulsing. It provides a fixed amplification factor of 10 and a differential output voltage of ≤ 34 V. To monitor the pulse shape, a UNI-T UTD2052CEX digital storage oscilloscope is connected to the wave form generator. Since long current pulses cause significant heating and thereby possible destruction of the structures, single shorter pulses are grouped into bursts. Adjusting the number of pulses per burst

$$m(\Delta t, j_0) = \frac{Q}{\Delta t j_0 w d}$$

allows for a constant charge Q to be transferred per burst. For all experiments presented in this work, the charge per burst is kept constant at $Q = 1.68 \times 10^{-4}$ C and a current pulse width of $\Delta t = 4\,\mu$s is used. The duty cycle, indicating the ratio between the pulse width and the pulse duration, is set to 0.002. To ensure a constant nominal current density j_0, the pulse line resistances R are measured before every switching cycle via a two-point resistance measurement with a Keithley 2000 multimeter. This way, the pulse voltage

$$V(T_\mathrm{s}) = jwtR(T_\mathrm{s})$$

for the desired current density can be adjusted accordingly.

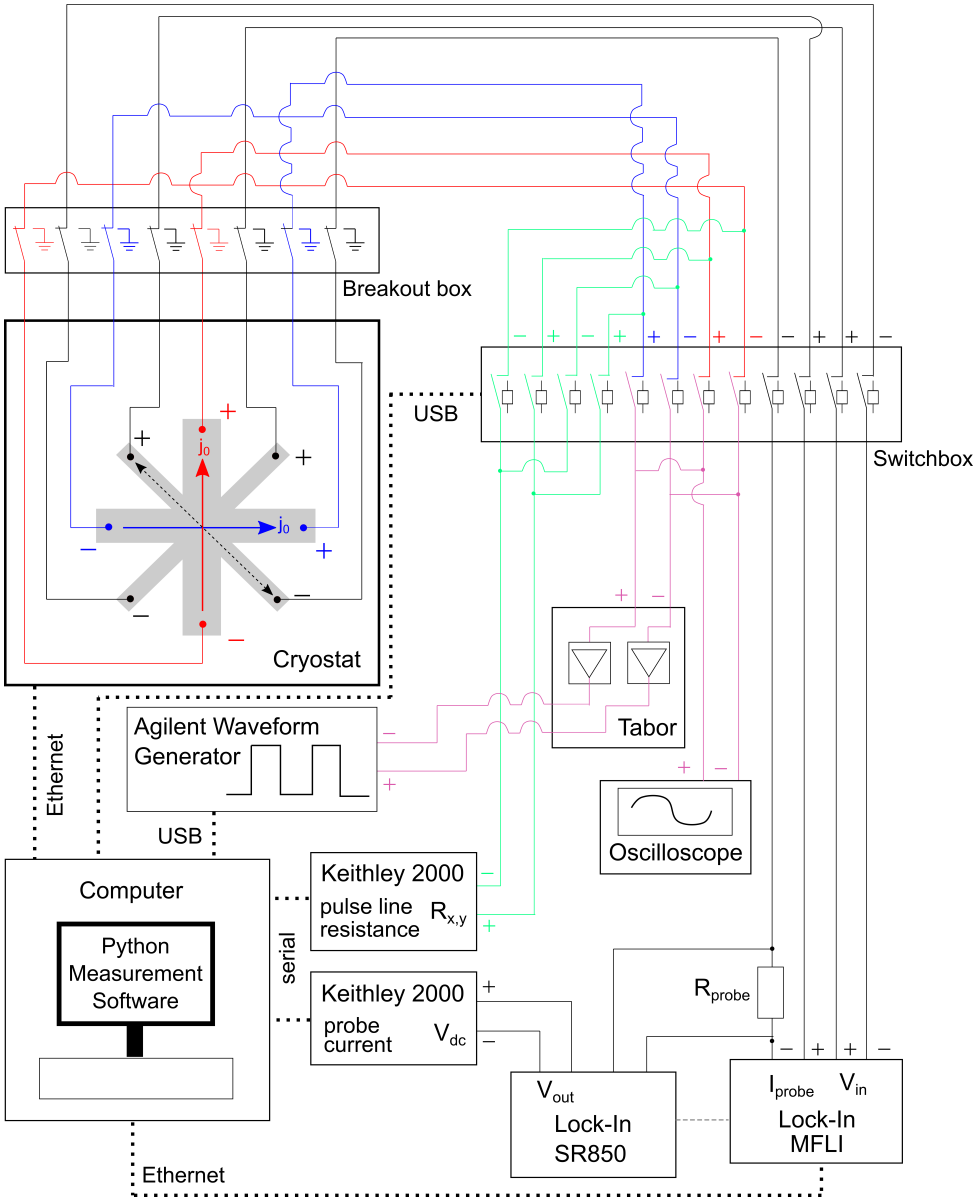

Figure 4.6: Schematic circuit diagram of the differential measurement setup for switching experiments, adopted and adjusted from [113]. The red and blue arrows in the star-shaped structure represent the physical current directions. The solid lines illustrate electrical connections with BNC cables and dotted lines represent connections to the computer operating the measurement software.

To detect changes to the magnetic orientation caused by the current pulses, the probe lines of the star-shaped structure are used. They are arranged in a typical planar Hall effect measurement geometry: A probe current is sent through one of the lines while the transverse voltage is measured perpendicular to it, giving rise to a transverse resistance

$$R_\perp = \frac{V_\perp}{I_{\text{probe}}}.$$

This read-out measurement is performed with a Zurich Instruments MFLI lock-in amplifier. The probe current I_{probe} is measured as a voltage drop over a known resistance $R_{\text{probe}} = 1\,\text{k}\Omega$ either via a second lock-in amplifier (Stanford Research Systems SR850) that is phase-locked to the MFLI or a Keithley 2000 multimeter. The transverse resistance is evaluated with a reference frequency of 81.3 Hz after every burst with a delay of 2 s to allow for equilibration of the system. The resistance change caused by the switching of the antiferromagnetic moments originates from either the planar Hall effect (PHE) or the spin Hall magnetoresistance (SMR), or both. A detailed discussion about the read-out mechanism follows in Chapter 4.5.

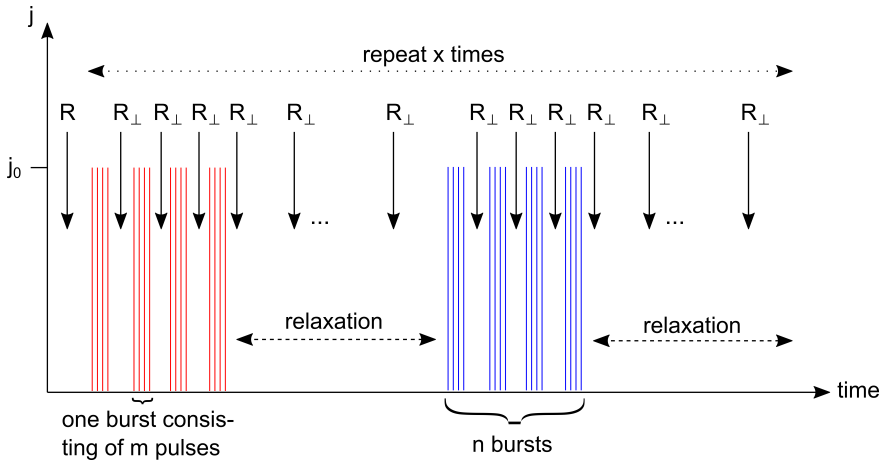

Figure 4.7: Illustration of a switching cycle consisting of x repeats of the presented switching sequence. Each sequence consists of a fixed number of n bursts in both pulsing directions, separated by a relaxation phase. Before the sequence is started, the pulse line resistances R are measured.

In Fig. 4.7, an illustration of a full switching sequence is shown. Before applying the first current burst, the pulse line resistances R are measured to adjust the pulse voltage accordingly. Then, a fixed number of n bursts, each consisting of m single current pulses that ensure a constant charge per burst, is applied to the first pulse line (red). In between the bursts, the transverse resistance $R_\perp$ is evaluated. Before changing the pulsing direction, the sample is left to relax for a fixed relaxation time. Here, the transverse resistance is again successively measured to observe the relaxation. Then, n bursts are applied to the other pulsing direction (blue) and the sample is left to relax again while the transverse resistance is evaluated. This sequence can then be repeated several times. For all presented switching measurements in this work, a full switching cycle consists of six repeats of 200 bursts per current direction and relaxation phases of 600 s. After the completion of such a cycle, it is repeated with inversed polarity.

4.4 Results

4.4.1 Polarity dependence

In Fig. 4.8 a), typical raw data of switching with positive or negative polarity is shown for the sample with 6 nm MnN. The background colors of the graph correspond to the pulsing direction indicated with the red and blue arrows

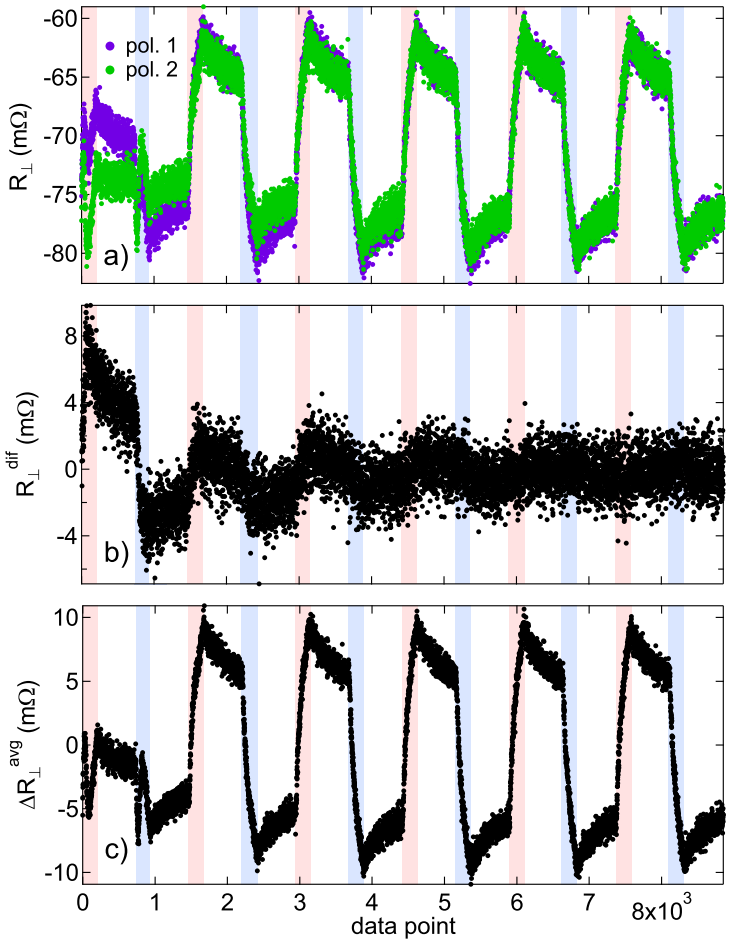

Figure 4.8: a) Raw $R_\perp$ traces from a switching experiment. Background colors correspond to pulsing the two pulse lines (red, blue) or the relaxation phase (white). b) Difference between the two polarities in a). c) Average of the two polarities with the offset removed.

in Fig. 4.5 b). After applying a fixed number of current bursts into the first pulsing direction, the sample is left to relax for 600 s. During the pulse phase, the time between two bursts is approximately 2.2 s, in the relaxation phase data are taken at 1 s intervals. After relaxation, the same number of current bursts is applied to the perpendicular pulsing direction, rotating the magnetic moments into the other direction. After another relaxation, this sequence is repeated. Clearly, reproducible switching can be observed after a short training phase at the beginning of the cycle.

To investigate the possible influence of the pulsing polarity, the differences and averages of the two polarities are calculated as can be seen in Fig. 4.8 b) and c), respectively. While the first two repeats show a clear dependence on the polarity, further cycles show only negligible influence of the polarity. This polarity independence is in line with the expected symmetry of the Néel order switching. Hence, for analyzing the switching traces, the focus is laid on the reproducible, polarity independent component of the measurement, i.e. the average over the two polarities after a training phase of three repeats. In the following, all switching traces refer to the polarity-averaged switching traces after three repeats of training.

4.4.2 Resistive contribution

Recent work on the switching of insulating antiferromagnets with the SHE of Pt suggests that the typical "saw-tooth" shape of the transverse voltage traces is related to a degradation effect in the Pt film [22, 108]. There are strong indications that this resistive contribution is caused by local annealing and crystallization at moderately high current density (reducing the resistivity locally) and by electromigration at high current density just below the destruction threshold (increasing the resistivity locally) [114].

To ensure that the electrical response in our experiment originates from the switching of the Néel order, several current density cycles were performed while closely monitoring the pulseline resistances, as was proposed to rule out resistive contributions in [114]. These measurements were performed after cycling of the temperature, minimizing the influence of resistance change

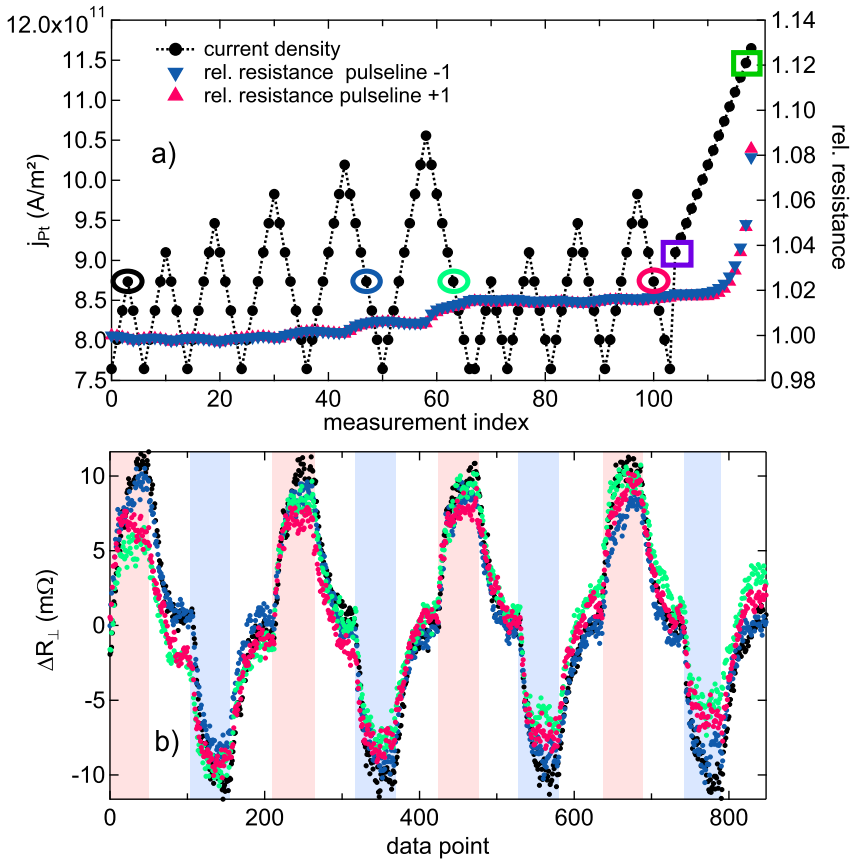

Figure 4.9: a) Current density sweeps, taken at room temperature for the 9 nm MnN sample. On the right axis, the development of the relative resistance of the two pulselines is shown. b) Selected switching traces at different stages of the current density sweeps, corresponding to the encircled data points in Fig. 4.9 a).

due to annealing-induced crystallization. The results are summarized in Fig. 4.9. While the pulseline resistances do not change during the first current density sweeps, a significant increase occurs when going to higher current densities in the fifth and sixth sweep (Fig. 4.9 a)). Small changes in the transverse response can be observed when looking at the switching traces in Fig. 4.9 b), corresponding to the encircled data points in Fig. 4.9 a). A small difference of the absolute switching amplitude is visible when comparing the

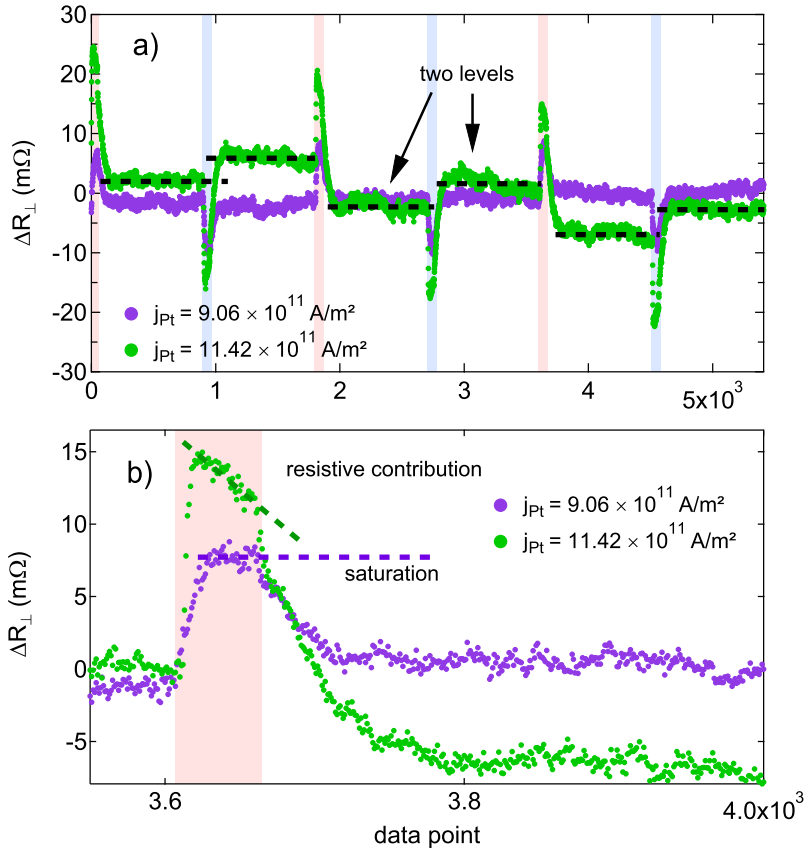

Figure 4.10: a) Switching traces measured at low and very high current density, respectively, corresponding to the data points marked with a square in Fig. 4.9 a). b) Zoom into Fig. 4.10 a) to illustrate the resistive constribution of the switching at high-current density. The dashed lines are guides to the eye.

black and the blue curve. This difference gets larger after sweeping up to $j_{\mathrm{Pt}} = 10.55 \times 10^{11}\,\mathrm{A/m^2}$ (green curve). The following cycle of sweeps, with smaller current densities, does not significantly change the amplitude further (pink curve).

After completion of these reproducibility tests, the current density was successively increased until destruction of the device. The pulseline resistances strongly increase with increasing current density, which is in line with the

observations in [114]. Fig. 4.10 a) shows a switching trace detected at relatively low current density compared to one measured with current density just below the destruction threshold (see squares in Fig. 4.9 a)). For the high-current density measurement, two different levels are observable during the relaxation phases, which are induced by the irreversible changes of local resistivity in the pulselines. This can also be seen by looking at a zoom-in of these switching traces, shown in Fig. 4.10 b). While the sample reaches saturation during the pulsing phase in the case of $j_{\mathrm{Pt}} = 9.06 \times 10^{11}\,\mathrm{A/m^2}$, a resistive contribution can be seen in the high-current density measurement. This destructive contribution only arises when applying $j_{\mathrm{Pt}} \gtrsim 11 \times 10^{11}\,\mathrm{A/m^2}$ and has a sign opposite to the low-current density contribution. Thus, the transverse response seen at lower current densities can be assigned to the magnetic reorientation, whereas the non-relaxing contribution of opposite sign seen at high current density originates from local changes of the resistivity. As we work with significantly smaller current densities in all of our presented measurements, we claim that the observed response is indeed of magnetic origin.

4.4.3 Quantitative analysis

In order to extract paramters like the switching efficiency or the relaxation time from the measured switching traces, a quantitative analysis of the data is performed. This allows for an independent and clear comparability between different measurements and thus facilitates the interpretation of the results. The method used for the quantitative analysis is adopted from a previous study on antiferromagnetic switching experiments but adjusted to better fit our results [97]. First, the polarity-averaged data set is calculated and reduced to the three repeats after training to remove any polarity-dependent components. Then, the remaining switching trace is separated into different regimes: the pulsing regime, i.e. pulsing along either the red or blue pulse lines (cf. Fig. 4.4 b)), and the relaxation regime. Thus, each regime can be fitted with an appropriate function separately. This is exemplarily shown in Fig. 4.11, where the pulsing regime (pulsing along red pulse line) and the relaxation regime have both been fitted with corresponding functions for further analysis.

For the pulsing regime, a simple phenomenological fit function consisting of a constant, an exponential function and a line was found to be appropriate. In this case, the variable is the burst count b:

$$R_{\mathrm{p}}(b) = c_0 + c_1 \exp\left(-\frac{b}{\mu}\right) + c_2\, b. \tag{4.12}$$

$c_{0,1,2}$ and μ are the fitting parameters. Note that Eq. 4.12 is only a phenomenological fit function with no further physical interpretation. It is just used to obtain the switching efficiency of the first burst R_{e} accurately by taking the derivative at $b = 0$:

$$R_{\mathrm{e}} = \left|\frac{dR_{\mathrm{p}}(b)}{db}\right|_{b=0} = \left|-\frac{c_1}{\mu} + c_2\right|. \tag{4.13}$$

In addition to the fitting procedure, we define the difference of $R_{\perp}$ before and after applying the bursts along one current line as the absolute switching amplitude $|\Delta R_{\mathrm{a}}|$, indicated in Fig. 4.11.

The relaxation regime is governed by the exponential relaxation of an independent ensemble of grains that have a broad range of relaxation times, which is usually modeled with a sum of two exponentials [97]. However, we found that using a stretched exponential decay, which is equivalent to a sum of exponentials [115], is more appropriate for our data set. Hence, the following functional expression, numerically more stable than the explicit sum of exponentials, was used:

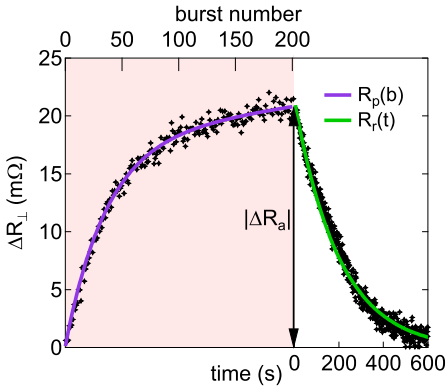

Figure 4.11: Exemplary fitting procedure for the pulsing (red background) and relaxing phase (white background).

$$R_{\mathrm{r}}(t) = k_0 + k_1 \exp\left(-\alpha\, t^{\beta}\right). \tag{4.14}$$

$k_{0,1}$, α and the streching exponent β are fitting parameters. The constant offset k_0 is added to allow for a non-relaxing contribution to the relaxation phase. The stretched relaxation time constant τ_s can then be derived from the fitting parameters via

$$\tau_\mathrm{s} = \left(\frac{1}{\alpha}\right)^{\frac{1}{\beta}}. \tag{4.15}$$

As shown in [97], the exponential decay during relaxation has a strict physical meaning. All antiferromagnetic grains of a polycrystalline film have volumes V_g which typically follow a log-normal distribution. As these grains are related to the anisotropy energy barriers via $E_\mathrm{B} = K_\mathrm{AF} V_\mathrm{g}$ [69], the corresponding relaxation time for the orientation of the Néel vector of a grain is given by the Néel-Arrhenius equation:

$$\tau = f_0^{-1} \exp\left(\frac{E_\mathrm{B}}{k_\mathrm{B} T}\right). \tag{4.16}$$

Here, $f_0 \approx 10^{12}\,\mathrm{s}^{-1}$ is the attempt frequency [69], k_B is the Boltzmann constant, and T is the absolute temperature. We note that f_0 does explicitly depend on the material parameters (including E_B) and the temperature [116]. However, for practical purposes the exponential dependence on the Boltzmann factor dominates, so to obtain a reasonable estimate of E_B, it is safe to treat f_0 as a constant. During the pulsing, grains with various energy barriers are excited at the same time, where smaller E_B means that the Néel vector is easier to switch but will also relax faster. This weighted sum is reflected by the stretched exponential, where the stretching parameter β is related to the probability distribution of the grains. Reconstructing the underlying probability distribution requires an inverse Laplace transform of the measured data and is impractical [115]. Therefore, only the mean time constant $\langle\tau\rangle$ is considered for further analysis, calculated via

$$\langle\tau\rangle = \frac{\tau_\mathrm{s}}{\beta}\,\Gamma\left(\frac{1}{\beta}\right), \tag{4.17}$$

where $\Gamma(x)$ denotes the gamma function.

4.4.4 Dependence on temperature

To investigate the temperature dependence of the spin current induced switching of MnN, switching traces were measured over a broad temperature range for the samples with 6 nm and 9 nm MnN. In Fig. 4.12, the corresponding polarity-averaged switching traces, all measured with a current density of

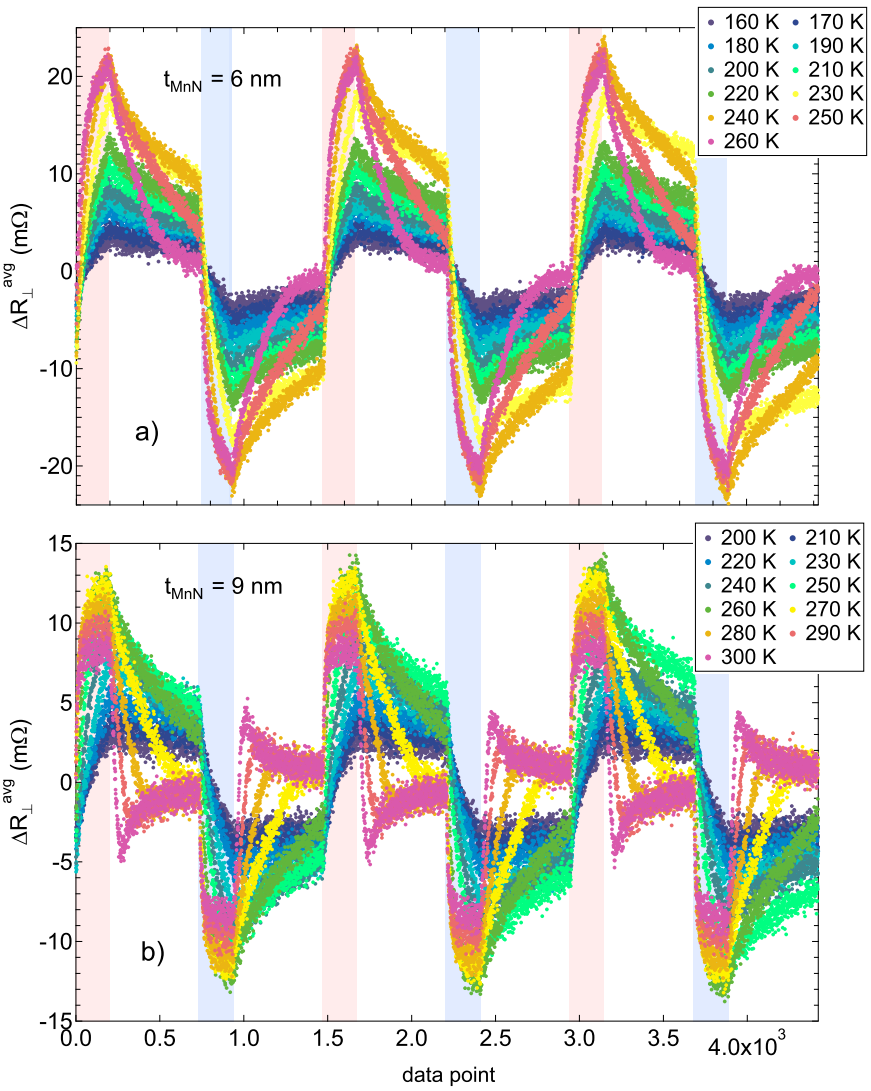

Figure 4.12: Temperature dependent switching traces of the a) 6 nm MnN and b) 9 nm MnN sample taken at a current density of $j_{\mathrm{Pt}} = 8.45 \times 10^{11}\,\mathrm{A/m^2}$.

$j_{\mathrm{Pt}} = 8.45 \times 10^{11}\,\mathrm{A/m^2}$, are shown for both samples. The results of the 6 nm MnN sample, displayed in Fig. 4.12 a), clearly show that higher temperature assists the switching process, with increasing steepness and amplitude. It is also clearly seen that with higher temperature, the relaxation becomes much faster and complete relaxation to the initial state is seen after 600 s at 260 K.

For the 9 nm MnN sample (Fig. 4.12 b)) the switching traces, especially the ones taken at high temperature, look somewhat complicated at first sight. Here, relaxation to the initial state is observed after 600 s at 270 K. When going to higher temperatures, another contribution to the relaxation arises. This contribution is of opposite sign and occurs after the initial state has been reached within the relaxation time window of 600 s. This is most prominently visible at a temperature of 300 K, where the system almost immediately relaxes to its initial state after pulsing but then evolves to more negative or positive values, correspondingly. A clear second relaxation back to the initial state follows. This behavior suggests an underlying additional switching mechanism, probably induced by resistive contributions, that occurs at high temperatures but requires further investigations to be fully understood.

In Fig. 4.13, the results of the quantitative analysis for these temperature dependent measurements are summarized. The absolute switching amplitude shows clear maxima for both film thicknesses as a function of the temperature (Fig. 4.13 a)). Remarkably, the thinner film shows a larger amplitude and the maximum is found at lower temperature. Simultaneously, the switching efficiency (Fig. 4.13 b)) increases with increasing temperature, but also shows an indication of peaking at a slightly higher temperature as compared to the amplitude. $\langle\tau\rangle$ shows a very strong temperature dependence in both samples and is smaller for the 6 nm MnN film thickness, see Fig. 4.13 c).

These results are fully compatible with the thermal-activation model developed earlier for NSOT switching in Mn_2Au and CuMnAs [21, 97]. The larger film thickness leads to a larger grain volume and thereby shifts the switching amplitude maximum to slightly higher temperature for the 9 nm MnN sample. However, as the spin current induced switching is mainly an interface effect, the absolute amplitude is overall smaller in the thicker sample.

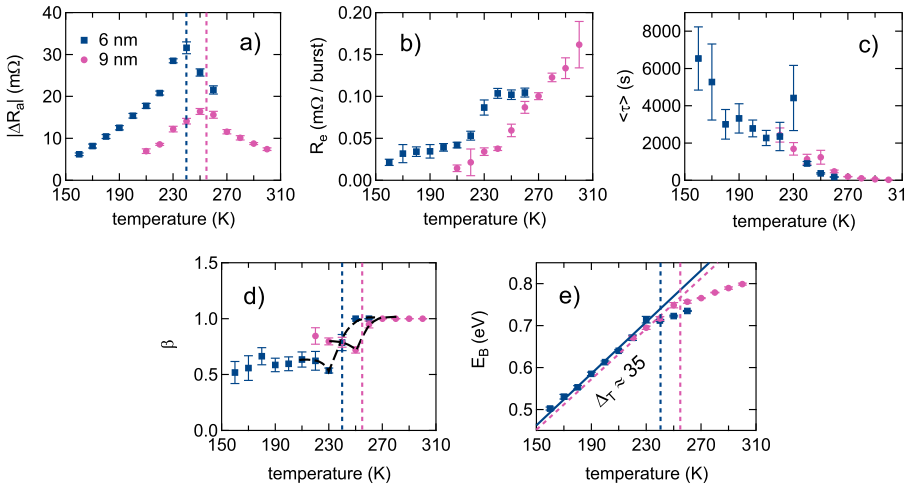

Figure 4.13: Temperature dependent parameters for the 6 nm and 9 nm MnN samples. a) Absolute switching amplitude $|\Delta R_\mathrm{a}|$, b) Switching efficiency R_e, c) Mean relaxation time constant $\langle\tau\rangle$, d) Streching exponent β (dashed lines as guide to the eye), and e) Switching energy barrier E_B. The measurements were performed with a current density of $j_\mathrm{Pt} = 8.45 \times 10^{11}\,\mathrm{A/m^2}$. All parameters represent the weighted average calculated from several repeats. The error bars mark the corresponding standard deviation.

Simultaneously, higher temperatures lead to a faster relaxation, as given by the Néel-Arrhenius equation [69]. As can be seen in Fig. 4.13 d), the stretching exponent β approaches unity with increasing temperature in both samples, but $\beta = 1$ is reached at lower temperatures in the thinner film. Notably, β shows a fairly sharp transition as it approaches unity, and this transition is observed at the same temperatures where also $|\Delta R_\mathrm{a}|$ peaks (see vertical dashed lines in Fig 4.13). This fact deserves closer attention and will be further discussed below. The energy barriers obtained from the relaxations are of the order $E_\mathrm{B} = 0.5 \ldots 0.8\,\mathrm{eV}$, see Fig. 4.13 e). In contrast to the naive expectation of scaling with film thickness, very similar energy barriers are observed for both samples. Notably, both films have mean relaxation time constants of less than 100 s at room temperature. This is in line with the observation that exchange bias is generated with MnN only for film thicknesses larger than $t_\mathrm{MnN} = 10\,\mathrm{nm}$ [31] at room temperature.

4.4.5 Dependence on current density

Next, the dependence of the switching on the current density was investigated for the 6 nm sample at a fixed temperature of 230 K. In Fig. 4.14, the corresponding switching traces for current densities ranging from $j_{\mathrm{Pt}} = 7.61 - 9.63 \times 10^{11}\,\mathrm{A/m^2}$ are displayed. Obviously, similar to increasing temperature, higher current densities assist the switching in terms of amplitude and steepness. The switching is quite sensitive to the current density as large changes of the amplitude are seen within a fairly small interval of current densities. However, an influence on the relaxation is not clearly visible.

The results of the quantitative analysis confirm that both the switching amplitude and the switching efficiency are greatly increased with increasing current density. This is shown in Fig. 4.15 a) and b), respectively. In contrast to the vague observation in Fig. 4.14, fitting the relaxation of the switching traces yields a clear dependence of $\langle\tau\rangle$ (Fig. 4.15 c)) and β (Fig. 4.15 d)) on the current density. This might seem surprising at first sight but is caused by the fact that at higher current density, the film temperature is substantially

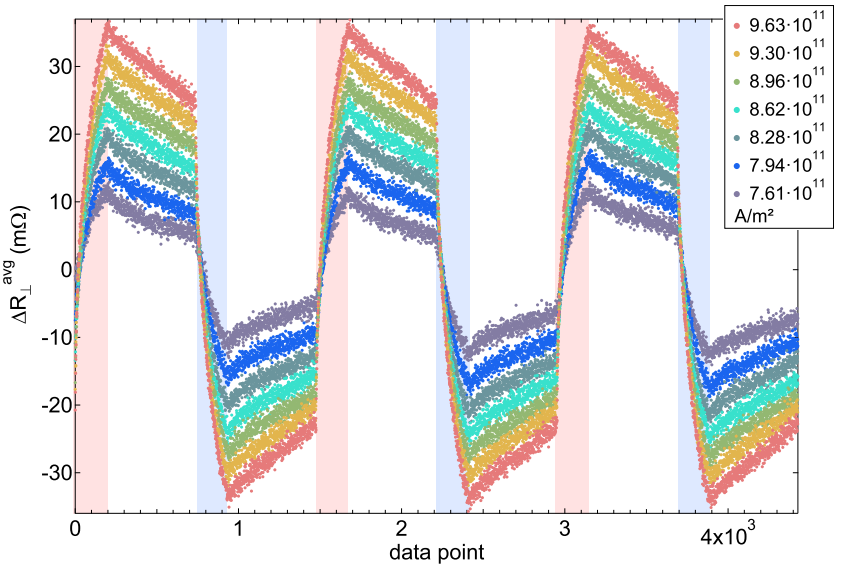

Figure 4.14: Switching traces of the 6 nm MnN sample taken at 230 K for center-region Pt current densities of $j_{\mathrm{Pt}} = 7.61 - 9.63 \times 10^{11}\,\mathrm{A/m^2}$.

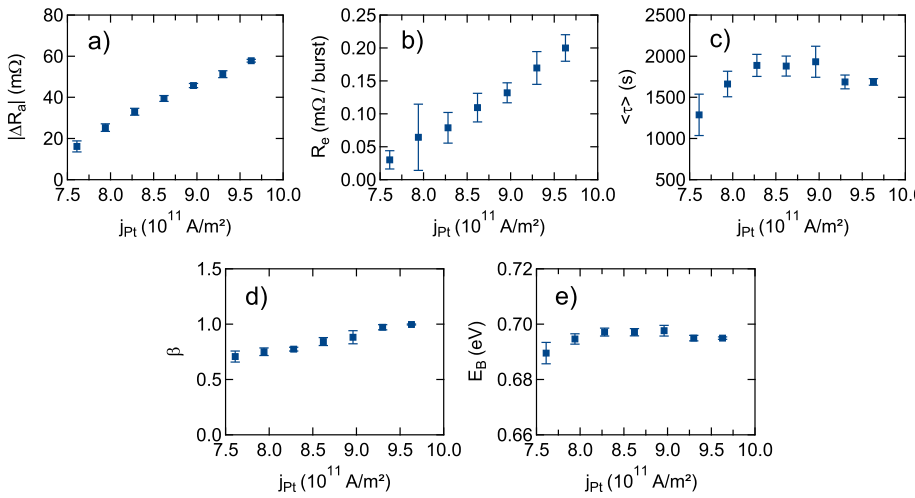

Figure 4.15: Switching parameters in dependence on the current density for the 9 nm MnN sample. a) Absolute switching amplitude $|\Delta R_\mathrm{a}|$, b) Switching efficiency R_e, c) Mean relaxation time constant $\langle\tau\rangle$, d) Streching exponent β, and e) Switching energy barrier E_B. The measurements were performed at $T = 230\,\mathrm{K}$. The Pt current densities are given for the center-region of the star structure. All parameters represent the weighted average calculated from several repeats. The error bars mark the corresponding standard deviation.

higher, which increases the proportion of larger grains with larger energy barriers that participate in the switching (Fig. 4.15 e)). The observed $\langle\tau\rangle$ increases as these grains contribute to a slower relaxation at the measurement temperature. Simultaneously, β approaches unity, which can be interpreted again as the lack of larger grains to activate by additional temperature.

4.4.6 Particle size and ensemble analysis

In the previous sections of this Chapter, the grain size distribution of MnN and its influence on the SOT switching has been frequently mentioned. Now, this relation will be discussed in more detail. Fig. 4.16 a) shows a reproduction of the results of the particle diameter analysis on MnN from [73]. Here, polycrystalline MnN films similar to the ones used in the switching experiments were studied. According to this analysis, the anisotropy energy density is $K_\mathrm{AF} \lessapprox 4 \times 10^5\,\mathrm{J/m^3}$ for thin MnN films. For log-normal distributed grain

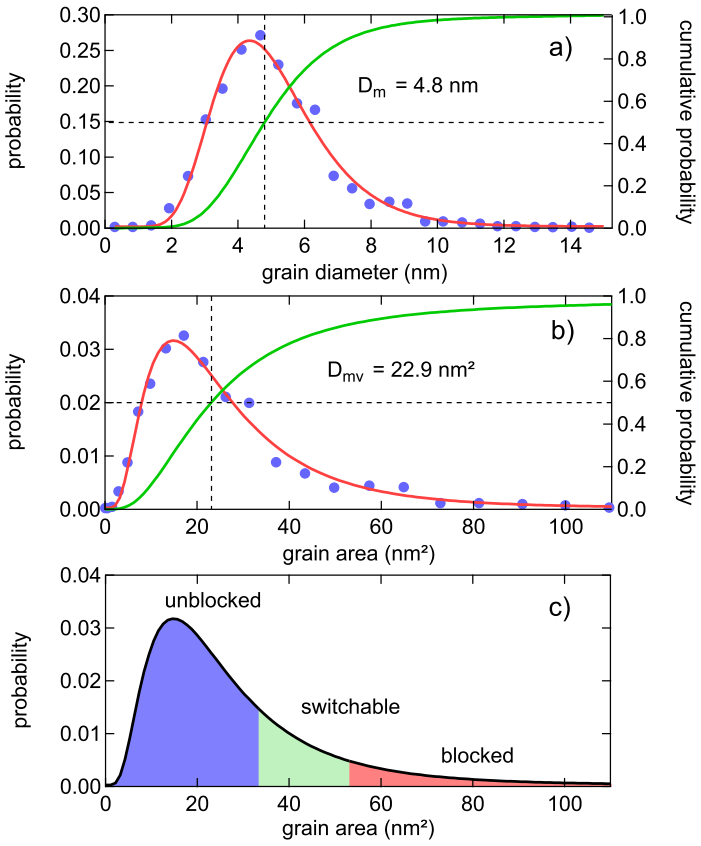

Figure 4.16: a) Particle diameter analysis from a plan view TEM image. Data points taken from [73]. The integrated log-normal fit (i.e., the cumulative probability) indicates a median grain diameter of $D_\mathrm{m} = 4.8\,\mathrm{nm}$. b) Particle size analysis recalculated for the grain area under the assumption of cylindrical grains. The log-normal fit indicates a median volume-derived grain area of $D_\mathrm{mv} = 22.9\,\mathrm{nm}^2$. c) Model of the three grain-size regimes discussed in the main text. The three grain categories are drawn for the case of an MnN thickness of 6 nm.

diameters, also the grain areas and grain volumes of cylindrical grains are log-normal distributed. Hence, the cross-sectional area of grains which correspond to the median volume is $D_\mathrm{mv} \approx 22.9\,\mathrm{nm}^2$, as can be seen in Fig. 4.16 b). This corresponds to an energy barrier of $E_\mathrm{B} = 0.35\,\mathrm{eV}$ in the 6 nm MnN film, which is clearly of the correct order of magnitude compared to the values derived from the switching characteristics.

However, this result indicates that the grains which contribute to the switching in our experiments are larger than the median of the distribution. The beginning saturation of E_B as a function of temperature in Fig. 4.16 e) can thus be understood as a lack of grains with diameters larger than 7.5 nm ($E_B \approx 0.7$ eV for the 6 nm film). Indeed, according to the particle size analysis, less than 10 % of the grains have larger diameters. Therefore, their contribution to the electrical signal will be rather small. This interpretation is additionally supported by the convergence of two more characteristics: The peak in $|\Delta R_a|$ and the transition to $\beta = 1$ at the very same temperatures (dashed vertical lines in Fig. 4.13). The peak in $|\Delta R_a|$ originates from the lack of larger grains, such that the number of grains contributing to the signal goes to zero as the temperature is further increased. Meanwhile, $\beta \to 1$ means that the decay is described by a single exponential, i.e. the width of active part of the grain size distribution becomes smaller. This is trivial, once the maximum grain size in the system is reached and no larger grains are present anymore to be activated by higher temperatures.

These results allow for the identification of three classes of grains, which we call *unblocked*, *switchable*, and *blocked*. These classes are indicated accordingly for the corresponding temperature regimes in Fig. 4.16 c). The unblocked grains relax very quickly for all temperatures at which the measurements were performed. The switchable grains correspond to the observed energy barriers of 0.5...0.7 eV for the 6 nm MnN film. Finally, the blocked grains remain blocked and are not switched with the SOT. It should be noted that only a narrow part of the switchable ensemble will contribute to the actual switching and relaxation at any given temperature. Correspondingly, one cannot directly relate the position of the switching amplitude maximum to the maximum of the grain size distribution, due to the complexity of the switching and relaxation dynamics. As a result of the Joule heating during the pulsing, the switching occurs at an elevated temperature, whereas the relaxation happens at the set measurement temperature.

4.4.7 Influence of Joule heating

To shed further light on the Joule heating and the effect of the conducting multilayer system and associated shunting, the sample stack is studied with the parallel resistor model, as introduced in Chapter 4.2. The corresponding results are presented in Fig. 4.17.

The model yields very similar Pt resistivities for the two samples (Fig. 4.17 a)), slight deviations probably arise from the neglect of the weak temperature dependence of the MnN and Ta resistivities. Because of the identical nominal current densities j_0, the sample with 9 nm MnN has a larger center-region current density in the Pt layer, cf. Fig. 4.17 b). On the basis of the resistivities and the center-region current densities, the associated spin Hall angles

$$\theta_{\mathrm{SH}} = \sigma_{\mathrm{SH}} \rho_{\mathrm{Pt}}, \tag{4.18}$$

with $\sigma_{\mathrm{SH}} = 4 \times 10^5\,(\Omega\mathrm{m})^{-1}$ [117] (Fig. 4.17 c)) and spin current densities

$$j_{\mathrm{s}} = \theta_{\mathrm{SH}} j_{\mathrm{Pt}} \tag{4.19}$$

(Fig. 4.17 d)) are calculated. The spin current density from the Ta film is neglected, since the current density flowing in the Pt layer is approximately eight times higher due to its lower resistivity. Because of the larger film thickness, the Joule heating power density

$$P_{\mathrm{MnN}} = \rho_{\mathrm{MnN}} d_{\mathrm{MnN}} j_{\mathrm{MnN}}^2 \tag{4.20}$$

is larger in the 9 nm MnN sample (Fig. 4.17 e)). Using the heating powers of the center-region of the star structures, the peak temperatures of the MnN film can be calculated using an analytical formula derived by You et al. [97, 118]:

$$\delta T(t) = \frac{w d_{\mathrm{MnN}} \rho_{\mathrm{MnN}} j_{\mathrm{MnN}}^2}{\pi \kappa_{\mathrm{s}}} \cdot \left[\mathrm{arcsinh}\left(\frac{2\sqrt{\mu_{\mathrm{s}} t}}{\alpha w} \right) - \theta(t - \Delta t) \mathrm{arcsinh}\left(\frac{2\sqrt{\mu_{\mathrm{s}}(t - \Delta t)}}{\alpha w} \right) \right]. \tag{4.21}$$

Here, w denotes the current line width, κ_s the heat capacity of the substrate and μ_s the thermal diffusivity. As suggested by You et al. [118], α was set to 0.5. Furthermore, a correction factor of 1.48 determined by a stationary finite-element simulation was applied to take the 50 nm SiO_2 layer into account. Unsurprisingly, at identical measurement temperature, the MnN film reaches a higher temperature due to the Joule heating with larger film thickness.

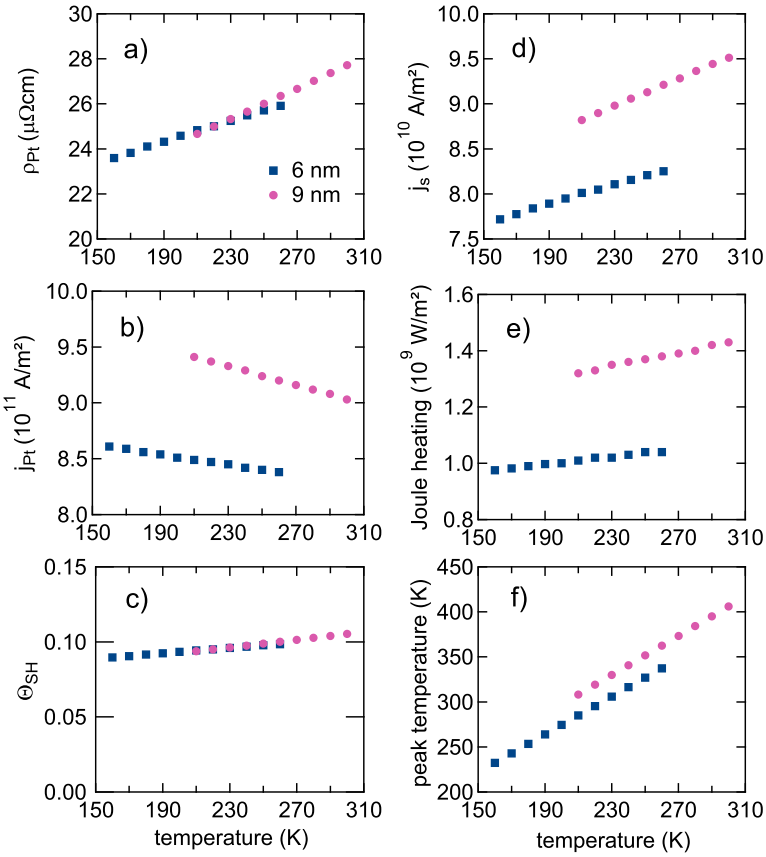

Figure 4.17: Temperature dependencies for the 6 nm and the 9 nm MnN sample of a) Resistivity of the Pt layer, b) Pulse current density in the center-region of the Pt layer at an initial current density of $j_0 = 5 \times 10^{11}\,\mathrm{A/m^2}$, c) Calculated spin Hall angle, d) Calculated spin current density, e) Calculated Joule heating power, and f) Calculated peak temperature during the pulses. Note that all Pt current densities are given for the center-region of the star-structure.

With these results in mind, one can take a more detailed look on the similarity of E_B for different MnN film thicknesses as seen in Fig. 4.13 e). Both the thermal activation and the spin current density are larger in the thicker MnN film, yielding a more efficient switching in this sample. This brings the two thicknesses closer together in terms of efficiency. However, E_B is evaluated from the relaxation, which depends only weakly on how the state has been set (cf. Fig. 4.15 c)). Both temperature dependencies of E_B in Fig. 4.13 e) can be fitted with identical line fits $E_\mathrm{B} = \Delta_T k_\mathrm{B} T$ with $\Delta_T \approx 35$ in the range up to 240 K, while saturation is seen at higher temperatures. This can be interpreted as a grain-selection process by the available torque. Only grains with $\Delta_T \approx 27 \ldots 44$ can be switched and be observed to relax [97]. Since the available torque is similar for all film thicknesses, in the thicker film grains with smaller diameter contribute to the switching at a given temperature as compared to a thinner film. Eventually, the energy barrier that is overcome is the same in the different films. This means that electrical switching may be observable in many antiferromagnets just below or at the onset of exchange bias, which can be taken as a simple measure for the thermal stability and the associated switching energy barrier.

4.5 Read-out mechanism

Up to this point, it has not been discussed how the reorientation of magnetic moments in the MnN layer yields a change of the transverse resistance $R_{\perp}$ that is measured perpendicular to the probe current. There are two possible mechanisms that can contribute to the transverse resistance change, either the planar Hall effect (PHE) or the spin Hall magnetoresistance (SMR), which will both be shortly introduced in the following.

The PHE, the transverse component of the anisotropic magnetoresistance (AMR), is a well-known tool for detecting the rotation of magnetic moments in ferromagnets [98]. A current flowing through a ferromagnetic film varies in dependence on the angular orientation towards the sample's magnetization. A few years ago, it has been demonstrated that the AMR also occurs in antiferromagnets, where it can be used to extract information about the Néel order [23, 119]. Here, a current $\vec{J}$ flowing through the sample varies with respect to the orientation of the antiferromagnet's Néel vector $\vec{L}$. The resulting dependence of the sample's resistivity on the angle α between the current and the Néel vector originates from relativistic spin-orbit interactions and spin-dependent scattering mechanisms, further discussed in the introduction of this Chapter and in [23, 98].

In a typical measurement, this effect is detected as a change in resistivity ρ either in a longitudinal or transverse geometry as illustrated in Fig. 4.18 [120]. When measuring the resistivity in a longitudinal orientation, parallel to the

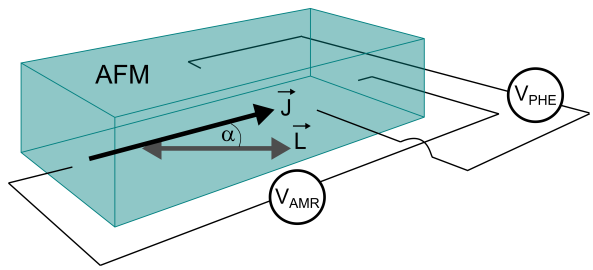

Figure 4.18: Schematic illustration of the measurement geometry for the AMR and the PHE in an antiferromagnet (AFM). The measured voltage is dependent on the angle α between the current $\vec{J}$ and the Néel vector $\vec{L}$.

applied current, the AMR is observed. Its angular dependence is described by

$$\rho_{\mathrm{AMR}} = \rho_{\mathrm{perpendicular}} + \Delta\rho \cos^2(\alpha), \tag{4.22}$$

where $\Delta\rho$ denotes the difference between the resistivity in the parallel and perpendicular configuration of the current and the Néel vector [120]. The PHE is observed in a transverse measurement geometry. Here, the angular dependence is given by

$$\rho_{\mathrm{PHE}} = \frac{\Delta\rho}{2} \sin(2\alpha). \tag{4.23}$$

In our switching experiments, the Néel order of the MnN layer, i.e. the single antiferromagnetic grains, is slightly rotated with each current pulse. Thus, by measuring the voltage (and resistance) perpendicular to a probe current flowing through the MnN layer, the PHE can be observed. Note that this effect arises solely from the antiferromagnetic layer and only occurs in conducting materials. Hence, in previous studies on antiferromagnetic switching with insulating NiO [20], it would not contribute to the transverse resistance $R_{\perp}$ and thus the read-out mechanism.

In contrast to the PHE, the SMR originates not from the magnetic layer but the adjacent heavy metal (NM) layer that generates the spin current for the switching, i.e. the Pt layer in our samples. As the mechanism of the SMR in antiferromagnets is not yet fully understood, Fig. 4.19 schematically illustrates how the SMR is induced in ferromagnets (FM), yielding a magnetization dependent transverse resistance $R_{\perp}$ [121]. A more detailed theoretical description of the SMR can be found in [122].

When a current J is applied to the heavy metal layer, a perpendicular spin current $\vec{J}_{\mathrm{s}}$ is generated due to the SHE. Dependent on the orientation of the magnetization in the adjacent ferromagnetic layer, this spin current is reflected at the interface or transfers its momentum to the magnetic moments of the ferromagnet. In case the magnetization and the spin of the electron that travels towards the interface are parallel (Fig 4.19a)), the electron is reflected and moves back towards the charge current due to the inverse SHE. However, if the electron's spin and the magnetization are not aligned parallel

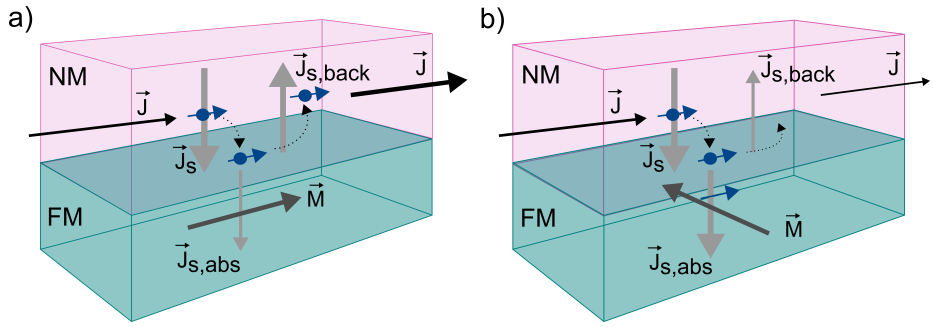

Figure 4.19: Simplified illustration of the mechanism that causes the SMR. A current $\vec{J}$ induces a spin current $\vec{J}_s$ in the non-magnetic heavy metal (NM) layer. a) If the electrons' spins that travel towards the NM/ FM interface are aligned parallel to the ferromagnet's (FM) magnetization, a significant spin current $\vec{J}_{s,\,back}$ directs them back to the charge current. b) For other orientations between the electrons' spins and the magnetization, momentum is transferred to the magnetic moments in the ferromagnet and only a small spin current $\vec{J}_{s,\,back}$ arises.

(Fig 4.19b)), angular momentum can be transferred to the magnetic moments in the ferromagnet via SOT. As a result, the electron has a higher probability of being absorbed by the ferromagnet, yielding a higher longitudinal and transverse resisistivity. The increase in resistivity is most pronounced for a perpendicular orientation of the electron's spin and the magnetization [121].

As discussed in Chapter 4.1.3, the interaction of spin currents with a corresponding spin polarization and the Néel order in antiferromagnets can be determined by two different mechanism. Possibly depending on the antiferromagnet's spin diffusion length, the Néel vector is favored to align parallel or perpendicular to the spin polarization. Thus, also the SMR in antiferromagnets might be influenced by the spin diffusion length. Depending on the dominant mechanism, the SMR would be maximum for a perpendicular or parallel initial orientation of Néel vector and incoming spin polarization. As it is not clear which switching mechanism is most prominent in our samples, we cannot be sure of the geometries of the resulting SMR. Nevertheless, is is definitively a second possible read-out mechanism contributing to the transverse resistance $R_\perp$ observed in our transport measurements.

To get a better understanding about the read-out mechanism that is dominant in our samples, the relative transverse resistivity $\rho_\perp/\rho$ is calculated for both possible read-out cases, simply using the maximum switching amplitudes $|\Delta R_\mathrm{a}|$. Depending on the mechanism, the transverse voltages can be written as follows:

$$U_{\perp,\mathrm{PHE}} = \rho_\perp I_\mathrm{MnN}/d_\mathrm{MnN}\ \text{(PHE)}\quad\text{and}\quad U_{\perp,\mathrm{SMR}} = \rho_\perp I_\mathrm{Pt}/d_\mathrm{Pt}\ \text{(SMR)}. \tag{4.24}$$

For the sample with 9 nm MnN this yields $(\rho_\perp/\rho_\mathrm{MnN})_\mathrm{PHE} \approx 2\times10^{-4}$ in the PHE case. Accordingly, for the SMR originating in the Pt layer the ratio is $(\rho_\perp/\rho_\mathrm{Pt})_\mathrm{SMR} \approx 0.9\times10^{-4}$. The current branching ratio is approximately $I_\mathrm{Pt}/I_\mathrm{MnN} \approx 7.3$. Both numbers are fairly small compared to previous antiferromagnetic switching experiments on Mn_2Au (maximum $\rho_\perp/\rho \approx 70\times10^{-4}$) and CuMnAs (maximum $\rho_\perp/\rho \approx 14\times10^{-4}$) [21, 97], where the PHE is the only possible read-out mechanism. However, they are similar to the SMR amplitude in Pt/ NiO upon rotation in a strong magnetic field (maximum $\rho_\perp/\rho \approx 2\times10^{-4}$ at room temperature) [20, 123]. On the other hand, the SMR can be much larger (maximum $\rho_\perp/\rho \approx 16\times10^{-4}$ at room temperature) in YIG/ Pt films [124].

Additionally, density functional theory calculations of antiferromagnetic MnN with the fully relativistic multiple-scattering Green function framework as implemented in the SPR-KKR program were performed by Markus Meinert [125, 126]. The resistivity tensor was calculated via the Kubo-Bastin formalism at a finite temperature of 300 K, determining the PHE amplitude. Lattice vibrations were treated in the alloy analogy model using the coherent potential approximation [127, 85].

The mean resistivity was found to be $\mathrm{Tr}(\rho) \approx 57.7\,\mu\Omega\mathrm{cm}$, which is much smaller than the observed value, but still rather high for a metal. The larger resistivity of the thin films arises from the small grain diameter and additional scattering in the grain boundaries. The PHE amplitude is $\rho_\perp/\rho \approx 5.4\times10^{-4}$ in case the Néel vector $\vec{L} \parallel [100]$ of the face-centered tetragonal unit cell depicted in Fig. 1.1. In contrast, with $\vec{L} \parallel [110]$ the amplitude yields $\rho_\perp/\rho \approx -1.7\times10^{-4}$. This result indicates that the PHE and the SMR are of similar magnitude in

the Pt/ MnN system and both may contribute to the signal. However, the theoretical PHE amplitude appears somewhat too small, given that only a small fraction of the film contributes to the observed signal. It is only a factor of 2.5 smaller than the theoretical result, which should be observed when the Néel states of all grains are aligned along the [100] direction. However, the calculation might underestimate the PHE, as neither chemical disorder nor grain boundary and surface effects are explicitly modeled. Apart from that, thermomagnetic effects such as the spin Seebeck effect should not contribute to the signal. In our transport measurements, a lock-in technique is used and the first harmonic signal is measured, whereas thermomagnetic effects would be seen on the DC and the second harmonic components. Concluding these considerations it gets clear that without knowing the dominating read-out mechanism and its sign, it is not possible to assess whether the Néel vector is switched parallel to the current direction (as suggested in [20]) or perpendicular (as derived for NiO in [25]). To gain further insight into this open question, a detailed study of the magnetoresistance in strong magnetic fields is necessary and has yet to be performed.

Chapter 5

Conclusion

In the course of this work, the rare-earth free antiferromagnet MnN was studied regarding its use in polycrystalline exchange bias systems as well as in SOT induced electrical switching experiments. In the following, the main results of these investigations are briefly summarized. Additionally, it is discussed which further experiments with MnN need to be performed to better understand some of its properties and what the chances of integrating MnN in spintronic devices in the near future are.

Studying Ta/ MnN/ CoFe exchange bias systems, we found that enhanced exchange bias is observed for samples with $t_{\mathrm{MnN}} \geq 36\,\mathrm{nm}$ after annealing at $T_{\mathrm{A}} > 400^{\circ}\,\mathrm{C}$. This way, maximum exchange bias of more than 2500 Oe could be achieved, accompanied by an increased blocking temperature. The highest value of $H_{\mathrm{eb}} = 2750\,\mathrm{Oe}$ was found for the sample with 48 nm MnN after annealing at $T_{\mathrm{A}} > 525^{\circ}\,\mathrm{C}$. Via AES and PNR measurements it was confirmed that strong nitrogen diffusion into the Ta buffer layer occurs during the annealing processes. The Ta layer is completely saturated with nitrogen after the last annealing step. However, samples with thick MnN ($t_{\mathrm{MnN}} = 42, 48\,\mathrm{nm}$) films are not that severely influenced by the resulting nitrogen deficiency since they have a large nitrogen reservoir, allowing for the generation of exchange bias even after annealing at temperatures higher than $T_{\mathrm{A}} = 500^{\circ}\,\mathrm{C}$. Concluding this, there seems to be a clear relation between thermal stability of Ta/ MnN/ CoFe exchange bias systems and the thickness of the MnN layer. With increasing thickness, exchange bias becomes more robust after annealing

at high temperatures. The giant increase of exchange bias for the samples with thicker MnN films might be connected to crystallographic or magnetic modifications that are induced during annealing.

Following the AES and PNR results suggesting strong nitrogen diffusion into the Ta seed layer during annealing, the focus of a second study concerning exchange bias and thermal stability in Ta/ MnN/ CoFeB systems was laid on the role of the buffer layer. Therefor, the influence of the Ta layer's thickness on exchange bias throughout a large annealing temperature range was studied. Our findings show that even though thinner Ta layers provide a smaller nitrogen drain, which might be beneficial for the thermal stability of the system, MnN's crystallinity worsens with decreasing Ta thickness. This causes lower total exchange bias values. Similar results were found when introducing a TaN_x diffusion barrier. While this modification could promote better thermal stability, it mostly yields low exchange bias values as the crystallinity of MnN is affected negatively when growing on TaN_x. Overall, our results show that the Ta buffer layer plays an active role in determining the exchange bias in the Ta/ MnN/ CoFeB system. It acts as a crystallographic seed layer for better growth of MnN and as an active nitrogen drain during the annealing process. Both these qualities are crucial for the generation of high exchange bias. Concluding this, the main findings of these investigations are that at least 10 nm Ta are needed as a buffer layer to generate high exchange bias and that the introduction of a diffusion barrier is not useful. Moreover, the diffusion processes and possible magnetic and structural transitions of MnN that happen during annealing, especially at high temperatures, are more complicated than expected and need further investigation for a comprehensive understanding.

To study whether MnN can act as an active component in spintronic devices, we investigated spin current driven SOT switching in Ta/ MnN/ Pt stacks. Via electrical transport measurements, reproducible and polarity-independent switching of the Néel order in MnN could be observed for current densities higher than $j_{Pt} \approx 7.5 \times 10^{11}\,\mathrm{J/m^2}$. The read-out was performed in a planar Hall geometry, however we cannot yet confirm whether the PHE or SMR is the dominating mechanism. Several current density cycles were performed in

order to rule out resistive contributions to the switching, confirming that those contributions only arise for high current density values of $j_{\mathrm{Pt}} \gtrsim 11 \times 10^{11}\,\mathrm{A/m^2}$. Hence, we are sure that the switching observed in our samples is of magnetic origin. Temperature and current density dependent measurements on samples with different MnN thickness confirmed that the observed characteristics are fully compatible with a thermal activation model. These results demonstrate that the characteristic switching properties observed in epitaxial Mn_2Au, CuMnAs, or NiO films can also be obtained in much simpler, polycrystalline antiferromagnetic films. Manipulation of the Néel order should thus, in principle, be possible in any polycrystalline antiferromagnet.

All in all, MnN has proven to be a very promising material for future application in spintronic devices. As a passive component, it can possibly be used to generate very high exchange bias for GMR or TMR spin valves. Furthermore, MnN functions in SOT induced switching experiments, enabling its use as an active and accessible antiferromagnet for spintronics. However, even though MnN surpasses a lot of other commonly used antiferromagnets in terms of availability, easy producibility and promising performance, there are still several properties that need to be better understood and investigated.

Most importantly, for both its use in exchange bias as well as in switching experiments, it would be extremely beneficial to know the magnetic orientation the polycrystalline MnN films grow in. Even though the x-ray diffraction results suggest a growth in (001) direction, it is not clear whether the films grow with the c or the a axis perpendicular to the sample plane. Consequently, depending on this orientation of the lattice, the magnetic moments could be either parallel, tilted, or perpendicular to the plane. Possibly, during annealing a transition between those states is induced, resulting in the dip in exchange bias observed around $T_{\mathrm{A}} \approx 250^{\circ}\,\mathrm{C}$. To clarify this, neutron diffraction measurements would be necessary. However, up to now, the investigation of thin films using this technique is close to impossible. Nevertheless, a study of the AMR in MnN in strong magnetic fields would be a first important step towards the understanding of the orientation of the Néel vector of MnN. Therefor, MnN's spin flop field has to be in the accessible range for laboratory magnetic fields. If possible, this would provide information to determine the

dominant read-out mechanism in the switching experiments as well as the direction the Néel vector is switched to with respect to the current direction. Being able to answer the latter would be a crucial contribution to the ongoing discussion about under which conditions SOT induced switching yields a parallel or antiparallel orientation of the Néel vector to the current direction.

Another important step towards the applicability of MnN would be a better understanding about the nitrogen diffusion processes happening during annealing. This is not only crucial for its use in exchange bias systems, but would also be beneficial for the switching experiments. Even though the samples do not need to be annealed here, high current densities and possibly high device operation temperatures might also induce irreversible changes due to nitrogen diffusion. We already found that nitrogen diffusion is highly correlated with thermal stability, being increased when using thick MnN films with a large nitrogen reservoir.

Even though AES and PNR studies already provided an extremely useful insight into the diffusion characteristics, it is still not clear how diffusion influences the crystal and magnetic structure on an atomic level. Therefore, detailed transmission electron microscopy studies could be performed in the future. Ideally, TEM measurements would be performed after different annealing steps and for different sample setups to reveal the changes diffused nitrogen induces to the atomic structure. Possibly, those investigations could provide information concerning the structural transitions that were observed after high-temperature annealing for samples with thin Ta buffer layers.

At this point, it should also be noted that the unusually high thickness of MnN poses another challenge for the integration of MnN exchange bias systems into spintronic devices. About 30 nm MnN are required to generate high exchange bias, whereas other commonly used materials like MnIr only require 7 nm [72]. Even though the reduction of MnN's thickness was no goal of this work, it should be mentioned that further investigations need to be performed to overcome this problem for future application. This could be achieved by altering the grain size distribution of MnN such that the anisotropy energy is increased, for instance by changing the deposition parameters or trying a

completely different preparation technique. With higher anisotropy energy, smaller minimum film thicknesses are necessary to induce exchange bias.

Despite those ongoing challenges, it can be concluded that it is quite probable that antiferromagnetic MnN will be used in future spintronic applications. It meets nearly all criteria for large-scale device integration and has proven to function reliably in exchange bias systems and SOT induced switching experiments, as shown in the course of this work. Our results present an important step on the route towards future spintronic devices based on rare-earth free and sustainable antiferromagnets.

Bibliography

[1] Moore, G. E. *Proceedings of the IEEE* **86**, 82 (1998).

[2] Chappert, C., Fert, A., and van Dau, F. N. *Nat. Mater.* **6**, 813 (2007).

[3] Žutić, I., Fabian, J., and Das Sarma, S. *Rev. Mod. Phys.* **76**, 323 (2004).

[4] Wolf, S., Awschalom, D., Buhrman, R., Daughton, J., von Molnár, v. S., Roukes, M., Chtchelkanova, A. Y., and Treger, D. *Science* **294**, 1488 (2001).

[5] Jullière, M. *Phys. Lett. A* **54**, 225 (1975).

[6] Baibich, M. N., Broto, J. M., Fert, A., Van Dau, F. N., Petroff, F., Etienne, P., Creuzet, G., Friederich, A., and Chazelas, J. *Phys. Rev. Lett.* **61**, 2472 (1988).

[7] Tsymbal, E. Y., Mryasov, O. N., and LeClair, P. R. *J. Phys. Condens. Matter* **15**, R109 (2003).

[8] Bhatti, S., Sbiaa, R., Hirohata, A., Ohno, H., Fukami, S., and Piramanayagam, S. *Mater. Today* **20**, 530 (2017).

[9] Liu, Y. and Yu, G. *Nat. Electron.* **2**(12), 555–556 (2019).

[10] Wadley, P., Howells, B., Železný, J., Andrews, C., Hills, V., Campion, R. P., Novák, V., Olejník, K., Maccherozzi, F., Dhesi, S. S., Martin, S. Y., Wagner, T., Wunderlich, J., Freimuth, F., Mokrousov, Y., Kuneš, J., Chauhan, J. S., Grzybowski, M. J., Rushforth, A. W., Edmonds, K. W., Gallagher, B. L., and Jungwirth, T. *Science* **351**, 587 (2016).

[11] Olejník, K., Schuler, V., Martí, X., Novák, V., Kašpar, Z., Wadley, P., Campion, R. P., Edmonds, K. W., Gallagher, B. L., Garcés, J., et al. *Nat. Commun.* **8**, 15434 (2017).

[12] Jungwirth, T., Marti, X., Wadley, P., and Wunderlich, J. *Nat. Nanotechnol.* **11**, 231 (2016).

[13] Jungwirth, T., Sinova, J., Manchon, A., Marti, X., Wunderlich, J., and Felser, C. *Nat. Phys.* **14**, 200 (2018).

[14] Baltz, V., Manchon, A., Tsoi, M., Moriyama, T., Ono, T., and Tserkovnyak, Y. *Rev. Mod. Phys.* **90**, 015005 (2018).

[15] Néel, M. L. *Ann. Phys. (Paris)* **12**, 137 (1948).

[16] Zabel, H., editor. *Magnetic heterostructures*, volume 227 of *Springer tracts in modern physics*. Springer, Berlin [u.a.] (2008).

[17] Néel, L. *Nobel Lectures in Physics 1963–1970*. Elsevier, Amsterdam (1972).

[18] Kools, J. C. S. *IEEE Trans. Magn.* **32**, 3165 (1996).

[19] Nogués, J. and Schuller, I. K. *J. Magn. Magn. Mater.* **192**, 203 (1999).

[20] Moriyama, T., Oda, K., Ohkochi, T., Kimata, M., and Ono, T. *Sci. Rep.* **8**, 14167 (2018).

[21] Meinert, M., Graulich, D., and Matalla-Wagner, T. *Phys. Rev. Appl.* **9**, 064040 (2018).

[22] Cheng, Y., Yu, S., Zhu, M., Hwang, J., and Yang, F. *Phys. Rev. Lett.* **124**, 027202 (2020).

[23] Shick, A. B., Khmelevskyi, S., Mryasov, O. N., Wunderlich, J., and Jungwirth, T. *Phys. Rev. B* **81**, 212409 (2010).

[24] Nakatsuji, S., Kiyohara, N., and Higo, T. *Nature* **527**, 212 (2015).

[25] Baldrati, L., Gomonay, O., Ross, A., Filianina, M., Lebrun, R., Ramos, R., Leveille, C., Fuhrmann, F., Forrest, T. R., Maccherozzi, F., Valencia, S., Kronast, F., Saitoh, E., Sinova, J., and Kläui, M. *Phys. Rev. Lett.* **123**, 177201 (2019).

[26] Fuke, H. N., Saito, K., Kamiguchi, Y., Iwasaki, H., and Sahashi, M. *J. Appl. Phys.* **81** (1997).

[27] Saito, M., Hasegawa, N., Watanabe, T., Kakihara, Y., Sato, K., Seki, H., Nakazawa, Y., Makino, A., and Kuriyama, T. In *Magnetics Conference, 1997. Digests of INTERMAG '97, IEEE International (1997).*

[28] *CRC handbook of chemistry and physics/94. 2013/14.* (2013).

[29] Glaister, B. J. and Mudd, G. M. *Minerals Engineering* **23**, 438 (2010).

[30] Hirohata, A., Huminiuc, T., Sinclair, J., Wu, H., Samiepour, M., Vallejo-Fernandez, G., O'Grady, K., Balluf, J., Meinert, M., Reiss, G., et al. *J. Phys. D Appl. Phys.* **50**, 443001 (2017).

[31] Meinert, M., Büker, B., Graulich, D., and Dunz, M. *Phys. Rev. B* **92**, 144408 (2015).

[32] Zilske, P., Graulich, D., Dunz, M., and Meinert, M. *Appl. Phys. Lett.* **110**, 192402 (2017).

[33] Dunz, M., Büker, B., and Meinert, M. *J. Appl. Phys.* **124**, 203902 (2018).

[34] Gokcen, N. *Bulletin of Alloy Phase Diagrams* **11**, 33 (1990).

[35] Leineweber, A., Niewa, R., Jacobs, H., and Kockelmann, W. *J. Mater. Chem.* **10**, 2827 (2000).

[36] Suzuki, K., Kaneko, T., Yoshida, H., Obi, Y., Fujimori, H., and Morita, H. *J. Alloys Compd.* **306**, 66 (2000).

[37] Mekata, M., Haruna, J., and Takaki, H. *J. Phys. Soc. Japan* **25**, 234 (1968).

[38] Yang, H., Al-Brithen, H., Trifan, E., Ingram, D. C., and Smith, A. R. *J. Appl. Phys.* **91**, 1053 (2002).

[39] Suzuki, K., Yamaguchi, Y., Kaneko, T., Yoshida, H., Obi, Y., Fujimori, H., and Morita, H. *J. Phys. Soc. Japan* **70**, 1084 (2001).

[40] Lambrecht, W. R., Prikhodko, M., and Miao, M. *Phys. Rev. B* **68**, 174411 (2003).

[41] Tabuchi, M., Takahashi, M., and Kanamaru, F. *J. Alloys Compd.* **210**, 143 (1994).

[42] Seshan, K. *Handbook of thin-film deposition processes and techniques: principles, methods, equipment and applications.* Noyes Publications/William Andrew Pub., Norwich, N.Y. (2002).

[43] Hölzle, R. H., editor. *Magnetische Schichtsysteme in Forschung und Anwendung: dieser Kurs wurde vom 1. bis 12. März 1999 im Forschungszentrum Jülich vom Institut für Festkörperforschung veranstaltet in Zusammenarbeit mit Universitäten und Forschungseinrichtungen*, volume 30 of *Vorlesungsmanuskripte des ... IFF-Ferienkurses; 30.* Forschungszentrum, Zentralbibliothek (1999).

[44] Swann, S. *Phys. Technol.* **19**, 67 (1988).

[45] Rossnagel, S. *Journal of Vacuum Science & Technology A: Vacuum, Surfaces, and Films* **21**, 74 (2003).

[46] Chapman, B. *Glow discharge processes.* Wiley, New York [u.a.] (1980).

[47] Wu, B. and Kumar, A. *Journal of Vacuum Science & Technology B: Microelectronics and Nanometer Structures Processing, Measurement, and Phenomena* **25**, 1743 (2007).

[48] Robinson, A. and Lawson, R. *Materials and Processes for Next Generation Lithography.* Elsevier, Amsterdam (2016).

[49] Hennessy, T. C. *Lithography: principles, processes, and materials.* New York: Nova Science (2011).

[50] Vieu, C., Carcenac, F., Pepin, A., Chen, Y., Mejias, M., Lebib, A., Manin-Ferlazzo, L., Couraud, L., and Launois, H. *Appl. Surf. Sci.* **164**, 111 (2000).

[51] Spieß, L., editor. *Moderne Röntgenbeugung: Röntgendiffraktometrie für Materialwissenschaftler, Physiker und Chemiker*. Teubner, Wiesbaden, (2005).

[52] Waseda, Y., Matsubara, E., and Shinoda, K. *X-ray diffraction crystallography*. Springer, Heidelberg [u.a.] (2011).

[53] Hammond, C. *The basics of crystallography and diffraction*, volume 21 of *IUCr texts on crystallography; 21*. Oxford University Press, Oxford (2016).

[54] Williamson, G. and Hall, W. *Acta Metallurgica* **1**, 22 (1953).

[55] Kerr, J. *Philosophical Magazine Series 5* **3**, 321 (1877).

[56] Argyres, P. N. *Phys. Rev.* **97**, 334 (1955).

[57] Qiu, Z. Q. and Bader, S. D. *Rev. Sci. Instrum.* **71**, 1243 (2000).

[58] Brukner, C. and Zeilinger, A. *Acta Phys. Slovaca* **49**, 647 (1999).

[59] Dunz, M., Schmalhorst, J., and Meinert, M. *AIP Adv.* **8**, 056304 (2018).

[60] Dunz, M. and Meinert, M. *J. Appl. Phys.* **128**, 153902 (2020).

[61] Meiklejohn, W. H. and Bean, C. P. *Phys. Rev.* **105**, 904 (1957).

[62] Nogués, J., Lederman, D., Moran, T. J., and Schuller, I. K. *Phys. Rev. Lett.* **76**, 4624 (1996).

[63] Leighton, C., Nogués, J., Suhl, H., and Schuller, I. K. *Phys. Rev. B* **60**, 12837 (1999).

[64] Mauri, D., Siegmann, H. C., Bagus, P. S., and Kay, E. *J. Appl. Phys.* **62**, 3047 (1987).

[65] Berkowitz, A. and Takano, K. *J. Magn. Magn. Mater.* **200**, 552 (1999).

[66] Kim, J.-V. and Stamps, R. L. *Appl. Phys. Lett.* **79**, 2785 (2001).

[67] Stamps, R. *J. Magn. Magn. Mater.* **242-245**, 139 (2002). Proceedings of the Joint European Magnetic Symposia (JEMS'01).

[68] Hu, J.-g., Jin, G., Hu, A., and Ma, Y.-q. *Eur. Phys. J. B* **40**, 265 (2004).

[69] O'Grady, K., Fernandez-Outon, L., and Vallejo Fernandez, G. *J. Magn. Magn. Mater.* **322**, 883 (2010).

[70] Stiles, M. D. and McMichael, R. D. *Phys. Rev. B* **59**, 3722 (1999).

[71] Fulcomer, E. and Charap, S. H. *J. Appl. Phys.* **43**, 4190 (1972).

[72] Ali, M., Marrows, C. H., Al-Jawad, M., Hickey, B. J., Misra, A., Nowak, U., and Usadel, K. D. *Phys. Rev. B* **68**, 214420 (2003).

[73] Sinclair, J., Hirohata, A., Vallejo-Fernandez, G., Meinert, M., and O'Grady, K. *J. Magn. Magn. Mater.* **476**, 278 (2019).

[74] Aley, N., Vallejo-Fernandez, G., Kroeger, R., Lafferty, B., Agnew, J., Lu, Y., and O'Grady, K. *IEEE Transactions on Magnetics* **44**, 2820 (2008).

[75] Reck, R. A. and Fry, D. L. *Phys. Rev.* **184**, 492 (1969).

[76] Nozières, J. P., Jaren, S., Zhang, Y. B., Zeltser, A., Pentek, K., and Speriosu, V. S. *J. Appl. Phys.* **87**, 3920 (2000).

[77] Briggs, D. and Seath, M. *Practical surface analysis.* Wiley, New York (1990).

[78] Malinowski, E. *Factor Analysis in Chemistry.* Wiley, New York (1991).

[79] Gall, D., Haasch, R. T., Finnegan, N., Lee, T.-Y., Shin, C.-S., Sammann, E., Greene, J. E., and Petrov, I. *Surf. Sci. Spectra* **7**, 167 (2000).

[80] Quarterman, P., Hallsteinsen, I., Dunz, M., Meinert, M., Arenholz, E., Borchers, J. A., and Grutter, A. J. *Phys. Rev. Materials* **3**, 064413 (2019).

[81] Gilbert, D. A., Grutter, A. J., Arenholz, E., Liu, K., Kirby, B. J., Borchers, J. A., and Maranville, B. B. *Nat. Commun.* **7**, 12264 (2016).

[82] Chang, H. W., Chien, Y. H., Yuan, F. T., Lai, Y. R., Wang, C. R., Horng, L., and Chang, W. C. *AIP Adv.* **10**, 025035 (2020).

[83] Meng, M., Wu, S. X., Ren, L. Z., Zhou, W. Q., Wang, Y. J., Wang, G. L., and Li, S. W. *J. Appl. Phys.* **116**, 173911 (2014).

[84] Yang, R., Haider, M., Yang, H., Al-Brithen, H., and Smith, A. *Appl. Phys. A* **81**, 695 (2005).

[85] Dunz, M., Matalla-Wagner, T., and Meinert, M. *Phys. Rev. Res.* **2**, 013347 (2020).

[86] Hoffmann, A. *IEEE Trans. Magn.* **49**, 5172 (2013).

[87] Sinova, J., Valenzuela, S. O., Wunderlich, J., Back, C. H., and Jungwirth, T. *Rev. Mod. Phys.* **87**, 1213 (2015).

[88] Vignale, G. *J. Supercond. Nov. Magn.* **23**, 3 (2009).

[89] Jungwirth, T., Niu, Q., and MacDonald, A. H. *Phys. Rev. Lett.* **88**, 207208 (2002).

[90] Dyakonov, M. and Perel, V. *Phys. Lett. A* **35**, 459 (1971).

[91] Kato, Y. K., Myers, R. C., Gossard, A. C., and Awschalom, D. D. *Science* **306**, 1910 (2004).

[92] Valenzuela, S. O. and Tinkham, M. *Nature* **442**, 176 (2006).

[93] Atulasimha, J. and Bandyopadhyay, S., editors. *Nanomagnetic and spintronic devices for energy-efficient memory and computing.* Wiley, Chichester (2016).

[94] Liu, L., Pai, C.-F., Li, Y., Tseng, H. W., Ralph, D. C., and Buhrman, R. A. *Science* **336**, 555 (2012).

[95] Gambardella, P. and Miron, I. M. *Phil. Trans. R. Soc. A* **369**, 3175 (2011).

[96] Wei, Z., Sharma, A., Nunez, A. S., Haney, P. M., Duine, R. A., Bass, J., MacDonald, A. H., and Tsoi, M. *Phys. Rev. Lett.* **98**, 116603 (2007).

[97] Matalla-Wagner, T., Rath, M.-F., Graulich, D., Schmalhorst, J.-M., Reiss, G., and Meinert, M. *Phys. Rev. Appl.* **12**, 064003 (2019).

[98] McGuire, T. and Potter, R. *IEEE Trans. Magn.* **11**, 1018 (1975).

[99] Grzybowski, M. J., Wadley, P., Edmonds, K. W., Beardsley, R., Hills, V., Campion, R. P., Gallagher, B. L., Chauhan, J. S., Novak, V., Jungwirth, T., Maccherozzi, F., and Dhesi, S. S. *Phys. Rev. Lett.* **118**, 057701 (2017).

[100] Železný, J., Gao, H., Výborný, K., Zemen, J., Mašek, J., Manchon, A., Wunderlich, J., Sinova, J., and Jungwirth, T. *Phys. Rev. Lett.* **113**, 157201 (2014).

[101] Bodnar, S. Y., Šmejkal, L., Turek, I., Jungwirth, T., Gomonay, O., Sinova, J., Sapozhnik, A., Elmers, H.-J., Kläui, M., and Jourdan, M. *Nat. Commun.* **9**, 348 (2018).

[102] Zhou, X. F., Zhang, J., Li, F., Chen, X. Z., Shi, G. Y., Tan, Y. Z., Gu, Y. D., Saleem, M. S., Wu, H. Q., Pan, F., and Song, C. *Phys. Rev. Appl.* **9**, 054028 (2018).

[103] V. M. T. S. Barthem, C. V Colin, H. M. M.-H. J. and Givord, D. *Nat. Commun.* **4**, 2892 (2013).

[104] Watanabe, H. and Yanase, Y. *Phys. Rev. B* **98**, 245129 (2018).

[105] Chen, X. Z., Zarzuela, R., Zhang, J., Song, C., Zhou, X. F., Shi, G. Y., Li, F., Zhou, H. A., Jiang, W. J., Pan, F., and Tserkovnyak, Y. *Phys. Rev. Lett.* **120**, 207204 (2018).

[106] Gray, I., Moriyama, T., Sivadas, N., Stiehl, G. M., Heron, J. T., Need, R., Kirby, B. J., Low, D. H., Nowack, K. C., Schlom, D. G., Ralph, D. C., Ono, T., and Fuchs, G. D. *Phys. Rev. X* **9**, 041016 (2019).

[107] Gomonay, H. V. and Loktev, V. M. *Phys. Rev. B* **81**, 144427 (2010).

[108] Zhang, P., Finley, J., Safi, T., and Liu, L. *Phys. Rev. Lett.* **123**, 247206 (2019).

[109] Shi, J., Lopez-Dominguez, V., Garesci, F., Wang, C., Almasi, H., Grayson, M., Finocchio, G., and Khalili Amiri, P. *Nat. Electron.* **3**, 92 (2020).

[110] Zhou, X., Chen, X., Zhang, J., Li, F., Shi, G., Sun, Y., Saleem, M., You, Y., Pan, F., and Song, C. *Phys. Rev. Appl.* **11**, 054030 (2019).

[111] Schroder, D. K. *Semiconductor material and device characterization.* Piscataway, NJ: IEEE Press, Hoboken, N.J., Wiley (2006).

[112] Perloff, D. S. *Solid State Electron.* **20**, 681 (1977).

[113] Matalla-Wagner, T. *Investigation of Néel-order spin-orbit torque switching in dc-sputtered CuMnAs thin films and identification of a parasitic contribution in the electrical readout.* PhD thesis, Bielefeld University (in preparation).

[114] Matalla-Wagner, T., Schmalhorst, J.-M., Reiss, G., Tamura, N., and Meinert, M. (2019).

[115] Johnston, D. C. *Phys. Rev. B* **74**, 184430 (2006).

[116] Rózsa, L., Selzer, S., Birk, T., Atxitia, U., and Nowak, U. *Phys. Rev. B* **100**, 064422 (2019).

[117] Obstbaum, M., Decker, M., Greitner, A. K., Haertinger, M., Meier, T. N. G., Kronseder, M., Chadova, K., Wimmer, S., Ködderitzsch, D., Ebert, H., and Back, C. H. *Phys. Rev. Lett.* **117**, 167204 (2016).

[118] You, C.-Y., Sung, I. M., and Joe, B.-K. *Appl. Phys. Lett.* **89**, 222513 (2006).

[119] Fina, I., Marti, X., Yi, D., Liu, J., Chu, J., Rayan-Serrao, C., Suresha, S., Shick, A., Železnỳ, J., Jungwirth, T., et al. *Nat. Commun.* **5**, 1 (2014).

[120] Akouala, C. R., Kumar, R., Punugupati, S., Reynolds, C. L., Reynolds, J. G., Mily, E. J., Maria, J.-P., Narayan, J., and Hunte, F. *Appl. Phys. A* **125**, 293 (2019).

[121] Nakayama, H., Althammer, M., Chen, Y.-T., Uchida, K., Kajiwara, Y., Kikuchi, D., Ohtani, T., Geprägs, S., Opel, M., Takahashi, S., Gross, R., Bauer, G. E. W., Goennenwein, S. T. B., and Saitoh, E. *Phys. Rev. Lett.* **110**, 206601 (2013).

[122] Chen, Y.-T., Takahashi, S., Nakayama, H., Althammer, M., Goennenwein, S. T., Saitoh, E., and Bauer, G. E. *Phys. Rev. B* **87**, 144411 (2013).

[123] Hoogeboom, G. R., Aqeel, A., Kuschel, T., Palstra, T. T. M., and van Wees, B. J. *Appl. Phys. Lett.* **111**, 052409 (2017).

[124] Althammer, M., Meyer, S., Nakayama, H., Schreier, M., Altmannshofer, S., Weiler, M., Huebl, H., Geprägs, S., Opel, M., Gross, R., Meier, D., Klewe, C., Kuschel, T., Schmalhorst, J.-M., Reiss, G., Shen, L., Gupta, A., Chen, Y.-T., Bauer, G. E. W., Saitoh, E., and Goennenwein, S. T. B. *Phys. Rev. B* **87**, 224401 (2013).

[125] Ebert, H., Ködderitzsch, D., and Minár, J. *Reports on Progress in Physics* **74**, 096501 (2011).

[126] The Munich SPR-KKR package, version 7.7, H. Ebert *et al.*, http://olymp.cup.uni-muenchen.de/ak/ebert/SPRKKR (2017).

[127] Ebert, H., Mankovsky, S., Chadova, K., Polesya, S., Minár, J., and Ködderitzsch, D. *Phys. Rev. B* **91**, 165132 (2015).

Danksagung

An dieser Stelle möchte ich allen danken, die mich durch meine Doktorandenzeit auf D2 begleitet und mich während der Erstellung dieser Arbeit unterstützt haben.

Mein größter Dank geht an Markus Meinert für die außergewöhnlich gute und intensive Betreuung, die vielen interessanten und hilfreichen Diskussionen sowie für deine Begeisterung an unserer gemeinsamen Forschung. Ich danke dir nicht nur für die Betreuung meiner Doktorarbeit, sondern auch dafür, dass du mich bereits während des Bachelor- und Masterstudiums mit spannenden Vorlesungs- und Forschungsthemen motiviert und mich für das wissenschaftliche Arbeiten begeistert hast. Darüber hinaus geht auch ein großer Dank an Günter Reiss: dafür, dass du mich zu Beginn meiner Promotion betreut und mir den Einblick in neue Forschungsgebiete ermöglicht hast. Außerdem danke ich dir natürlich für die Finanzierung meiner Doktorandenzeit, inklusive der Teilnahme an diversen Tagungen und Konferenzen.

Karsten, dir danke ich ganz herzlich für deine großzügige und geduldige Hilfe und Unterstützung bei allen technischen Fragen oder Problemen im Labor. Danke, dass du dir so viel Zeit genommen hast, mit mir die Depositionsanlagen für organsiche Schichten aufzubauen; ich hoffe, sie kommen in Zukunft noch oft zum Einsatz. Jan, bei dir bedanke ich mich für die Auger-Elektronen-Spektroskopie-Messungen und dafür, dass du sowohl bei technischen als auch bei bürokratischen Themen immer ein hilfsbereiter Ansprechpartner warst. Aggi, dir danke ich für deine freundliche Unterstüzung bei organisatorischen Fragen jeglicher Art.

Ein großer Dank geht natürlich an meine Kollegen von D2, ohne die Kaffeepausen, Konferenzen und auch die Laborarbeit nicht halb so unterhaltsam gewesen wären: Kathi, Philipp, Andreas, Luca, Dominik, Tristan, Denis, Jay, Tobi, Olli, Anastasiia und alle, die ich vergessen habe, vielen Dank euch!

Tristan, dir bin ich besonders dankbar dafür, dass du mich bei den Schalt-Experimenten unterstützt hast. Danke, dass du immer ein offenes Ohr für meine Fragen hattest und mir so den ein oder anderen Kabelsalat im Magnetlabor erspart hast. Andreas, dir möchte ich für deine geduldige Unterstützung am REM und am XRD danken und dafür, dass du immer ein so hilfsbereiter Ansprechpartner bei allen Fragen warst.

Kathi und Philipp, ihr habt mich schon durch die meiste Zeit des Studiums begleitet und wart auch während der Doktorandenzeit die besten Mitstreiter und Bürokollegen, die ich mir vorstellen kann. Danke, dass ihr mir bei allen Fragen zugehört und geholfen, mit mir diskutiert, und mich aufgemuntert oder abgelenkt habt. Vielen Dank auch für eure Unterstützung im Labor, ob am Bonder oder an der Sputteranlage, für die besten Mittagspausen, die schönsten Urlaube vor oder nach Koferenzen, und nicht zuletzt für das Korrekturlesen dieser Arbeit.

Abschließend danke ich außerdem meinem gesamten Prüfungskommittee und besonders Prof. Dr. Thomas Huser für die Erstellung des Zweitgutachtens für diese Arbeit.